NUMERICAL MODELING OF CASED-HOLE INSTABILITY IN HIGH PRESSURE AND HIGH TEMPERATURE WELLS

A Dissertation

by

ZHENG SHEN

Submitted to the Office of Graduate Studies of
Texas A&M University
in partial fulfillment of the requirements for the degree of

DOCTOR OF PHILOSOPHY

Approved by:

Chair of Committee,	Frederick E. Beck
Committee Members,	Stephen A. Holditch
	Eduardo Gildin
	Yuefeng Sun
Head of Department,	A. Daniel Hill

December 2012

Major Subject: Petroleum Engineering

ABSTRACT

Down-hole damages such as borehole collapse, circulation loss and rock tensile/compressive cracking in the open-hole system are well understood at drilling and well completion stages. However, less effort has been made to understand the instability of cemented sections in High Pressure High Temperature (HPHT) wells. The existing analysis shows that, in the perforation zones, casing/cement is subject to instability, particularly in the presence of cavities. This dissertation focuses on the instability mechanism of casing/cement in the non-perforated zones.

We investigate the transient thermal behavior in the casing-cement-formation system resulting from the movement of wellbore fluid using finite element method. The critical value of down-hole stresses is identified in both wellbore heating and cooling effects. Differently with the heating effect, the strong cooling effect in a cased hole can produce significant tension inside casing/cement.

The confining formation has an obvious influence on the stability of casing/cement. The proposed results reveal that the casing/cement system in the non-homogeneous formation behaves differently from that in homogeneous formation. With this in mind, a three-dimensional layered finite element model is developed to illustrate the casing/cement mechanical behavior in the non-homogeneous formation. The radial stress of cement sheath is found to be highly variable and affected by the contrast in Young's moduli in the different formation layers. The maximum stress is predicted to concentrate in the casing-cement system confined by the sandstone.

Casing wear in the cased-hole system causes significant casing strength reduction, possibly resulting in the casing-cement tangential collapse. In this study, an approach for calculating the stress concentration in the worn casing with considering temperature change is developed, based on boundary superposition. The numerical results indicate that the casing-cement system after casing wear will suffer from severe tangential instability due to the elevated compressive hoop stress.

Gas migration during the cementing process results from the fluid cement's inability to balance formation pore pressure. Past experience emphasized the application of chemical additives to reduce or control gas migration during the cementing process. This report presents the thermal and mechanical behaviors in a cased hole caused by created gas channels after gas migration. In conclusion, the size and the number of gas channels are two important factors in determining mechanical instability in a casing-cement system.

DEDICATION

To my father, Shen, Q. X.

To my mother, Lv, S. L.

ACKNOWLEDGEMENTS

I would like to express my gratitude to my committee chair, Dr. Frederick Beck, who has given so much encouragement in both academic and life areas. In addition, his invaluable suggestions laid fundamental basis for the success of this project.

I also would like to sincerely thank my committee members, Dr. Steve Holditch, Dr. Eduardo Gildin and Dr. Yuefeng Sun for their significant guidance and support throughout this research project. I also deeply appreciate their patience and tolerance in the process of this dissertation.

Thanks also go to my friends and colleagues and the department faculty and staff for making my graduate study at Texas A&M University a great and rewarding experience.

NOMENCLATURE

Alphabets

C	Fluid concentration
C_p	Rock specific heat
C_R	Rock compressibility
D	Diameter
E	Young's modulus
f	Body force
F_f	Fluid flux
G	Shear modulus
h_f	Fluid enthalpy
K	Thermal conductivity
p	Pressure
p_{fo}	Reference pore pressure
q_f	Source/Sink
r_w	Wellbore Inner radius
r_o	Wellbore outer radius
t	Thickness
T	Temperature
T_{fo}	Reference temperature
u_i	Displacement
U_f	Fluid specific internal energy
W	Weight function
Y_m	Yield strength

Greek symbols

α	Boit coefficient of rock ($\phi < \alpha < 1$)
α_T	Thermal expansion
β	Heat transfer coefficient
γ	Liquid leakage coefficient
μ	Viscosity
ε_{ij}	Strain tensor
$\varepsilon_{ij}^{\ e}$	Reversible strain
$\varepsilon_{ij}^{\ p}$	Irreversible strain
ε_{vol}	Volumetric strain
σ^*	Material strength
σ_{ij}	Normal stress tensor
τ_{ij}	Shear stress tensor
ρ_R	Rock density
ρ_f	Fluid density
ρ_{fo}	Reference fluid density
μ	Fluid viscosity
ν	Poisson ratio
λ	Elasticity modulus
ϕ	Porosity
δ_{ij}	Variables operator
Nu	Nusselt number
Re	Reynold's number
Pr	Prandtl number

Subscript

Γ	Integral area
Ω	Integral volume
ϕ_i, ϕ_j	Interpolation function
r	Rock
f	Fluid
i	Inner wellbore
o	Outer wellbore
x, y, z	Direction in Cartesian coordinate
r, θ, z	Direction in Cylindrical coordinate

TABLE OF CONTENTS

Page

LIST OF FIGURES

Page

LIST OF TABLES

Page

1. INTRODUCTION

1.1 Importance

The major function of casing and cement in oil and gas wells is to prevent wellbore collapse during the life of a well. Damages in the casing-cement system will decrease the capacities of the casing/cement mechanical resistance. Various well events such as drilling, cementing, perforating, well testing, chemical stimulation and hydrogen production can cause serious well instabilities, eventually result in the well abandonment.

In order to meet the exponentially growing demand for hydrocarbon energy, HPHT (high pressure and high temperature) drilling in deep formations has been opted for by oil companies. Casing/cement design is reportedly insufficient because some unique problems do exist when developing such wells. One of the major challenges is to dealing with the narrow drilling window. Drilling tools are also typically limited by the depth and rock hardness in HPHT wells. In addition, well control in a HPHT environment becomes much more difficult because kick detection techniques are far from perfect, despite many efforts made in recent years.

To prevent wellbore collapse, the casing-cement system is expected to survive from all destructively induced stresses created by the down-hole operations during the span of the well life [1]. To achieve the stable casing-cement system as stated above, casing strings have to be designed and cemented in place properly before the well can be drilled and cemented in the next stage. It is therefore expected that the knowledge of stress evolution inside the casing/cement is extremely important for well engineers.

Drilling and well completion in HPHT wells can cause both wellbore cooling and heating effects. In a wellbore circulation system, the movement of wellbore fluid dominates the temperature distribution in the casing-cement-formation system. Heat transfer occurs even with a slight temperature difference between the wellbore and the formation. The direction and value of thermal stress depend on temperature difference across the wellbore, casing, cement and formation. Either assigning a uniform

temperature or applying temperature difference as boundary conditions in a numerical model is insufficient for evaluating the effect of thermal stress inside the casing-cement system.

It is worthwhile to understand the relationship of heat transfer and the induced thermal stress with time in cemented zones. In this study, we simulated the stress evolution inside casing/cement in the cemented zones under HPHT conditions. We will discuss the possible reasons for casing-cement instability. The casing-cement-formation system is assumed not to fail even when the induced stress exceeds the material strength in the numerical models. In this study, the critical maximum stress inside the casing-cement system is identified in the wellbore fluid movement. Therefore, the thermal effect in HPHT wells should not always be overemphasized.

In addition, the formation tectonic effect does cause the instability in casing-cement system. We conclude that maximum radial and equivalent stresses are subject to be in the direction of the formation minimum horizontal stress. The maximum compressive radial stress inside the casing-cement system will decrease with the strong formation tectonic effect; meanwhile, the maximum equivalent stress will increase.

Casing wear is considered a serious well problem in HPHT wells. The rotation of drill pipe creates the significant contact force at the inner wall of casing. It causes the reduction of casing wall. Severe wear of casing is typically found in the extended and horizontal well because of the huge down-hole torque and contact force, particularly in drilling through deep formation with a long time rotation of drill pipe.

Comprehensive knowledge of the mechanical response of worn casing in the casing-cement system can be used to propose necessary precautions for the well instability caused by any future down-hole operations. However, our current understanding of the mechanical behavior of worn casing is not enough. A limited number of researchers worked to investigate the stress response in the worn casing (Song et al. 1992; Wu and Zhang 2005; Hall and Malloy 2005). Other studies concentrated more on the relationship of wear depth and contact force based on the experimental tests that the wear depth is recorded at a given contact force.

None of the studies consider the mechanical behavior of worn casing in the cemented section of a well. In our study, the predicted results show that the effect of the formation largely reduces the risk of tensile failure near the worn part of casing. Furthermore, without considering the temperature change inside the worn casing, the stress concentration in the worn area of casing is apparently underestimated.

The effect of formation is to provide mechanical support to casing in the wellbore. The homogeneous formation has been used in different wellbore instability models. In a well of thousands meters away from the surface, the casing could be cemented with different formations. The interaction of casing, cement, and nonhomogeneous formation should be investigated for evaluating the casing-cement instability. This dissertation recognized that the nonhomogeneous formation consisting of shale and sandstone did impact the stability of casing/cement.

In order to present the effect of the nonhomogeneous formation on the casing-cement system, we built a 3D FEM model to address the instability of the cased-hole model. The mechanical behavior of casing cemented with multiple layers of sandstone and shale are studied. Because of heat transfer in the model is in the radial direction, the analysis of mechanical response of the casing-cement system will be constraint on the radial stress. Heat flux is emphasized to understand the direction and value of heat transfer with time in the cased-hole model. The thermal stress inside the casing-cement system is calculated as a function of time. The predicted results indicate that the radial compression stress in the casing-cement-shale layer is much larger than it is in the casing-cement-sandstone layer when the identical burst pressure is applied in the wellbore.

Gas migration during the cementing displacement in a well is a problem for many years. It is still a technique challenge in terms of avoiding cement shrinkage and gas channels. The consequence of gas migration in a well can result in the loss of cement bond, and then damages the formation zonal isolation. In the liquid state of cement slurry, gas is free to travel up as long as the formation gas pressure is higher than the hydrostatic pressure of liquid cement. Weight cement slurry may use to balance the high

formation gas pressure in a deep well. Meantime, the weight of cement slurry has to be increased with the addition of certain heavy particles in the slurry. In a typical HPHT well, the margin between the formation fracturing gradient and the pore gradient is small. It is therefore anticipated that the dedicated design of cement slurry is required to prevent any unwanted fracture and gas channels.

Some measurements based on the control of cement shrinkage are developed in terms of reducing gas migration in the cementing displacement stage. In reality, the cased-hole instability caused by gas migration more or less exists in all kinds of wells. The casing-cement system strength in a gas migration well will be changed because of the gas channels after gas migration. For both economical and safe consideration, it is important to understand the mechanical response of casing/cement by the presence of gas channels.

We present the possible instability in the casing and cement system due to the influence of gas channels in the gas migration well. To be able to include the thermal effect, the gas channel model is developed to obtain the mechanical response of casing and cement in the HPHT conditions. In this study, the casing-cement instability resulting from the effects of the number and size of gas channels are clarified.

1.2 Literature review

Maintaining well stability in the drilling process is a crucial step for the success of well construction in oil and gas fields. Significant efforts to improve drilling stability have been made in recent years.

A significant number of drilling problems comes from drilling in shale formations. Shale is mainly composed of fine grain sands and clay. It is found in approximate 90% of drillable formations. The wellbore could be enlarged by the water hydration of swelling shale. Researcher investigated the open-hole instability caused by the existence of shale. The chemical and thermal interaction on the borehole stability has been analyzed. [2].

Some other authors revealed the well instability in the junction of multilateral well in varying stress orientation [3]. It is stated that the stress concentration most likely happens around the well junction areas.

The discussions of the down-hole integrity account for the effects of static wellbore fluid and homogeneous formation [1, 4-17]. However, these studies are not capable to comprehensively depict the thermal and mechanical behaviors of casing/cement in HPHT wells.

Casing burst resistance is an important factor at the initial stage of casing design. Burst criteria are used to guarantee well integrity. Besides the API standard in Eq. 1.3, Wu and Zhang (2005) propose several different models: the initial yield burst standard, the full yield burst standard, and the rupture burst standard. The initial stress criteria in Eq. 1.4 emphasizes the casing initially yields at the inner wall of casing. Eq. 1.5 describes the casing yields across the entire casing, which is named as the full yield criteria. Eq. 1.6 states the rupture criterion, which emphasizes casing ductile and tensile resistance. t is the thickness of casing wall. D is casing diameter. Y_m is the yielding strength of casing.

$$p_{API} = \frac{1.75 Y_m t}{D} \tag{1.3}$$

$$p_{IY} = \frac{1.75 Y_m}{\sqrt{3}} \frac{2t}{D} (1 - \frac{t}{D}) \tag{1.4}$$

$$p_{FY} = \frac{1.75 Y_m}{\sqrt{3}} \frac{2t}{D} (1 + \frac{t}{D}) \tag{1.5}$$

$$p_{DR} = \frac{1.75 Y_m t}{D - t} \tag{1.6}$$

Drilling fluid in the wellbore balances formation in-situ stress and prevents the invasion of reservoir fluid. Because of the effect of drilling slurry degrading in high temperature environment, limited types of viscous fluids can be used in HPHT wells.

Maintaining the well integrity becomes a difficult task when the bit penetrates into a deep formation.

Wellbore instability problem due to the temperature variation in HPHT wells is increasing during drilling and completion stages. The induced thermal stress caused by the significant temperature difference between the wellbore and the surrounding formation can result in the physical damage of casing/cement.

In HPHT wells, it requires better knowledge of down-hole induced stresses since both overburden effect and temperature significantly increase along with drilling in deep formation. The wells experience the stimulation pressure of 14,000 psi and the production drawdown of up to 13,000 psi. The 300 ˚F temperature variation in the oil wells is measured [1].

Wu and Kanauss [18] reportes that the production casing experiences the hot-yield state and fatigue in the cyclic steam injection wells. The effects of the surrounding cement and formation have not been included. Fleckstein .et .al ([12],[15]) have shown that the surrounding formation significantly increased the burst resistance of casing in a isothermal down-hole condition. By the lack of the thermal effect due to wellbore fluid movement, the proposed method doesn't account for the effect of transient heat transfer on the casing/cement. Gray [13] proposes the cased-hole deformation model using staged finite element method. The near wellbore plastic deformation is predicted in his research.

Sunal [19] stated that the casing collapse by the presence of the horizontal stresses may result from the plastic behavior of formation. A finite difference simulator-Frac3D was used. It is indicated that casing failure in salt is faster than it in shale because the salt cannot hold much compression stress before failure. The ignore of temperature variation in this analysis could comprise its field application. Nabipour [14] analyzed the cement mechanical behavior in deep gas well using a 2D finite element model, which is weakened by the lack of down-hole stress evolution because of the movement of wellbore fluid. Heather [1] has shown that, in Hilltop field of Texas, the serious debonding and micro annulus inside cement sheath existed in the wells over

14,000 ft. That report proposed that the procedures to alleviate the micro annulus could include reducing the prefrac pressure drawdown, pumping frac fluids through tubing and packer and displacing the cement slurry using brine instead of heavy drilling mud.

Casing wear is considered a serious well instability problem and it causes important contact force because of the contact of tool joint and inner casing wall during the rotation of drill pipe. It is not only a problem related to directional and extended wells, but it also occurs in vertical wells. The wear on casing leads to the reduction of casing wall, which could reduce down-hole burst and collapse resistance and form stress concentration around the worn area. Casing wear is difficult to predict and measure in drilling deep well with high ECD (Equivalent circulation density) and high circulating temperature. Particularly, the contact force becomes much hard to avoid during drilling in deep formation. In case of corrosive fluids in a well with casing wear, the loss of casing thickness will be accelerated due to the chemical reaction destructing the surface of casing.

The drill pipe rotation in the drilling process can uniformly reduce the casing string wall, or form a crescent shape wear on casing. Some researchers focused on the worn volume of casing based on numerous laboratory measurements [20]. Gao .et .al [21] investigated the relation of the worn depth of casing and the contact force using a group of scattering data. In this analysis, each worn depth on the casing was recorded at a given contact force.

Other researchers investigated the maximum wear groove depth based on the contact pressure generated on the inner wall of casing [22]. Various-sized drill strings were used to predict the groove depth of crescent-shaped casing and the casing wear was tested in single, sharp and the blunt groove. Another study emphasized the alleviation of casing wear using appropriate well operations such as the dogleg severity control and sealant application in the worn sections [23].

The correct understanding of the true stress profile of worn casing allows for economical well operations. A limited number of researchers have worked to investigate the mechanical responses of worn casing in cased hole [4, 22, 24]. Song al [24] focused

on the rupture capacity of casing after wear. The down-hole stress at the surfaces of worn casing was solved by dividing the worn casing into three superimposable shapes. The induced hoop stress of worn casing can be obtained using the superposition principle in a bipolar coordinate.

Others agreed that the casing wear model was built assuming a slotted ring inside the casing wall [4]. The resistance of worn casing tangential strength is decreased because of the reduction of casing wall. The down-hole hydraulic pressure acting on the surface of the slotted ring will increase the risk of worn casing failure. The stress under the worn surface is also investigated by Rainforth [25]. His experimental results indicated that the area below the worn surface would experience the unusual strain due to the stress concentration. Because the formation and thermal effects on the worn casing have not been included in these studies, the reported results are not sufficient for a better practical application.

A successful cementing job provides the good zonal isolation to prevent any unwanted communication between the wellbore fluid and the formation fluid. The basic element of cement slurry is from the product of burning the blend of limestone and clay. To cope with severe down-hole conditions, additives are mixed with the cement in the process of cementing job. In addition, the cement composition and placement procedures must be chosen correctly in order to achieve an adequate cementing job. The density of cement should be sufficient to prevent gas migration in the cement column and avoid fracturing formation simultaneously.

However, high strength of cement is not always applied to the solutions for deep well development. Researchers have shown that the flexible cement may be used to enhance the entire wellbore burst resistance [26]. Thus, mechanical properties of the cement should be selected based on the knowledge of wellbore geometry and formation in-situ stresses as well as any anticipated load.

Gas migration during the cementing process has been a serious problem in industry for many years, particularly occurs in the development of deep wells. Gas migration through cement columns causes gas channels after the migration. It

dramatically reduces the strength of cement sheath. On the other hand, the gas migration increases the risk of casing collapse [11]. Gas migration also could cause the sustained casing pressure when gas bubbles flow up the cement slurry. The sustained casing pressure has proved to result in high risk gas leakage in the tubing.

Gas channel occurs in the cementing process resulting from the cement column's inability to balance pore pressure. Others reasons behind gas migration include the inadequate drilling fluid displacement and the debonding of cement sheath [27]. Fig. 1.1 has revealed that the permanent channels generated in the cement column using the experimental test. It will decrease the strength of cement sheath and cause the loss of formation zonal isolation [28].

Fig. 1.1 The existence of gas channels during the lab test

Gas migration often occurs when drilling through hydrocarbon saturated rocks, especially in gas wells. Different researchers have studied to control the occurrence of the gas migration in the help of new cement formula. [9-11]. In order to prevent gas entering into cement columns, the methods of reducing gas migration include that special additives are added to the cement slurry [29].

For a casing/cement without worn casing and gas channels, the radial and hoop stresses can be evaluated using Eqs. 1.1 and 1.2. Casing is expected to suffer from significant tension when the burst pressure is applied on a casing without cemented with the surrounding formation.

$$\sigma_r = \frac{p_i r_i^2}{r_o^2 - r_i^2}\left(1 - \frac{r_o^2}{r^2}\right) - \frac{p_o r_o^2}{r_o^2 - r_i^2}\left(1 - \frac{r_i^2}{r^2}\right) \tag{1.1}$$

$$\sigma_\theta = \frac{p_i r_i^2}{r_o^2 - r_i^2}\left(1 + \frac{r_o^2}{r^2}\right) - \frac{p_o r_o^2}{r_o^2 - r_i^2}\left(1 + \frac{r_i^2}{r^2}\right) \tag{1.2}$$

1.3 Dissertation organization

The first section introduces the well instability in cemented zones and states the background for the problems. The major limitations for modeling the processes of drilling and well completion in HPHT wells have been reviewed. The second section provides the general theory for the analysis of wellbore stability in both cased hole and open hole. An overview on heat transfer in both cases is made. In terms of the mechanical behavior in open hole, the temperature and formation pore pressure can be solved for before the stress model. The second purpose of this section presents the consequence of the hydraulic and thermal loads on casing/cement due to wellbore fluid movement.

The third section describes the processes of numerical integration to the proposed finite element models. Both 2D and 3D integration techniques are discussed in detail. It provides the computational procedures required for solving the numerical models. The relative coefficient matrices for heat transfer and stress models are also analyzed in this chapter.

The discussions on the proposed results are included from the forth section to the seventh section. Section 4 is to dealing with stress evolution inside the casing/cement/formation in several down-hole scenarios, which can be summarized into heating process and cooling process. The critical mechanical behavior of casing/cement due to the circulation of wellbore fluid is analyzed based on the variation of induced stresses. This part also addresses the formation tectonic effect on casing-cement instability.

Section 5 emphasizes the importance of the nonhomogeneous formation on the instability of casing/cement. The formation consists of sandstone and shale layers. The casing/cement mechanical responses caused by the nonhomogeneous formation effect as well as the effect of transient heat transfer are presented.

Section 6 is to dealing with the instability of worn casing in the cemented well. An analytical solution to the stress model of casing wear is developed in this chapter. This section investigates the post mechanical behavior of the remaining part of worn casing/cement.

Section 7 investigates the cemented well instability caused by gas channels due to gas migration. Our research evaluates the stress redistribution inside casing/cement by the presence of gas channels. The sensitivity analysis including the effects of the size of gas channels and the number of gas channels is performed accordingly. The last section includes the conclusions and the recommendations for future work.

2. WELLBORE THERMAL AND MECHANICAL BEHAVIORS

This section describes the methodologies of heat transfer and the induced mechanical responses in permeable and impermeable zones, which in this report are corresponding to open hole and cased hole respectively. Although we emphasize the casing-cement instability, the approach developed in this section can extend into open-hole instability analysis. Temperature is solved in advance, and then the thermal effect due to temperature non-uniform distribution in the well is transferred to the stress model after every time step. Finite element analysis for investigating the stress evolution in the casing-cement-formation system will be emphasized in this report.

2.1 Governing equations in open hole

Borehole instability due to the temperature variation between wellbore and formation has become an important topic along with drilling in deep formations. Down-hole heat transfer resulting from the mud circulation may assist wellbore stability. Li [30] concluded that the cooling effect helped alleviate the borehole shear failure to some extent. In open hole, heat transfer from the wellbore into the formation depends on the effects of heat conduction and convective.

The down-hole stress balance in a well is broken when the cylindrical rock is removed and replaced by the drilling fluid. The drilling fluid provides the hydraulic support to avoid the borehole collapse, also functions to cool down-hole drill equipments and clean drilling cuts. In reality, the magnitude of down-hole hydraulic pressure is hard to control in order to balance the formation stress. When the drilling mud pressure is not sufficient, formation during drilling may collapse if the induced stress is beyond the formation strength. On the other side, if the drilling mud pressure is greater than the formation effective stress, subsequent lost circulation can occur by the consequence of fracturing formation.

Fluid transportation in a porous medium causes the variations of pore pressure, temperature and rock deformation near the wellbore. Conductive and convective heat transfer in the porous formation occurs when the wellbore fluid temperature is different from the formation temperature. The thermal effect in a porous medium is known to cause the expansion of pore fluid and formation matrix. In permeable zones, the coefficient of heat convective is a dominating factor in deciding the temperature profile near the wellbore.

Fluid movement in a porous medium refers to the interaction of fluid flowing and rock mechanical response. Terzaghi (1923) presented a soil model of rock deformation while considering the influence of pore fluid. The net effective stress in his model was defined as the total stress minus the effective fluid pressure in the porous space. The relation can be found in Eq. 2.1. The effective stress variation causes the stress redistribution in the well.

$$\sigma'_{ij} = \sigma_{ij} - \delta_{ij}\alpha p \tag{2.1}$$

Eq. 2.2 presents the energy conservation law, which can be used in an open hole. The temperature distribution near the well is determinate by a group of parameters that consisting of rock porosity, thermal conductivities and fluid enthalpy etc. Although the temperature is an explicit variable; it cannot be obtained without q_f , the fluid flowing rate.

$$\begin{aligned} &\frac{d}{dt}\int_{Vn} ((1-\phi)\rho_R C_R T + \phi\rho_f U_f)dV = \\ &\int_{\Gamma n}(-[(1-\phi)K_R + \phi K_f]\nabla T + h_f F_f).n d\tilde{A} + \int_{Vn} q_f h_f dV \end{aligned} \tag{2.2}$$

Because wellbore fluid in porous rock can communicate with the rock system, the fluid flow rate and pore pressure change simultaneously. The mass conservation, as shown in Eq. 2.3, is used to compute the pore pressure and flow rate. The relationship of fluid flow rate and pore pressure is illustrated by Darcy's equation.

$$\frac{d}{dt}\int_{Vn}(\phi\rho_f)dV=\int_{\Gamma n}\left(-\frac{k\rho_f}{\mu_f}\right)\left(\nabla P_f-\rho_f g\right)nd\tilde{A}+\int_{Vn}q_f dV \tag{2.3}$$

The induced pore pressure and temperature changes due to the interaction of fluid and rock can change the effective stress of formation. Practically, rock porosity and permeability also change with the variation of pressure and temperature. In a nonlinear condition, the porosity is function of pressure, temperature and volumetric strain, as shown in Eq. 2.4. The permeability is nonlinearly changed along with the change of pressure and temperature in most cases. Instead of the direct calculation for the permeability, the permeability can be obtained from different correlations based on the rock porosity.

$$\phi^{n+1}=\phi^n+a(\varepsilon^{n+1}-\varepsilon^n)+C_R(P^{n+1}-P^n)+\alpha_T(T^{n+1}-T^n) \tag{2.4}$$

Compared with the compressibility of rock, fluid has much large compressibility. It is thereby expected that the fluid density would be considered as a significant variation during the well production and injection stages. Fluid density is not only a function of pressure and temperature, but also it is influenced by the fluid leakage effect. The calculation for the fluid density is given in Eq. 2.5.

$$\rho_f=\rho_{fo}\exp[C_R(p_f-p_{fo})+\alpha_T(T_f-T_{fo})+\gamma C] \tag{2.5}$$

In Equ 2.3, the fluid viscosity has the inverse relation to the rock permeability. Fluid temperature influences the viscosity. Zyvoloski (1980) presented the equation for the calculation of fluid viscosity in the Newtonian fluid (pa.s), as stated in Eq. 2.6. As a matter of fact, most drilling muds exhibit the non-Newtonian fluid behavior. Santoyo

[31] presented that, in Eq. 2.7, the viscosity equation is used for non-Newtonian fluids(pa.s).

$$\mu = 2.414 \times 10^{-8} \times 10^{\frac{247.8}{T+133.5}} \tag{2.6}$$

$$\mu = (15.7688 - 0.0420576T - 8.03819 \times 10^{-5} T^2) \times 10^{-3} \tag{2.7}$$

The following numerical model describes the temperature and pressure profiles in an open-hole scenario when the fluid is injecting in the formation. The initial temperature of wellbore is 212 ˚F. The wellbore fluid of 330 ˚F is injected into the formation. Other important parameters such as the rock porosity of 0.15 and the permeability of 300 md, are proposed in this model. The heat capacity of rock is 0.25 Btu/lb. ˚F. Rock density is an important factor in a transient heat transfer during the fluid flowing in the porous rock. The heat energy of rock is determined by the product of the rock heat capacity and density. The rock density of 0.094 lb/in^3 and the rock heat capacity of 0.17 Btu/lb.˚F are assumed. The heat convective and conductive effects are considered simultaneously in this case.

Fig. 2.1 has shown that the temperature near the wellbore significantly increased due to the hot fluid injection. The pore pressure of formation also increases along the fluid is injected into the porous formation. Fig. 2.2 has revealed that the formation pore pressure has increased by 400 psi from the initial pressure of 4350 psi by the end of one year.

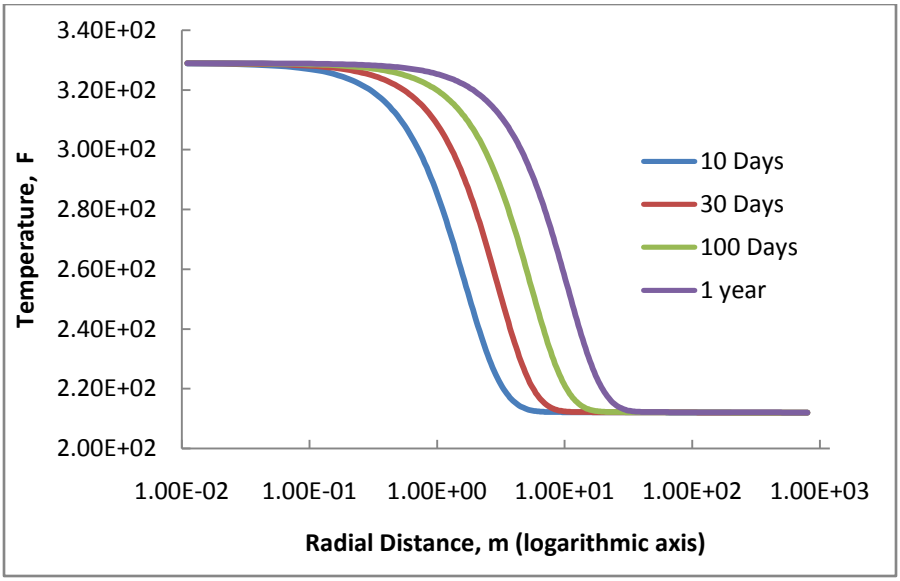

Fig. 2.1 Temperature profile of injection well in 1 year

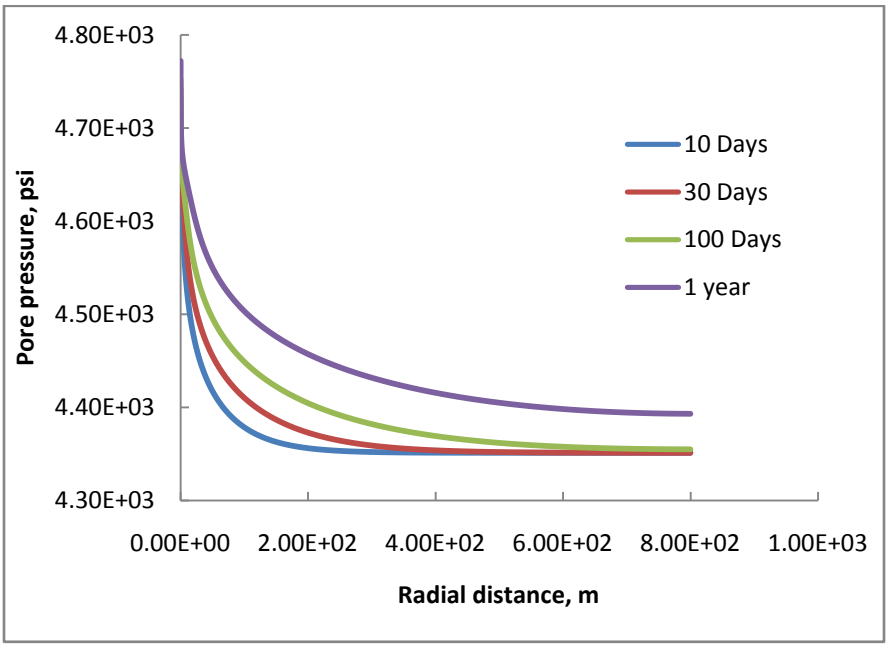

Fig. 2.2 Pore pressure profile of injection well in 1 year

In the proposed method, the temperature and pore pressure profile are solved first. After obtaining the rock volumetric strain from the stress model, the calculated

temperature and pressure are used to update the fluid and rock properties at each time step.

The governing equations for the non-isothermal fluid flow through a porous deformed medium have been presented by different researchers ([32],[33],[34]). The equations are used to describe the poro-thermo-elasticity problem. They can be summarized in the following forms, as shown in Eqs. 2.8 to 2.10.

$$(\lambda+G)\frac{\partial \varepsilon_{vol}}{\partial x}+G\frac{\partial^2 u}{\partial x^2}-\frac{\alpha E}{1-2\nu}\frac{\partial T}{\partial x}-\alpha\frac{\partial p}{\partial x}+f_x=0 \tag{2.8}$$

$$(\lambda+G)\frac{\partial \varepsilon_{vol}}{\partial y}+G\frac{\partial^2 u}{\partial y^2}-\frac{\alpha E}{1-2\nu}\frac{\partial T}{\partial y}-\alpha\frac{\partial p}{\partial x}+f_y=0 \tag{2.9}$$

$$(\lambda+G)\frac{\partial \varepsilon_{vol}}{\partial z}+G\frac{\partial^2 u}{\partial z^2}-\frac{\alpha E}{1-2\nu}\frac{\partial T}{\partial z}-\alpha\frac{\partial p}{\partial x}+f_z=0 \tag{2.10}$$

Thus, the computational procedures for a open-hole stress model in this discussion can be categorized into two steps. Equs. 2.2 to 2.3 are used to calculate the temperature and pore pressure. The stress distribution near the wellbore is obtained through Eqs. 2.8 to 2.10.

2.2 Governing equations in cased hole

Full integrity of casing and cement in HPHT wells plays an important role for the down-hole zonal isolation. Casing-cement damages in the wellbore can be caused by the reservoir compaction, especially when the casing is located in the perforation zones. Because of the harsh environment in HPHT wells, casing and cement failures in non-perforating zones are increasingly recorded resulting from some unclear down-hole mechanical responses. The subsequent remediation for the failures is extremely expensive in the cost of loss of production and well workover service.

2.2.1 Thermal behavior

In a deep well, the heat transfer through the casing-cement system in the cased sections due to the wellbore fluid movement should be addressed properly. Because of a minor contribution caused by the friction work of viscous fluid to the total heat energy in our case, the following discussion won't include this factor.

A typical flow scheme of wellbore fluid movements consists of the fluid downward flow through the central pipe and upward flow through the annulus. The energy balance is broken at the beginning of fluid circulation. The unbalanced behavior will result in stress variation in the vicinity of wellbore. In a cased hole with fluid flow, the temperature distribution in the wellbore depends on the conductive heat inside the casing-cement-formation system and convective heat at the boundaries. As the fluid enters the annulus between drill pipe and formation, the near wellbore temperature is determined by the rate of heat exchange between the formation and the wellbore fluid in the annulus. The boundary and initial conditions in the cased hole include the temperature and fluid hydraulic pressure as well as the formation stresses.

Heat transfer in the cased hole dynamically occurs in the process of wellbore fluid circulation. Figs. 2.3 and 2.4 describe two typical cases, the cooling effect and heating effect in the cemented sections. As shown in Fig 2.3, the cool fluid is pumped through the central pipe into the bottom hole while the surrounding formation has a relative higher temperature. This process cools down the casing-cement-formation system. On the contrary, the produced oil from deep reservoir is usually hotter than the upper cemented section during it returning to the surface. Fig 2.4 indicates that the hot fluid in the wellbore heats the surrounding wellbore. Despite high temperature effect on the integrity of casing-cement system has been emphasized by different researchers, the quantity of thermal stress should be further understood.

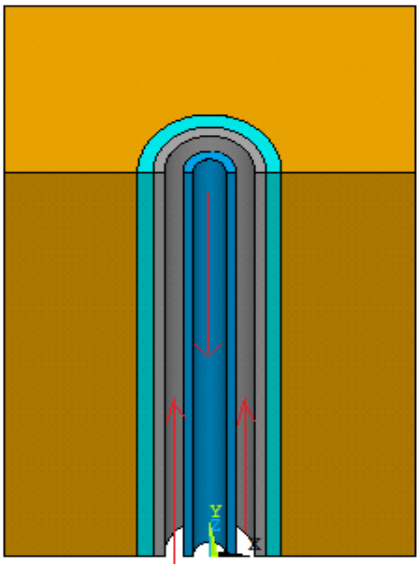

Fig. 2.3 The circulation of wellbore fluid in HPHT wells

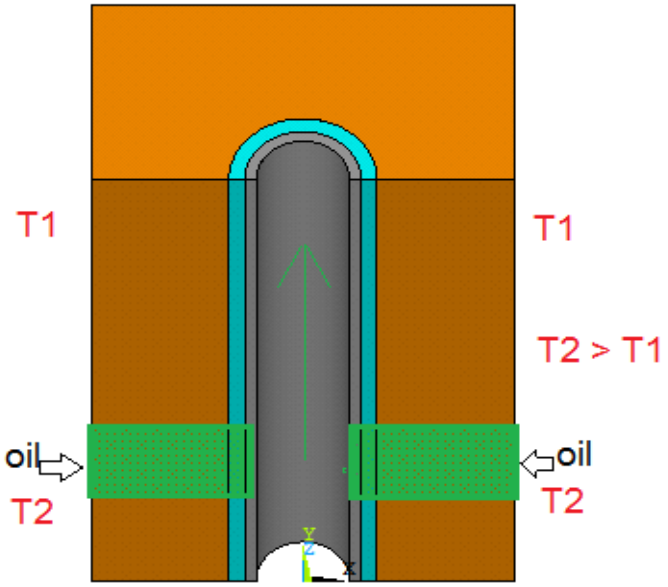

Fig. 2.4 Producing oil flowing up in HPHT wells

Eq. 2.11 reveals the energy conservation law, which can be used in open hole and cased hole conditions. The physical meaning is that energy change per unit of time, which is represented by the left side, is equal to heat energy accumulation in the medium

during heat flow in and out, which is represented by the right side. Q at the second term of the right side represents heat source and sink in the wellbore.

$$\frac{d}{dt}\int_{Vn} M_T dV = \int_{\Gamma n} F_T . n d\widetilde{A} + \int_{Vn} q dV \tag{2.11}$$

Where:

$$F_T = -k_x \frac{dT}{dx} - k_y \frac{dT}{dy} - k_z \frac{dT}{dz} \tag{2.12}$$

$$M_T = \rho_R C_R T \tag{2.13}$$

To explicit express the primary variables of Eq. 2.11, Substitute Eqs. 2.12 and 2.13 into Eq. 2.11, yield the Eq. 2.14, which can used to calculate temperature distribution with time in the cased hole. The temperature profile is mainly dependent on the mediums' thermal conductivity and density, specific heat.

$$\rho_R c_R \dot{T} - k_x \frac{d^2T}{dx^2} - k_y \frac{d^2T}{dy^2} - k_z \frac{d^2T}{dz^2} - Q = 0 \tag{2.14}$$

Due to the absence of fluid transport in the cemented sections, there is no energy exchange that is induced by the fluid convective heat. This leads to the thermal boundaries as stated in Eqs. 2.15 and 2.16. The boundary conditions can be characterized using temperature and heat flow rate.

$$T = \hat{T} @ \Gamma_T \tag{2.15}$$

$$\hat{q}_n = q_{cond} @ \Gamma_q \tag{2.16}$$

Finite element method (FEM) has become widely accepted as a valuable technique for solving complex mechanical problems. Different mathematical equations are used to characterize the mechanical problems. The FEM is capable to provide exactly approximate solutions to the equations. Using this method, an integrity domain is divided into a number of small subdomains so that the solution within each subdomain can be represented by a function simpler than that required for entire

domain. The local coordinate system is used in all subdomains. Then the subdomains are assembled together in a global coordinate.

The casing, cement and formation in the cased hole are assumed fully bonded. Temperature is the primary unknown variable in the heat transfer model and it is solved numerically. The numerical approach in the finite element model has two computational parts: the spatial and temporal discretizations. The representation of the given cased-hole model using appropriate elements is an important step in finite element analysis. The continuous casing-cement-formation system is converted into a group of discretized elements.

We seek the approximate solutions to the heat transfer and stress models. It is necessary to reduce the approximation errors by using a suitable finite element mesh. There exist some general rules to discretize a given domain. First, the element type must be able to represent the original problem. Then, the number of elements and element size should accurately characterize the finite element domain. Thus, the sensitivity analysis using different elements is preferred before conducting the final numerical simulation. Generally, dense elements are preferred in the potential temperature and stress concentration regions. The following analysis is to obtain the weak formulation for the finite element model.

Multiply the weighted function w(x,y,z) of the finite element model in both sides of Eq 2.14. It yields Eq. 2. 17.

$$\begin{aligned}&\int_{\Omega e}(w\rho_R c_R\frac{dT}{dt}-k_x\frac{dw}{dx}\frac{dT}{dx}-k_y\frac{dw}{dy}\frac{dT}{dy}-k_z\frac{dw}{dz}\frac{dT}{dz}-wq)d\Omega\\&-\oint_{\Gamma e}w(k_x\frac{dT}{dx}n_x+k_y\frac{dT}{dy}n_y+k_z\frac{dT}{dz}n_z)=0\end{aligned}\tag{2.17}$$

The next step of developing the weak formulation is to impose the actual boundary conditions. The wellbore fluid temperature of T_w is circulated from the surface to the bottom hole, which will result in the heat convective boundary condition. The boundary conditions in Eq 2.17 are incorporated, and then Eq. 2.18 will be obtained.

$$\int_{\Omega e}(\rho_R c_R \frac{dT}{dt} - k_x \frac{dw}{dx}\frac{dT}{dx} - k_y \frac{dw}{dy}\frac{dT}{dy} - k_z \frac{dw}{dz}\frac{dT}{dz} - wq)d\Omega + \oint_{\Gamma e} w(\hat{q}_n - \beta T + \beta T_w)ds = 0 \tag{2.18}$$

The Eq. 2.19 is given to approximate the temperature variable, T over a master element.

$$T = \sum_{j=1}^{n} T_j{}^e \phi_j{}^e(x, y, z) \tag{2.19}$$

In order to obtain the semidiscrete model of the heat transfer problem, the temporal part is approximated using Eqs. 2.20 and 2.21.

$$T(x, y, z, t) = \sum_{j=1}^{n} T_j{}^e(t_s)\phi_j{}^e(x, y, z) \tag{2.20}$$

$$\alpha \dot{T}_{s+1} + (1-\alpha)\dot{T}_s = \frac{T_{s+1} - T_s}{\Delta t_{s+1}} \tag{2.21}$$

After incorporate the spatial part and temporal parts into the Eq. 2.18, the finite element model can be presented in terms of the following matrix form.

$$\sum_{j=1}^{n} M_{ij}{}^e \dot{T}_j + \sum_{j=1}^{n}(K_{ij}{}^e + H_{ij}{}^e)T_j{}^e = F_i^e + P_i^e \tag{2.22}$$

Where:

$$K_{ij}{}^e = \int_{\Omega e} k_x \frac{d\phi_i^e}{dx}\frac{d\phi_j{}^e}{dx} + k_y \frac{d\phi_i^e}{dy}\frac{d\phi_j{}^e}{dy} + k_z \frac{d\phi_i^e}{dz}\frac{d\phi_j{}^e}{dz} d\Omega$$

$$H_{ij}{}^e = \oint_{\Gamma e} \beta \phi_i^e \phi_j{}^e ds \tag{2.23}$$

$$M_{ij}{}^e = \int_{\Omega e} \rho c \phi_i^e \phi_j{}^e d\Omega$$

$$F_i^e = \int_{\Omega e} \phi_i^e f d\Omega + \oint_{\Gamma} q \phi_i^e ds$$

$$P_i^e = \oint_{\Gamma} \phi_i^e T_w ds$$

2.2.2 Wellbore thermal convective effect

To construct the transient thermal profile of the cased hole due to the movement of wellbore fluid, it is necessary to evaluate the heat convective coefficient of the wellbore fluid. Convective heat transfer in the cased hole occurs as a consequence of wellbore fluid flowing past the inner surface of the wellbore. The near wellbore temperature profile and the induced thermal stress are determined by a group of parameters that include the fluid density, fluid heat capacity, rock conductivity, fluid flow rate, fluid viscosity, wellbore diameter, initial temperature distribution etc. Marshall [35] in his work reports that the bottom hole temperature decreases by 12˚C when the fluid density is increased from 1200 kg/m^3 to 1600 kg/m^3. In addition, the increase of the fluid flow rate would decrease the bottomhole temperature.

Heat convective coefficient refers to that the fluid flowing on a solid surface. It can be evaluated using experimental measurements. The thermal convective coefficient in the wellbore is mainly dependent of the fluid properties and wellbore geometry. The thermal convective effect in both Newtonian and nonNewtonian fluids were analyzed[31]. Nusselt number is dimensionless number for describing the rate of heat flow at the interface of fluid and solid surfaces. Eq. 2.24 is used to calculate the heat convective coefficient as long as the Nusselt number, Nu is evaluated.

$$K_f = \frac{\beta D}{Nu} \tag{2.24}$$

Eq. 2.25 is used to compute the Nusellt number of fluid turbulence flow in the wellbore. Reynolds number defines the fluid flowing regime. Prandtl number is a dimensionless number in describing the relation of fluid kinematic viscosity and thermal diffusivity. The Reynolds' number, Re and Prandtl's number, Pr are calculated using Eqs. 2.27 to 2.28.

$$Nu = 0.027\,\mathrm{Re}^{4/5}\,\mathrm{Pr}^{1/3}\left(\frac{u}{u_w}\right) \tag{2.25}$$

$$\beta = \frac{Q}{A \cdot \Delta T} \tag{2.26}$$

$$\mathrm{Re} = \frac{\rho V D}{u} \tag{2.27}$$

$$\mathrm{Pr} = \frac{C_p u}{K_f} \tag{2.28}$$

D, is the wellbore equivalent diameter, k_f, is the thermal conductivity of the wellbore fluid. u is fluid viscosity. β, represents the convective heat transfer coefficient. u_w, is the fluid viscosity at the surface of the wellbore. C_p, is the heat capacity. Q, is the flow rate and A, is the cross area. V, is the fluid velocity and ρ, is the fluid density.

In order to use the above calculations for convective heat transfer coefficient, the parameters in Eqs 2.25 to 2.28 are subject to the constraints of Eqs 2.29 to 2.32.

$$0.7 \le \mathrm{Pr} \le 16700 \tag{2.29}$$

$$\mathrm{Re} \ge 10000 \tag{2.30}$$

$$\frac{L}{D} \ge 10 \tag{2.31}$$

$$D = D_o - D_i \tag{2.32}$$

The above analysis states the heat transfer of turbulent flow in the wellbore. In terms of the laminar flow, Corre [36] analyzed the convective heat transfer coefficient in the laminar flow using the Nusselt number. Eqs. 2.33 to 2.35 indicate calculated procedures for obtaining the convective heat transfer coefficient.

$$K_f = -\frac{1}{\pi}\frac{q\rho C_p}{NuL} In(8 f(n_1)) \tag{2.33}$$

$$f(n_1) = 0.10238\exp(-14.627n_1) + 0.01220\exp(-89.22n_1) + 0.00237\exp(-212n_1) \tag{2.34}$$

Where

$$n_1 = \frac{\pi K_f L}{4q\rho C_p} \tag{2.35}$$

2.2.3 Stress model

This part provides a conceptual basis for solving for the stresses in the casing-cement-formation system and severs two purposes: first illustrates the basic governing formulations associated with the cased-hole instability under the thermo-elasticity assumption. To solve for the down-hole induced stresses and displacements, this part will discuss the numerical discretizing technique for the casing-cement-formation system and the matrix assembling in the finite element model.

The near wellbore stress during down-hole operations is considered to reach a new balance in an extreme short time. Therefore, the quasi-static assumption is appropriate for the instability analysis in the wellbore. The cased hole consists of casing, cement and formation. For each part of the cased-hole system: casing, cement and formation needs satisfy the stress equilibrium constraints. Eqs. 2.36 to 2.38 reveal the force equilibrium equations. Although these equations describe the displacements and stresses in the Cartesian coordinate, they can be expressed in the cylindrical coordinate system, as shown in Appendix A.

$$\rho\frac{\partial^2 u_x}{\partial t^2} - \frac{\partial \sigma_{xx}}{\partial x} - \frac{\partial \sigma_{xy}}{\partial y} - \frac{\partial \sigma_{xz}}{\partial z} - fx = 0 \tag{2.36}$$

$$\rho\frac{\partial^2 u_y}{\partial t^2} - \frac{\partial \sigma_{xy}}{\partial x} - \frac{\partial \sigma_{zy}}{\partial z} - \frac{\partial \sigma_{yy}}{\partial y} - fy = 0 \tag{2.37}$$

$$\rho\frac{\partial^2 u_z}{\partial t^2} - \frac{\partial \sigma_{zy}}{\partial y} - \frac{\partial \sigma_{zx}}{\partial x} - \frac{\partial \sigma_{zz}}{\partial z} - fz = 0 \tag{2.38}$$

The stress is a tensor consisting of the direction and value. In this dissertation, we use the positive sign to represent the tensile stress. The negative sign represents the compressive stress.

Thermal expansion and contraction in thermodynamics describe the size change of a body with the temperature change. The relation between the thermal strain and the temperature change is expressed in Eq. 2.39.

$$\sigma_T = \alpha_T E \Delta T \tag{2.39}$$

The thermal effect in a sealed wellbore annuli can result in the extreme pressure increase. It can cause apparent damages on the casing and production liners in a wellbore. When the fluid temperature in the bottom hole increases from 63 ˚F to 160 ˚F, the induced pressure is recorded to increase from the initial 170 psi to 3600 psi [37].

In a three dimensional coordinate, the relation of stress and strain can be represented in Eqs. 2.40 to 2.42 [38].

$$\varepsilon_x - \alpha_T \Delta T = \frac{1}{E}\left[\sigma_x - \nu\left(\sigma_z + \sigma_y\right)\right] \tag{2.40}$$

$$\varepsilon_y - \alpha_T \Delta T = \frac{1}{E}\left[\sigma_y - \nu\left(\sigma_z + \sigma_x\right)\right] \tag{2.41}$$

$$\varepsilon_z - \alpha_T \Delta T = \frac{1}{E}\left[\sigma_z - \nu\left(\sigma_x + \sigma_y\right)\right] \tag{2.42}$$

After incorporating the thermal effect in Eqs 2.36 to 2.38, the thermo-elasticity governing equations can be stated in Eqs. 2.43 to 2.45. The solutions to the equations include temperature, stress, strain and displacement in the cased hole.

$$(\lambda + G)\frac{\partial \varepsilon_{vol}}{\partial x} + G\frac{\partial^2 u}{\partial x^2} - \frac{\alpha E}{1-2\nu}\frac{\partial T}{\partial x} + f_x = 0 \tag{2.43}$$

$$(\lambda + G)\frac{\partial \varepsilon_{vol}}{\partial y} + G\frac{\partial^2 u}{\partial y^2} - \frac{\alpha E}{1-2\nu}\frac{\partial T}{\partial y} + f_y = 0 \tag{2.44}$$

$$(\lambda + G)\frac{\partial \varepsilon_{vol}}{\partial z} + G\frac{\partial^2 u}{\partial z^2} - \frac{\alpha E}{1-2\nu}\frac{\partial T}{\partial z} + f_z = 0 \tag{2.45}$$

The strain in the case hole can be obtained through the evaluation of relative displacement in the casing-cement-formation system. The general relation of strain and displacement is summarized using Eq. 2.46.

$$\varepsilon_{i,j} = \frac{1}{2}\left(\frac{\partial u_i}{\partial x_j} + \frac{\partial u_j}{\partial x_i}\right) \tag{2.46}$$

The weight functions are used to approximate integrals in the governing equations. The weight functions w_1, w_2 and w_3 are the first variations of u_x u_y u_z, which are the three components of displacement vector. Eqs. 2.47 to 2.49 indicate that the same shape function is used in the approximation of displacements.

$$u_x = \sum_{j=1}^{n} u_{xj}{}^{e}\phi_j{}^{e}(x,y,z) \tag{2.47}$$

$$u_y = \sum_{j=1}^{n} u_{yj}{}^{e}\phi_j{}^{e}(x,y,z) \tag{2.48}$$

$$u_z = \sum_{j=1}^{n} u_{zj}{}^{e}\phi_j{}^{e}(x,y,z) \tag{2.49}$$

The subsequent step is to solve for Eqs 2.43 to 2.45 using the above shape functions. Eq. 2.50 reveals the matrix form over a typical element. The Integral terms of all the matrices coefficients are stated in Appendix B.

Depending on the specific location of each element in the cased hole system, Eq. 2.50 denotes different displacements. The interfaces of casing, cement and formation are fully bonded. After assembling all of the discretized elements, the global matrix for representing the casing-cement-formation system is easily obtained.

$$\begin{bmatrix} K^{11} & K^{12} & K^{13} \\ K^{21} & K^{22} & K^{23} \\ K^{31} & K^{32} & K^{33} \end{bmatrix} \begin{Bmatrix} U_x \\ U_y \\ U_z \end{Bmatrix} + \begin{bmatrix} K^{T1} \\ K^{T2} \\ K^{T3} \end{bmatrix} = \begin{bmatrix} F^1 \\ F^2 \\ F^3 \end{bmatrix} \tag{2.50}$$

Under plain strain assumption, the dimension of the well in the axial direction is sufficiently large compared with the dimensions in the other two directions. It will lead to the following relations in Eq. 2.51.

$$\varepsilon_z = \gamma_{xz} = \gamma_{yz} = 0 \tag{2.51}$$

Eq. 2.52 states the relation of stress to strain under the plain strain assumption in an isotropic material. The thermal effect is considered to zero effect on the shear stress[38].

$$\frac{E}{(1+\nu)(1-2\nu)} \begin{bmatrix} 1-\nu & \nu & 0 \\ \nu & 1-\nu & 0 \\ 0 & 0 & \dfrac{1-2\nu}{\nu} \end{bmatrix} \begin{Bmatrix} \varepsilon_x \\ \varepsilon_y \\ \gamma_{xy} \end{Bmatrix} + \begin{Bmatrix} \dfrac{\alpha E \Delta T}{1-2\nu} \\ \dfrac{\alpha E \Delta T}{1-2\nu} \\ 0 \end{Bmatrix} = \begin{Bmatrix} \sigma_x \\ \sigma_y \\ \tau_{xy} \end{Bmatrix} \tag{2.52}$$

2.3 Boundary conditions

Boundary conditions in a stress model include the natural boundary conditions specifying the boundary stresses and the essential boundary conditions specifying the displacements [39]. The boundary conditions in our study consist of stress and displacement specified at inner surface of casing and outer surface of formation in 2D system. The overburden and bottom burden stress will be needed in the 3D system.

Eqs. 2.53 and 2.54 state the natural boundary conditions in the stress model on the surface, Γ_σ

$$\hat{t}_x = \sigma_{xx} n_x + \sigma_{xy} n_y \tag{2.53}$$

$$\hat{t}_y = \sigma_{yy} n_y + \sigma_{xy} n_x \tag{2.54}$$

Essential boundary conditions have the following forms, as shown in Eqs. 2.55 to 2.56.

$$\hat{u}_x = u_x \tag{2.55}$$

$$\hat{u}_y = u_y \tag{2.56}$$

n_x and n_y denote the components of the unit normal vector on the boundary Γ; $\hat{t}_x$ and $\hat{t}_y$ indicate the components of the specified traction vector, $\hat{u}_x$ and $\hat{u}_y$ are the components of the specified displacement vectors.

2.4 Failures criteria

We investigate the induced stress evolution in the cased hole under HPHT conditions and discuss the possible instability of casing-cement system caused by the induced stress. To investigate the cased-hole stress evolution, we assume that the casing-cement-formation system would not fail when the induced stress exceeds the material strength.

Mechanical failure is a term that describes the consequence of stress imposing on a body is greater than the material strength. In practice, the casing-cement-formation system can fail even it still under the material yield point. After the elastic phase, the deformed casing-cement-formation system cannot return to its original size when the applied loads are moved. It is thereby expected that the casing-cement-formation system suffers from the non-reversible deformation in the plastic phase. The general deformation $d\varepsilon_{ij} = d\varepsilon_{ij}^{\ e} + d\varepsilon_{ij}^{\ p}$ consists of the elastic and plastic parts.

Different failure modes are available to determine the onset of wellbore failure. Von-Mise failure and Drucker-Prager failure are widely used to calibrate the uncemented borehole failure. In the cased hole, the failure of casing-cement system more like results from tensile and compressive deformation. Cement sheath and rock

have similar mechanical attributes. The shear failure can be determined using Mohr-Coulomb failure criterion in Eq. 2.57.

$$\tau = \sigma \tan(\varphi) + C \tag{2.57}$$

τ is the shear strength of rock, σ is the normal stress, C is the cohesion strength, φ is the friction angle. These parameters can be calculated through Eqs. 2.58 to 2.59.

$$\tau = \frac{\sigma_1 + \sigma_3}{2} \cos\varphi \tag{2.58}$$

$$\sigma = \frac{\sigma_1 + \sigma_3}{2} - \frac{\sigma_1 - \sigma_3}{2} \sin\varphi \tag{2.59}$$

Von-MISE criteria are used to decide the initial yielding point of material. The combination of three principal stresses and shear stresses in Eq. 2.60 is used to determine the equivalent stress.

$$\sigma_{eqv} = \sqrt{\sigma_r{}^2 + \sigma_\theta{}^2 + \sigma_z{}^2 - \sigma_r\sigma_\theta - \sigma_r\sigma_Z - \sigma_Z\sigma_\theta + 3\tau_{\theta Z}} \tag{2.60}$$

The tensile failure in the wellbore occurs when the minimum effective stress inside the casing-cement-formation system is greater than the tensile strength of the material, as shown in Eq. 2.61. The failure typically occurs inside cement sheath and formation since both mediums exhibit very low tensile resistance.

$$\sigma'_{\min} > \sigma^* \tag{2.61}$$

Casing has both high compressive and tensile tolerance. The compressive strengths of cement sheath and formation are higher than the tensile strengths. The Drucker-Prager model is served as a compressive failure criteria, as shown in Eqs. 2.62 to 2.65 [40].

$$J_2 = AJ_1^{eff} + B \tag{2.62}$$

$$J_1^{eff} = \frac{\sigma_1 + \sigma_2 + \sigma_3}{3} \tag{2.63}$$

$$A = \frac{2\sqrt{2}\sin\varphi}{3 - \sin\varphi} \tag{2.64}$$

$$B = \frac{2\sqrt{2}\cos\varphi}{3 - \cos\varphi} \tag{2.65}$$

3. NUMERICAL INTEGRATION TO THE FINITE ELEMENT MODELS

The development of oil and gas wells in HPHT conditions are considered expensively. The casing-cement-formation system with the curved boundary conditions consists of multi mediums. An analytical solution to the instability problem in the casing-cement-formation system is impractical. In the absence of enough down-hole survey information, numerical modeling technique as an alternative way is used to evaluate the well integrity.

Finite element method has become an effective tool for solving complex structural and fluid problems. The finite element method based on an accurate approximation against the analytical solution is used by discretizing the continuous problem into many consecutive elements. This method includes three steps in a typical analysis. The physical problems are represented by a number of elements after the numerical discretization. Second, all of the matrices of the elements equations are assembled in a global coordinate. After solving the assembled equation, the approximation solution to the original problem is postprocessed.

The casing-cement-formation domain is divided into small subdomains composed of a series of nodes. The displacements and stresses on all nodes in the local coordinates are obtained after the govern equation in each subdomain is solved. A larger finite element system will require much computation time and iteration steps, an additional optimization approach should be used to minimize these factors.

Through comparing different finite element simulator, Ansys is used as a major program to solve the finite element models. The following is to discuss the processes that the finite element models are solved using approximation functions. The interface for connecting the stresses model and the thermal models are programmed based on Fortran language. The main step for using this simulator is to define analysis type and specify boundary conditions as well as gridding the physical geometry.

Plain strain theory assumes the dimension in longitudinal axial direction much longer compared with its other two directions. The axial displacement caused by the

uniform load in the cased hole is negligible, so that plain strain is applicable for the analysis in 2D. In the following finite element analysis, the quadrilateral element in 2D and the brick element in 3D are chosen to describe the numerical evaluation over integral expressions.

Accuracy of a finite element scheme measures the closeness between analytical solution and the simulated solution. Fig. 3.1 and Fig. 3.2 show the radial stress and tangential stress inside the casing when suffering from the internal burst pressure of 1000 psi. The analytical solution exhibits a premium match with the solution to the numerical model.

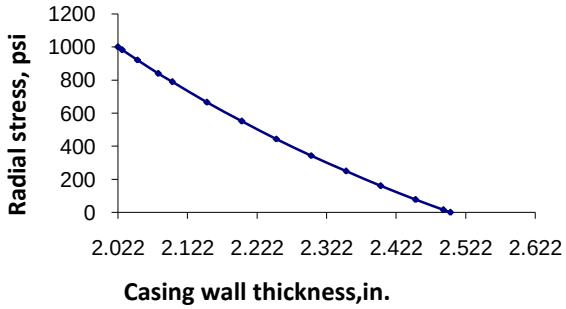

Fig. 3. 1 Radial stress inside the casing by numerical and analytical solutions

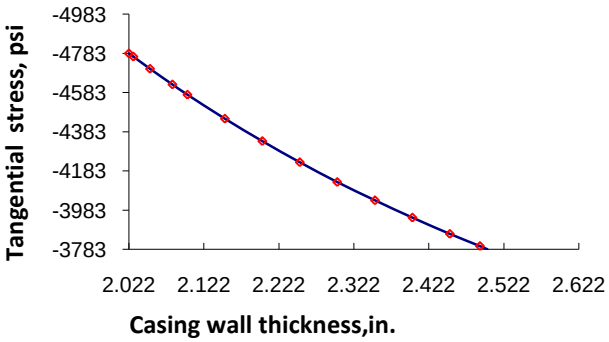

Fig. 3. 2 Tangential stress inside the casing by numerical and analytical solutions

For instance, the cased-hole domain is discretized into small domains that represented by mathematical equations in Eq 2.23. The coefficients of the mathematical equations are in the form of integrals. Because of the complicated integrals in the finite

element model, numerical evaluation for the integrals is preferred. Therefore, the integrands in the integrals are evaluated at the integration points and then all the evaluated integrands in are summed together as the product of the original integral approximation formula. Eq. 3.1 indicates the expression of converting the integral to the numerical approximation.

$$\int_{\Omega e} f(\xi,\eta)d\zeta d\eta = \sum_{i=1}^{n} W_i f(\xi_{i,}\eta_i) \tag{3.1}$$

3.1 Two-Dimensional Numerical integration

The quadrilateral element with four nodes is used. For the purpose of integration, the actual element shape is transformed into a master element shape. The integration of the quadrilateral element requires that integrals are expressed in a master element. Eq 3.2 states that the integrand is expressed against the coordinates (ξ,η) of the master element. ϕ_j is the shape function over the master element[39].

$$x = \sum_{j=1}^{m} x_j{}^{e}\phi_j{}^{e}(\xi,\eta) \tag{3.2}$$

$$y = \sum_{j=1}^{m} y_j{}^{e}\phi_j{}^{e}(\xi,\eta) \tag{3.3}$$

To implement the numerical integration, the shape functions of the quadrilateral element in a local coordinate is expressed in Eqs. 3.4 to 3.7.

$$\phi_1 = \frac{1}{4}(1-\xi)(1-\eta) \tag{3.4}$$

$$\phi_2 = \frac{1}{4}(1+\xi)(1-\eta) \tag{3.5}$$

$$\phi_3 = \frac{1}{4}(1-\xi)(1+\eta) \tag{3.6}$$

$$\phi_4 = \frac{1}{4}(1+\xi)(1+\eta) \tag{3.7}$$

J is known as Jacobian matrix in the finite element model, as shown in Eq. 3.8.

$$[J]=\begin{bmatrix}\frac{\partial x}{\partial \xi} & \frac{\partial y}{\partial \xi}\\ \frac{\partial x}{\partial \eta} & \frac{\partial y}{\partial \eta}\end{bmatrix}^{e}=\begin{bmatrix}\sum_{i=1}^{m} x_i \frac{\partial \phi i}{\partial \xi} & \sum_{i=1}^{m} y_i \frac{\partial \phi i}{\partial \xi}\\ \sum_{i=1}^{m} x_i \frac{\partial \phi i}{\partial \eta} & \sum_{i=1}^{m} y_i \frac{\partial \phi i}{\partial \eta}\end{bmatrix} \tag{3.8}$$

In order to compute the global derivatives $\psi_i^{\,e}$, the inversion of Jacobian matrix, J^{-1} is required. The det[J] has to be nonzero in order to make the matrix invertible. Eq. 3.9 is obtained after make the coordinate transformation.

$$\begin{bmatrix}\frac{\partial \phi_i^{\,e}}{\partial x}\\ \frac{\partial \phi_i^{\,e}}{\partial y}\end{bmatrix}=\left[J^{-1}\right]\begin{bmatrix}\frac{\partial \phi_i^{\,e}}{\partial \xi}\\ \frac{\partial \phi_i^{\,e}}{\partial \eta}\end{bmatrix}=\begin{bmatrix}\frac{\partial \xi}{\partial x} & \frac{\partial \eta}{\partial x}\\ \frac{\partial \xi}{\partial y} & \frac{\partial \eta}{\partial y}\end{bmatrix}\begin{bmatrix}\frac{\partial \phi_i^{\,e}}{\partial \xi}\\ \frac{\partial \phi_i^{\,e}}{\partial \eta}\end{bmatrix} \tag{3.9}$$

After including the Jacobian matrix, the main integral expressions in the matrix equation of heat transfer model can be expressed in Eqs 3.10 to 3.12.

$$\begin{aligned}K_{ij}^{\,e}=\int_{-1}^{1}\int_{-1}^{1} &\{k_x[(\frac{\partial \xi}{\partial x}\frac{\partial \phi_i^{\,e}}{\partial \xi}+\frac{\partial \eta}{\partial x}\frac{\partial \phi_i^{\,e}}{\partial \eta})(\frac{\partial \xi}{\partial x}\frac{\partial \phi_j^{\,e}}{\partial \xi}+\frac{\partial \eta}{\partial x}\frac{\partial \phi_j^{\,e}}{\partial \eta})]\\ &+k_y[(\frac{\partial \xi}{\partial y}\frac{\partial \phi_i^{\,e}}{\partial \xi}+\frac{\partial \eta}{\partial y}\frac{\partial \phi_i^{\,e}}{\partial \eta})(\frac{\partial \xi}{\partial y}\frac{\partial \phi_j^{\,e}}{\partial \xi}+\frac{\partial \eta}{\partial y}\frac{\partial \phi_j^{\,e}}{\partial \eta})]\}Jd\zeta d\eta\end{aligned} \tag{3.10}$$

$$M_{ij}=\int_{-1}^{1}\int_{-1}^{1}\rho c\phi_i^{\,e}\phi_j^{\,e}Jd\xi d\eta \tag{3.11}$$

$$F_i^{\,e}=\int_{-1}^{1}\int_{-1}^{1}\phi_i^{\,e}fJd\xi d\eta+\int_{-1}^{1}\int_{-1}^{1}q\phi_i^{\,e}Jd\xi d\eta \tag{3.12}$$

3.2 Three-Dimensional Numerical integration

The 3D modeling uses the brick element of 8 nodes at each corner points. The corresponding shape functions are expressed in Eq. 3.13.

$$\phi_i(\xi,\eta,\psi)=\frac{1}{8}(1+\xi\xi_i)(1+\eta\eta_i)(1+\psi\psi_i) \tag{3.13}$$

To obtain the Jacobian matrix for the 3D numerical integration, it is required to express $\phi_i^e(x,y,z)$ in the local coordinates ζ,η,ψ, as shown in Eqs. 3.14 to 3.16.

$$\frac{\partial\phi_i^e}{\partial\xi}=\frac{\partial\phi_i^e}{\partial x}\frac{\partial x}{\partial\xi}+\frac{\partial\phi_i^e}{\partial y}\frac{\partial y}{\partial\xi}+\frac{\partial\phi_i^e}{\partial z}\frac{\partial z}{\partial\xi} \tag{3.14}$$

$$\frac{\partial\phi_i^e}{\partial\eta}=\frac{\partial\phi_i^e}{\partial x}\frac{\partial x}{\partial\eta}+\frac{\partial\phi_i^e}{\partial y}\frac{\partial y}{\partial\eta}+\frac{\partial\phi_i^e}{\partial z}\frac{\partial z}{\partial\eta} \tag{3.15}$$

$$\frac{\partial\phi_i^e}{\partial\psi}=\frac{\partial\phi_i^e}{\partial x}\frac{\partial x}{\partial\psi}+\frac{\partial\phi_i^e}{\partial y}\frac{\partial y}{\partial\psi}+\frac{\partial\phi_i^e}{\partial z}\frac{\partial z}{\partial\psi} \tag{3.16}$$

Therefore, the Jacobian matrix in the 3D model is represented by Eq. 3.17.

$$[J]=\begin{bmatrix}\frac{\partial x}{\partial\xi} & \frac{\partial y}{\partial\xi} & \frac{\partial z}{\partial\xi}\\ \frac{\partial x}{\partial\eta} & \frac{\partial y}{\partial\eta} & \frac{\partial z}{\partial\eta}\\ \frac{\partial x}{\partial\psi} & \frac{\partial y}{\partial\psi} & \frac{\partial z}{\partial\psi}\end{bmatrix}^e=\begin{bmatrix}\sum_{i=1}^m x_i\frac{\partial\phi i}{\partial\xi} & \sum_{i=1}^m y_i\frac{\partial\phi i}{\partial\xi} & \sum_{i=1}^m z_i\frac{\partial\phi i}{\partial\xi}\\ \sum_{i=1}^m x_i\frac{\partial\phi i}{\partial\eta} & \sum_{i=1}^m y_i\frac{\partial\phi i}{\partial\eta} & \sum_{i=1}^m z_i\frac{\partial\phi i}{\partial\eta}\\ \sum_{i=1}^m x_i\frac{\partial\phi i}{\partial\psi} & \sum_{i=1}^m y_i\frac{\partial\phi i}{\partial\psi} & \sum_{i=1}^m z_i\frac{\partial\phi i}{\partial\psi}\end{bmatrix} \tag{3.17}$$

In order to compute the global derivatives ${\psi_i}^e$ in the 3D model, the Jacobian matrix for the finite element model is required inversely. The K, M and F in the finite element model can be expressed in Eqs. 3.18 to 3.20.

$$\begin{aligned}{K_{ij}}^e=\int_{-1}^{1}\int_{-1}^{1}\int_{-1}^{1}\ &\{k_x[(\frac{\partial\xi}{\partial x}\frac{d{\phi_i}^e}{d\xi}+\frac{\partial\eta}{\partial x}\frac{d{\phi_i}^e}{d\eta}+\frac{\partial\psi}{\partial x}\frac{d{\phi_i}^e}{d\psi})(\frac{\partial\xi}{\partial x}\frac{d{\phi_j}^e}{d\xi}+\frac{\partial\eta}{\partial x}\frac{d{\phi_j}^e}{d\eta}+\frac{\partial\psi}{\partial x}\frac{d{\phi_j}^e}{d\psi})]\\ &+k_y[(\frac{\partial\xi}{\partial y}\frac{d{\phi_i}^e}{d\zeta}+\frac{\partial\eta}{\partial y}\frac{d{\phi_i}^e}{d\eta}+\frac{\partial\psi}{\partial y}\frac{d{\phi_i}^e}{d\psi})(\frac{\partial\xi}{\partial y}\frac{d{\phi_j}^e}{d\zeta}+\frac{\partial\eta}{\partial y}\frac{d{\phi_j}^e}{d\eta}+\frac{\partial\psi}{\partial y}\frac{d{\phi_j}^e}{d\psi})]\\ &+k_z[(\frac{\partial\xi}{\partial z}\frac{d{\phi_i}^e}{d\zeta}+\frac{\partial\eta}{\partial z}\frac{d{\phi_i}^e}{d\eta}+\frac{\partial\psi}{\partial z}\frac{d{\phi_i}^e}{d\psi})(\frac{\partial\xi}{\partial z}\frac{d{\phi_j}^e}{d\zeta}+\frac{\partial\eta}{\partial z}\frac{d{\phi_j}^e}{d\eta}+\frac{\partial\psi}{\partial z}\frac{d{\phi_j}^e}{d\psi})]\}Jd\zeta d\eta d\psi\end{aligned} \tag{3.18}$$

$$M_{ij}{}^{e} = \int_{-1}^{1}\int_{-1}^{1}\int_{-1}^{1} \rho c \phi_i{}^{e} \phi_j{}^{e} J d\zeta d\eta d\psi \tag{3.19}$$

$$F_i^{e} = \int_{-1}^{1}\int_{-1}^{1}\int_{-1}^{1} \phi_i{}^{e} f J d\zeta d\eta d\psi + \int_{-1}^{1}\int_{-1}^{1}\int_{-1}^{1} q \phi_i{}^{e} J d\zeta d\eta \tag{3.20}$$

4. CASING/CEMENT/FORMATION CRITICAL BEHAVIOR

The casing-cement system plays an important role in zonal isolation, preventing unwanted fluid communication between wellbore and production intervals. During drilling and well completing in deep formations, casing and cement sheath failures have been reported increasingly in recent years. It is expected that the evaluating stress in the casing-cement system before drilling/well completion can help ensure future well integrity. In other words, an improper understanding of down-hole stress evolution in the casing-cement system can cause serious well damage that results in expensive remediation, ultimately leads to well abandonment.

Perforation in the casing-cement system does create stress concentration in the wellbore. The non-uniform stress distribution near the perforation also induces the instability in the perforation zones. The casing-cement failures are reported increasingly in the non-perforated zones, particularly in the development of unconventional oil and gas wells.

Beside the drilling stage in HPHT wells, Hydraulic fracturing treatment and extreme production drawdown in the production stage can cause the mechanical instability in the casing-cement system. Many efforts on cemented well stability concentrate on either the casing and cement mechanical analysis, or investigation on the static behavior of formation [4, 6, 13, 14, 16, 41]. In order to improve casing and cementing job design, it is worthwhile to understand the mechanical responses inside the casing-cement system at non-perforation zones. Without considering the down-hole stress evolution in the wellbore due to the fluid movement, the mechanical behavior of the cemented sections cannot be properly evaluated.

This chapter emphasizes the effect of wellbore fluid on the stability of casing and cement in the cased hole. The objective is to investigate the state of stress inside casing/cement in differing down-hole conditions. We performed numerical simulations to evaluate the casing-cement response in the well cooling and heating effects. To

construct the relation of heat transfer against the induced stress in the cased-hole model, we investigated the thermal stress inside casing/cement with time.

Our study shows that a critical induced stress inside the casing/cement exists during the wellbore fluid movement. In the well heating process caused by the hot wellbore fluid, the maximum compressive radial stress at the interface of casing-cement has been increased by up to 3000 psi. Then it slightly decreased after 1 hour. To calibrate the tangential and Von-Mise failures in the casing-cement system, we analyzed the tangential stress and equivalent stress with time in the cased hole. It is found that the stress variation in both the heating process and the cooling process is negligible after 24-hour wellbore fluid movement.

4.1 Statement

A deep well is typically subject to the small margin of drilling window. The thermal effect near wellbore will change along with the wellbore fluid circulation. Temperature imbalance between wellbore fluid and the surrounding formation induces the wellbore contraction or expansion.

Damages caused by the thermal effect in the casing-cement system tend to be more serious when the well is in the existence of casing eccentricity, pre-existing casing deformation and gas channels in the cement sheath. Any subsequent remediation for the damages is extremely expensive in the cost of production loss, equipment replacement and services.

The cooling effect in a well occurs when the wellbore fluid is cooler than near formation. Either drilling mud or well completion fluid can induce the cooling effect. Oppositely, the hot steam injection in a well can create the heating effect. The heating effect also occurs in a production well when the produced oil is hotter than the casing-cement system in the upper well zone. The magnitude of cooling effect and heating effect depends on the temperature difference of wellbore fluid against formation.

Both well heating and cooling effects may cause damages in casing-cement system. In the process of wellbore fluid movement in a well, the temperature profile in

the well changes with time. The interacting effect of wellbore fluid and the casing-cement-formation system becomes critically important and then the state of stress inside casing/cement has to be quantitatively estimated.

4.2 Methodology

Finite element method is used because it is widely used in solving for mechanical and thermal engineering problems. In order to solve for the stress and strain inside casing/cement in the wellbore, the casing-cement-formation system is divided into small elements.

This section discusses the mechanical instability inside casing/cement caused by the heating and cooling effects in the cased hole. The thermal stress inside casing/cement is sensitive to temperature variation. We present the thermal behaviors in the cased hole such as temperature profile, thermal flux and thermal gradient.

A dedicated gridding system for the finite element model is fundamental step for the success of the cased-hole instability analysis. It is able to generate accurate simulation results. The Finite element modeling based on nodal solutions requires a proper location distribution for the nodes of each element. As shown on the radial lines of Fig. 4.1, the size of element is in an incremental order. The dense meshes for the casing-cement system are preferred to produce high resolution of stress concentration in the cased hole.

In order to solve for displacements and temperature in the finite element model, the thermal properties of casing, cement and formation are required. The fluid properties have been given in the Table 4.2. Formation young's modulus and Poisson ratio are defined in this model.

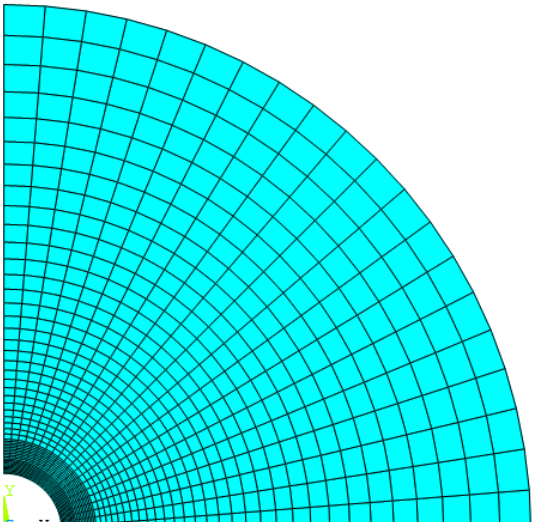

Fig. 4.1 Cross section of the quarter cased-hole model

An infinity boundary for the numerical model is preferred in this system, but not feasible in the numerical computation. The common accepted effective region is approximate 5 to 7 times of the bore-hole radius [3, 14]. This model includes the 40-in diameter formation, which is approximate 10 times of the casing radii. The casing of outer diameter of 5.5 in. and inner diameter of 4.408 in. is designed. The casing is cemented in a 7-in. open hole. All other material properties and geometry properties are listed in Table 4.1 and Table 4.2 respectively. To investigate the difference of mechanical responses near the wellbore in the heating and cooling processes, we proposed three cases in differing down-hole conditions, as listed in Table 4.3.

Table 4.1 Properties of the casing, cement and formation

	Elastic modulus, psi	Poisson's ratio	Density, g/cm^3	Thermal conductivity, Btu/ft.hr. ˚F	Specific heat, Btu/lb. ˚F	Thermal expansion, ˚F ^−1
Casing	2.80E+07	0.3	7	7.2	0.12	1.8E–5
Cement	3.00E+06	0.24	1.8	0.6	0.5	1.2E–5
Sandstone	6.00E+06	0.2	2	0.48	0.4	1.4E–5
Shale	4.00E+06	0.35	2	0.24	0.3	1.4E–5

Table 4.2 The geometry of cased hole

Wellbore temperature when returning	350
Formation T@ upper section, ˚F	300
Casing Type	P110/55
Casing ID, in.	4.408
Casing OD, in.	5.5
cement sheath ID, in.	5.5
Cement sheath OD, in.	7
Formation ID, in.	7
Formation OD, in.	40
Fluid specific heat, btu/lb. ˚F	0.45
Fluid thermal conductivity, btu/ft.hr. ˚F	1.0
Fluid thermal convective, btu/ft^2.hr. ˚F	288
Mud circulating Time , in.	48

Table 4.3 Profile of fluid temperature and burst pressure

	Fluid T, ˚F	Rock T, ˚F	Initial T, ˚F	Burst pressure, psi	Formation horizontal stress, psi
Case 1	350	300	300	7000	8100
Case 2	300	350	350	7000	8100
Case 3	100	350	350	7000	8100

4.3 Heating effect

The well heating effect usually occurs at several different stages. The drilling fluid enters the drilling pipe from the surface. The formation geothermal energy heats the drilling fluid at the lower section in the wellbore. Then the heated fluid from the bottom hole fluid will heat upper casing-cement systems in the wellbore when it returns to the surface. Secondly, in a production stage, the produced hydrogen from a deep reservoir will create the heating effect at the upper cemented section when it travels in the wellbore. Thirdly, well stimulation such as steam injection will result in the extreme expansion in the casing-cement system. To maintaining the integrity of cased hole during the life of well, it is necessary to under the state of stress inside casing/cement caused by the heating effect.

The first case aims to reveal the mechanical response of the casing-cement-formation system caused by the heating effect through analyzing the variation of induced stress in the finite element model. The state of stress inside casing/cement is calculated using the wellbore fluid temperature of 350 ˚F and formation temperature of 300 ˚F. We implement the numerical simulation by assuming the fluid pressure of 7000 psi acting on the inner surface of 4 ½ in. diameter casing. The horizontal formation stress of 8100 psi is proposed to act on the outer boundary of formation.

Most properties of the cased-hole model exhibit linear behavior, which is independent of the stress and temperature variations. However, the thermal conductivity

of casing is sensitive of temperature variation, the casing shows a nonlinear thermal relation, as plotted in Fig. 4.2.

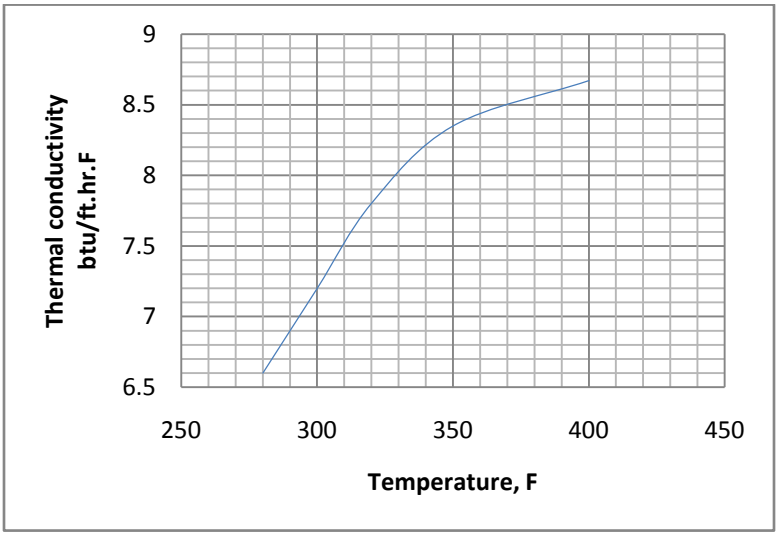

Fig. 4.2 Casing thermal conductivity

Figs. 4.3 and 4.4 show the thermal behaviors inside casing/cement in event of the wellbore fluid movement in 48 hours. The thermal flux indicates that the rate of heat energy crosses through the casing surface. The mathematical form of thermal flux is expressed using $\oint_s \vec{\phi}_q . \vec{ds}$. The maximum thermal flux of 54 btu/hr.in^2 occurred at the inner boundary of wellbore, in Fig. 4.3. It declined sharply along with the movement of wellbore fluid. After one hour fluid movement, the difference of thermal flux inside the casing/cement at two consecutive steps becomes small.

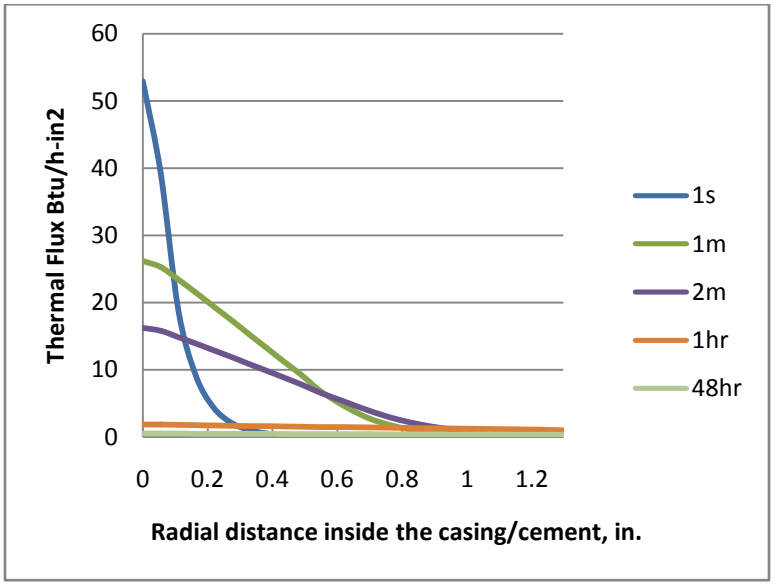

Fig. 4.3 Thermal flux through casing/cement by the heating effect in 48 hours

Thermal gradient describes the rate and direction of heat transfer. It is shown in the form of $\nabla T = (\frac{\partial T}{\partial x}, \frac{\partial T}{\partial y}, \frac{\partial T}{\partial z})$. Fig. 4.4 shows the thermal gradient quickly decreased inside the casing in the first hour. In the casing-cement-formation system, the maximum thermal gradient of 87 ˚F/in occurred at the inner boundary of wellbore. Through the comparison of the thermal gradient at 12 hour with that at 48 hour, the thermal equilibrium inside the casing is concluded to reach after 12 hours.

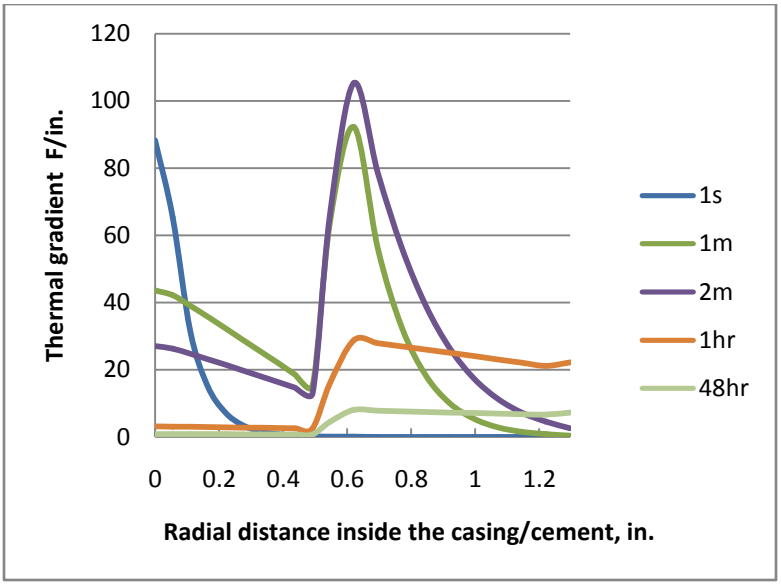

Fig. 4.4 Thermal gradient through casing/cement by the heating effect in 48 hours

The induced radial stress inside casing/cement is an important indicator to determine the cased-hole structural instability. Radial cracking is one of the failures in casing-cement system [12]. On the plot of radial stress in Fig. 4.5, the compressive radial stress increased through the casing and reached the maximum value at the interface of casing and cement sheath. The radial stress decreased inside the cement-formation system in the radial direction, it ultimately arrived the original formation horizontal stress. Apparently, the maximum radial stress at the casing-cement interface increased and reached a critical maximum value at 1 hour, and then it decreased slightly from 1 hour to 48 hours.

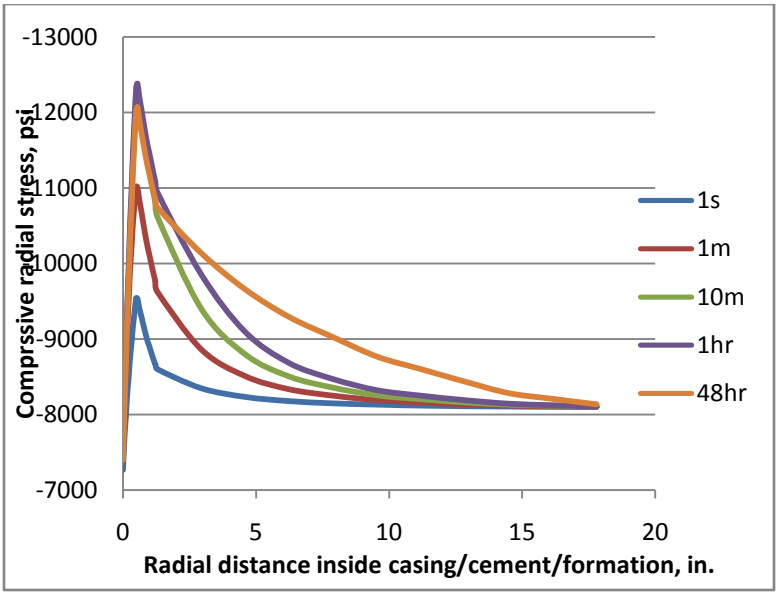

Fig. 4.5 Radial stress of casing/cement/formation by the heating effect

Fig. 4.6 shows the maximum induced thermal radial stress caused by the process of heating effect in the casing-cement-formation system, as indicated by the blue line. The red line reveals the radial stress inside the casing-cement-formation system without considering the thermal effect. Due to the hot wellbore movement, the compressive radial stress at the casing-cement interface has increased by approximately 3000 psi at the end of first hour. Beyond the areas over 16 in. in the radial direction of wellbore, the heating effect has little influence on the cased-hole system in terms of the radial stress variation.

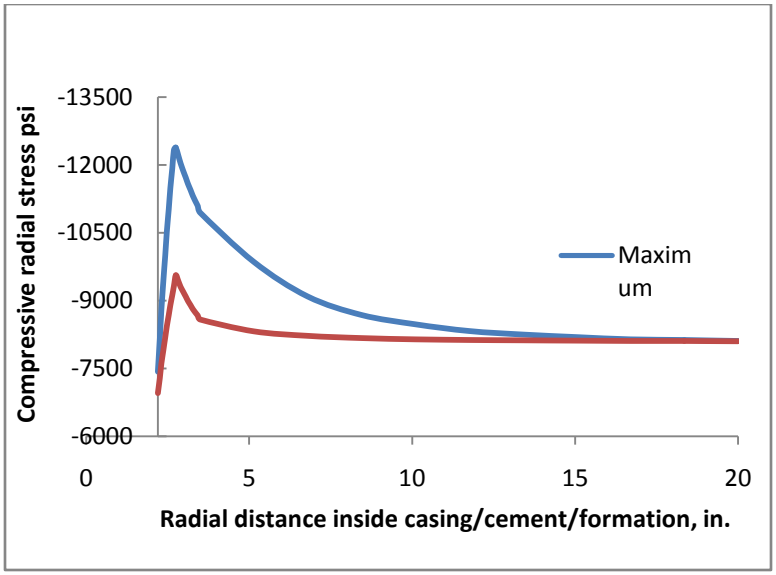

Fig. 4.6 Comparison of radial stress by thermal and non-thermal effects

Tangential stress inside casing/cement is used to predict the possible tangential cracking. Casing/cement in the cased hole will suffer from tangential instability when the effective minimum tangential stress is greater than the casing/cement strength. Fig. 4.7 has shown that a relative large compressive tangential stress at the inner boundary of casing. It increased from 27470 psi at the beginning to 38391 psi at 1 hour, and then slightly dropped to 36212 psi by the end of 48 hours. In other words, the capacity of tensile resistance inside the casing/cement rises approximate 40% during the circulation of wellbore fluid.

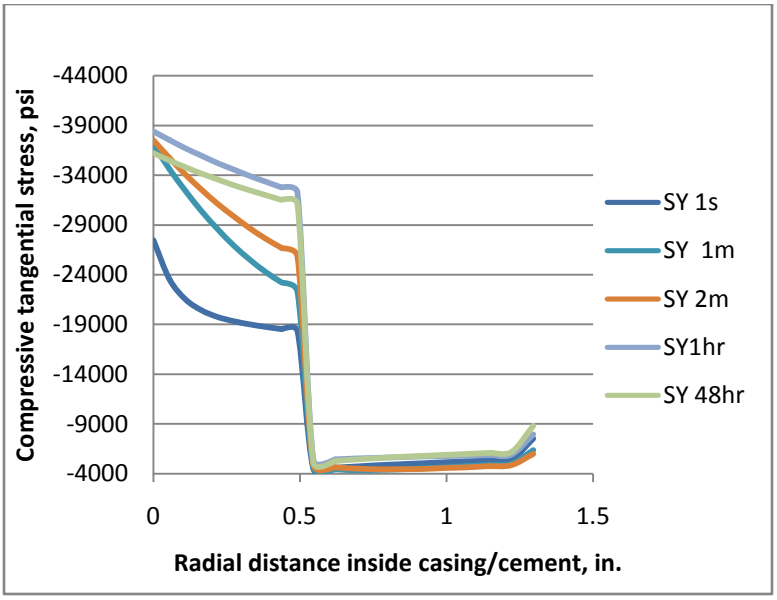

Fig. 4.7 Tangential stress of casing/cement by the heating effect in 48 hours

Von-MISE stress is normally accepted to determine the initial yielding point of material. It is a comprehensive expression of principal stresses and shear stresses, as revealed in Eq 2. 55. In our case, the Von-Mise criteria can be analyzed based on the Equivalent stress.

Fig. 4.8 shows that most areas inside the casing experiences severe equivalent stress. At the area closed to inner boundary of cement, the equivalent stress inside the casing drops importantly. In terms of the equivalent stress variation in the cased hole, the heating effect due to wellbore fluid movement has little influence on the cement sheath. The inner wall of casing will suffer from 31077-psi equivalent stress of at the 1 hour. And then the equivalent stress decreases to 29896 psi by the end of 48 hours.

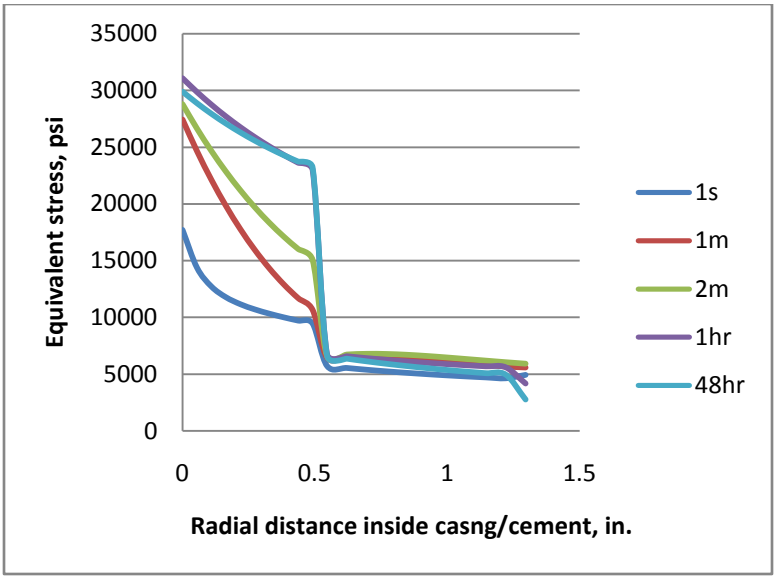

Fig. 4. 8 Equivalent stress of casing/cement by the heating effect in 48 hours

The induced formation stress is used to evaluate the formation mechanical responses in the cased-hole model. Fig. 4.9 plots that the compressive radial stress of formation at the cement-formation interface increased by approximate 2000 psi. The results indicate that the maximum compressive radial stress occurs at inner surface of formation and nonlinearly declines inside the formation in the radial direction.

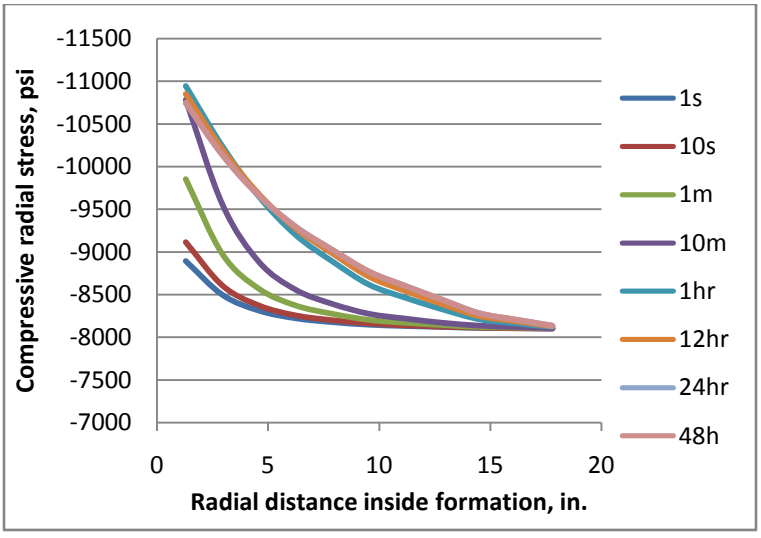

Fig. 4.9 Formation radial stress by the heating effect in 48 hours

In order to show the formation mechanical response at different locations inside the formation, a group data set of positions inside the formation is picked to track the variation of formation radial stress.

Fig 4.10 has revealed the radial stress inside formation with time at different locations. Each curve on this figure represents a specific location inside the formation. The blue curve, on the top, indicates the radial distance of 3.5 in. in the radial direction, which reveals the radial stress variation at the inner boundary of formation. The maximum compressive radial stress inside the formation caused by the wellbore heating effect is predicted at this inner boundary. It increases with time and will reach a maximum value around 1 hour, then slightly dropped afterwards. If a longer fluid movement in the wellbore is permit, the radial stress at the other locations will increase until reaching their own critical values.

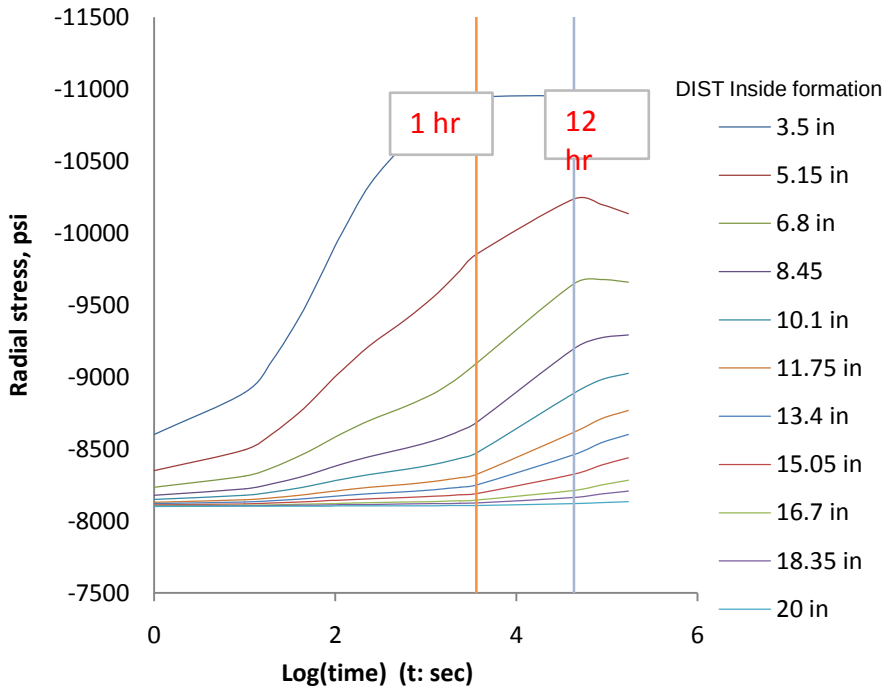

Fig. 4.10 Formation radial stress at the fixed locations by the heating effect in 48 hours

In the variation of tangential stress caused by the well heating effect, we obtain two different mechanical behaviors inside the formation. Fig 4.11 reveals that the compressive tangential stress at the first 10 minutes nonlinearly decreases at the inner boundary of the formation. The far field of formation has not been significantly affected by the wellbore fluid movement. After 1 hour, the compressive tangential stress increases at the inner interface of formation. Meanwhile, the compressive tangential stress at the far field of formation decreases accordingly.

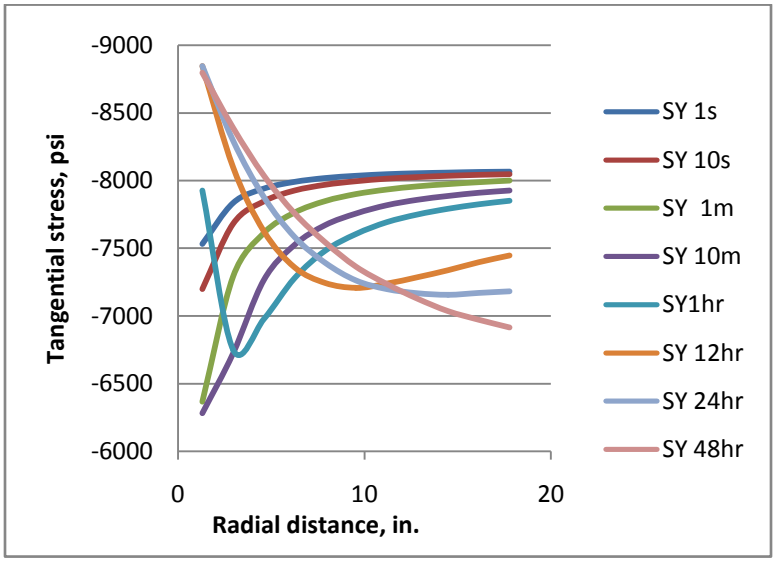

Fig. 4.11 The formation tangential stress by the heating effect in 48 hours

4.3.1 Tectonic stress

In the previous section, we present the effect of formation on the well integrity in the casing-cement system based on the equal formation horizontal stresses. The critical maximum stress at the casing-cement interface is identified.

Formation horizontal stresses are caused by the rock vertical overburden. The stresses can be expressed using rock Poisson's ration and Young's modulus. The tectonic effect of formation is associated with rock movement because of the uplifting and erosion effects. The effect of formation tectonics will result in the unequal formation horizontal stresses. Fig. 4.12 reveals three principal stresses of Sigma-Z, Sigma-X and

Sigma-Y over a typical rock element. The Sigma-Z is in the direction of overburden stress.

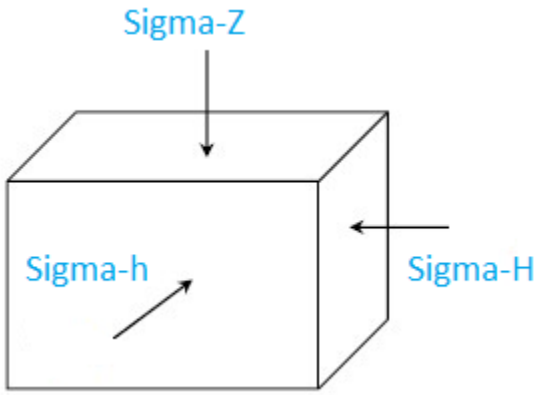

Fig. 4.12 Three principal stresses in a cubic element

In the cased-hole model, there is no fluid movement inside the formation. Therefore, the two formation horizontal stresses are given by the following equations in Eqs. 4.1 and 4.2. The equations show the unequal horizontal stresses resulting from geological tectonics. The typical facture direction inside formation is normal to the smallest principal stress. The two horizontal stresses are equal in the event of zero tectonic stress.

$$\sigma_H = \frac{\nu}{1-\nu}\sigma_z + \sigma_{tec} \tag{4.1}$$

$$\sigma_h = \sigma_H - \sigma_{tec} \tag{4.2}$$

Fig. 4.13 reveals that the maximum horizontal stress is in the direction of X axis and the minimum horizontal stress is in Y direction. This figure reveals a quarter section of the finite element mesh representing the cased-hole model. The quadrilateral element with four nodes is used.

We implement three cases, as shown in Table 4.4, to analyze the mechanical behavior of casing/cement in differing tectonic effect. Cement sheath is bonded with casing and formation. In the heating effect, the temperature of the wellbore fluid is 50 ˚F higher than that in the surrounding formation. The wellbore burst pressure of 10,000 psi is fixed while changing the contrast of two horizontal formation stresses. The formation tectonic effect rises from case 1 to case 3 when the ratio of maximum horizontal stress verse minimum horizontal stress is increased.

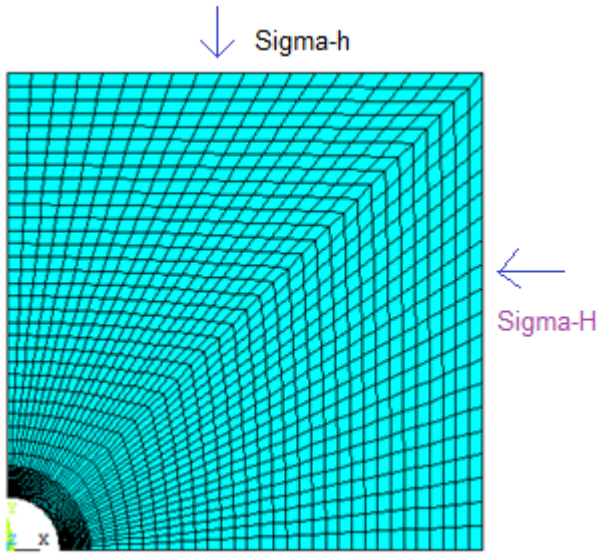

Fig. 4.13 The finite element model in differing horizontal stresses

Table 4.4 Formation tectonic analysis

	Fluid T, ˚F	Rock T, ˚F	Initial T, ˚F	Burst pressure, psi	Sigma-h, psi	Sigma-H, psi
Case 1	350	300	300	10,000	9,000	12,000
Case 2	350	300	300	10,000	8,000	12,000
Case 3	350	300	300	10,000	7,000	12,000

Case 1: Figs. 4.14 and 4.15 plot the radial stress and equivalent stress inside casing/cement under the formation effect of maximum horizontal stress of 12,000 psi

and minimum horizontal stress of 9000 psi. We predict the maximum compressive radial stress of 15,162 psi at the casing-cement interface, but it is normal to the formation minimum horizontal stress. The maximum equivalent stress occurs at the upper inner wall of the casing. The equivalent stress decreases from the maximum value of 36,429 psi at the upper inner wall of the casing to the minimum value of 6401 psi at the outer boundary of cement.

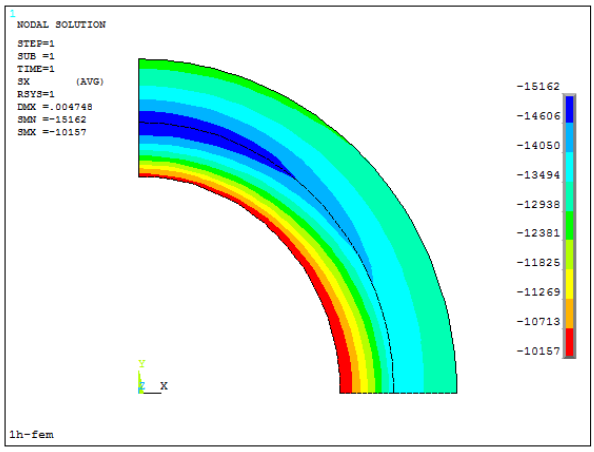

Fig. 4.14 Radial stress inside the casing/cement in case 1

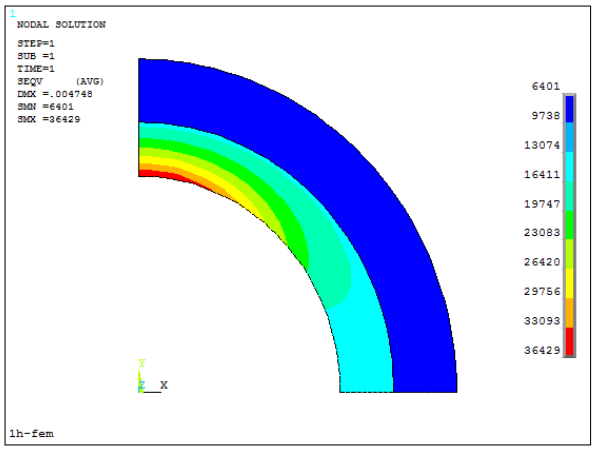

Fig. 4.15 Equivalent stress inside the casing/cement in case 1

Case 2: Compared with case 1, the formation minimum horizontal stress decreases by 1000 psi while maintaining other parameters. It results in that the tectonic effect in case 2 is stronger than that in case 1. The predicted results have shown, in Fig. 4.16, the maximum compressive radial stress of 14,958 psi at the upper casing-cement interface. Fig. 4.17 indicates that the maximum equivalent stress still occurs at the upper inner wall of the casing. This equivalent stress decreases from 38609 psi to the minimum value of 6033 psi at the outer boundary of the cement. However, the maximum equivalent stress inside casing/cement in case 2 increases by approximate 2180 psi compared with that in case 1.

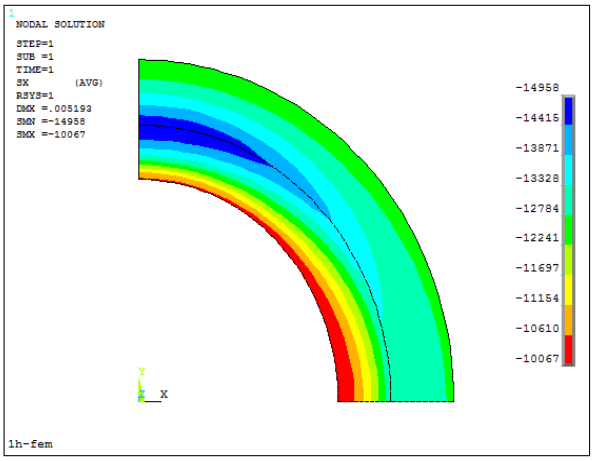

Fig. 4.16 Radial stress inside the casing/cement in case 2

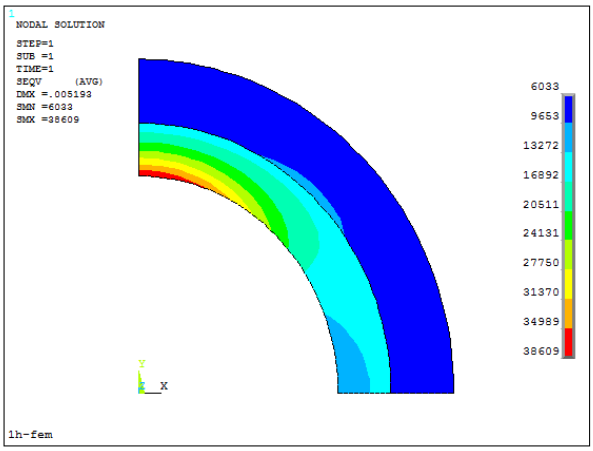

Fig. 4.17 Equivalent stress inside the casing/cement in case 2

Case 3: The formation minimum horizontal stress is assumed to be 7000 psi. The tectonic effect is strongest one since the large difference of formation minimum and maximum horizontal stresses. Fig. 4.18 reveals the maximum compressive radial stress of 14755 psi, which produces at the upper interface of casing and cement. This maximum radial stress is not significantly affected by the tectonic factor. The maximum equivalent stress inside casing/cement, as depicted in Fig. 4.19, is predicted 40803 psi. The equivalent stress in case 3 increases by approximate 2200 psi compared with that in case 2.

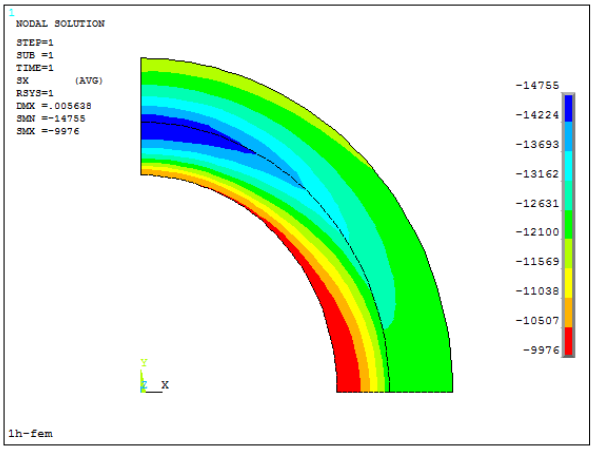

Fig. 4.18 Radial stress inside the casing/cement in case 3

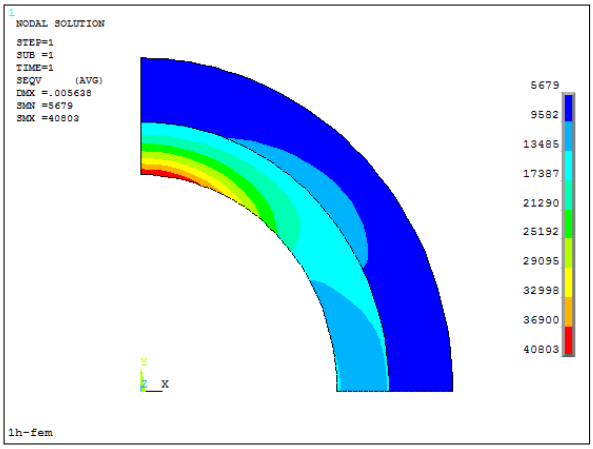

Fig. 4.19 Equivalent stress inside the casing/cement in case 3

Summarily, the comparison study is constructed to analyze the maximum radial stress and equivalent stress of the casing/cement in differing tectonic effect. Table 4.5 summarizes the maximum radial and equivalent stresses in the casing-cement system. Within a strong formation tectonic effect, we predict that the maximum radial stress inside casing/cement decreases and the maximum equivalent stress increases accordingly.

Table 4.5 Comparison analysis under different tectonic effect

	Max Radial stress, psi	Max Equivalent stress, psi
Case 1	15162	36429
Case 2	14958	38609
Case 3	14755	40803

4.4 Cooling effect

The temperature variation in the case-hole system depends on a group factors including fluid circulation rate, wellbore geometry and mud properties etc. The existing studies

revealed that the cool drilling fluid would help enhance the fracture gradient of formation, which could serve to increase the drilling window. I.Gil (2006) presented that, through creating a stress cage around the wellbore, the cooling effect was considered an alternative method to increase the formation fracture gradient in the low permeability zones. The thermal effect on bore hole instability is recently emphasized by different researchers([34];[32];[40];[42];[43];[44];[45];[46]).

The above researches focus on the interaction of drilling fluid and formation. However, the cooling effect in casing-cement system has not been well known. Drilling mud cools down the upper cased section in the wellbore during that traveling to the bottom hole.

The following discussion includes the mechanical behavior in the casing-cement-formation system caused by the well cooling effect. In the slight cooling case, the program simulates 50 ˚F differences in the cased hole using the wellbore fluid of 300 ˚F and initial formation temperature of 350 ˚F. Unlikely in the heating process, the stress evolution inside casing/cement during the cooling process is found to be more sensitive to the temperature variation. In the strong cooling effect, the stress profile of casing/cement is predicted using the formation temperature of 350 ˚F and wellbore fluid temperature of 100 ˚F. It is concluded that, in this case, the induced radial stress inside the casing/cement can change from compression to tension. Constant wellbore geometry and properties of the casing-cement-formation are maintained in the slight and strong cooling effects.

4.4.1 Behavior of Casing/cement by slight cooling effect

The cased-hole temperature depends on the parameters such as wellbore geometry, rock properties, fluid circulation rate, and fluid initial temperature. Figs. 4.20 to 4.22 have shown the temperature profile of the casing/ cement at different time steps. The cooling effect due to the movement of wellbore fluid results in that the temperature of casing/cement decreases from 350 ˚F to 300 ˚F. The casing temperature decreases

rapidly. The temperature of cement sheath decreases slowly because of the relatively large heat capacity.

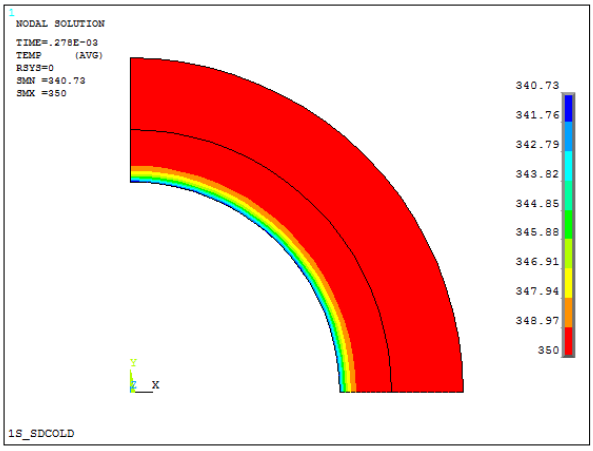

Fig. 4.20 Temperature of casing/cement at 1 second by the slight cooling effect

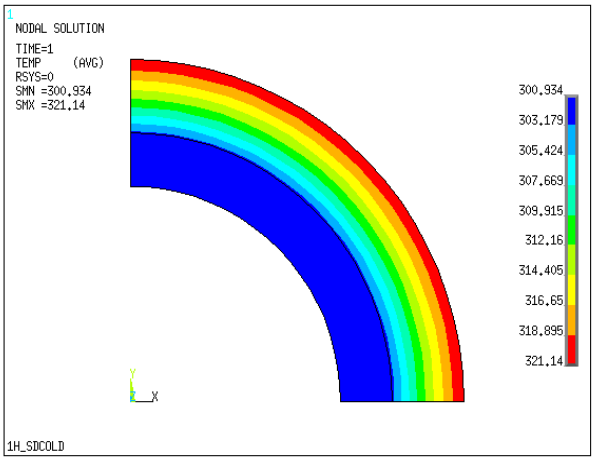

Fig. 4.21 Temperature of casing/cement at 1 hour by the slight cooling effect

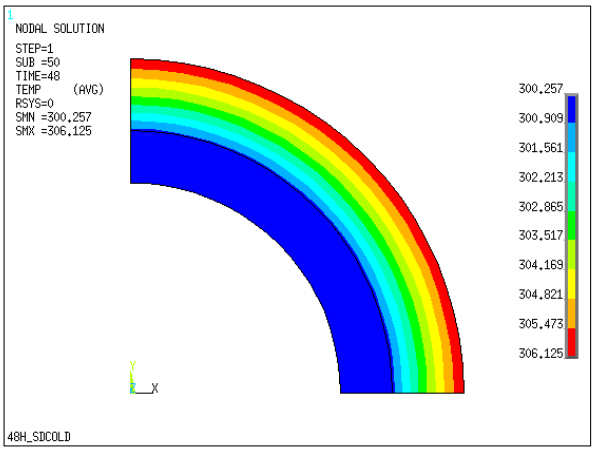

Fig. 4.22 Temperature of casing/cement at 48 hour by the slight cooling effect

It is indicated that the circulation of cool fluid may reduce the risk of casing-cement compressive radial cracking. On the plot of radial stress in Fig. 4.23, the compressive radial stress inside the casing increases in the radial direction, then reaches the largest value at the interface of casing and cement. However, along with the circulation of wellbore fluid, the maximum compressive radial stress decreases importantly. After 10 minutes, the maximum radial stress inside casing/cement is predicted at the inner wall of casing.

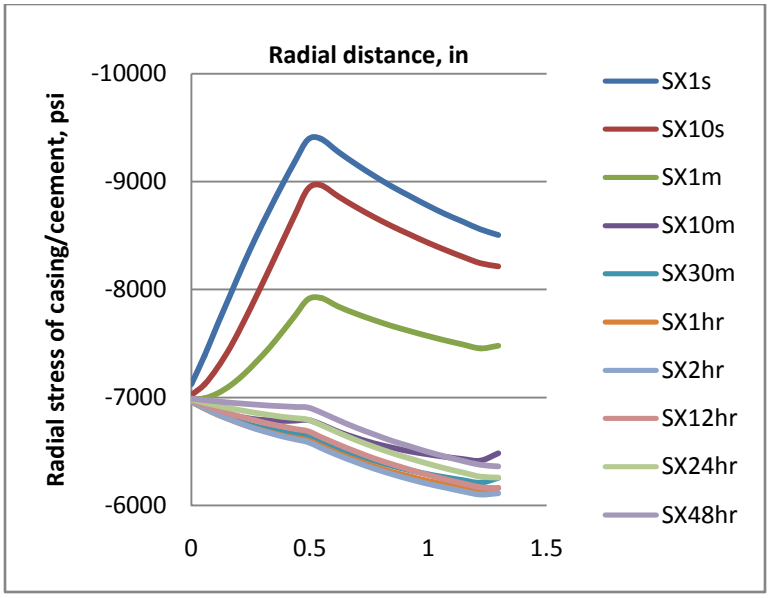

Fig. 4.23 Radial stress inside casing/cement by the slight cooling effect

The contour plots in Figs. 4.24 to 4.26 depict the evolution of radial stress in the casing-cement-formation system by the slight cooling effect. The maximum compressive radial stress at the casing-cement interface gradually decreases with time. It is clear to indicate that the maximum compressive radial stress occurs at the casing-cement interface. The compressive radial stress in the cased hole decreases and it becomes less important at the casing-cement interface after 1 hour.

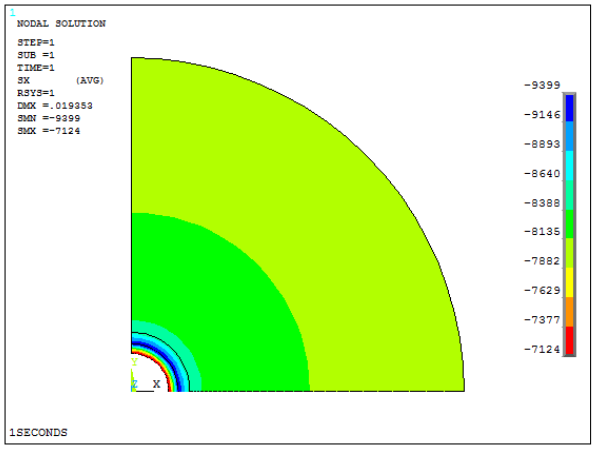

Fig. 4.24 Radial stress by the slight cooling effect at 1 second

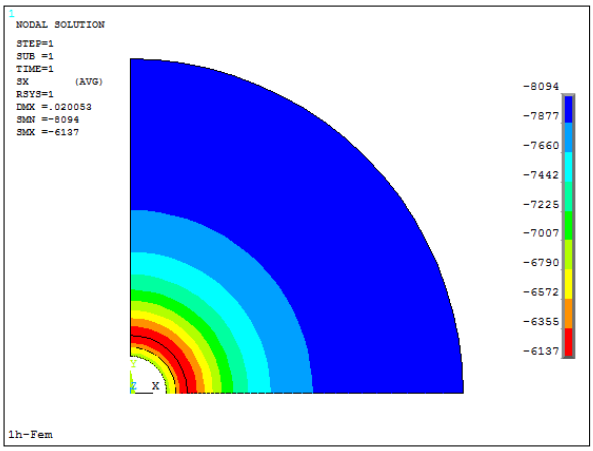

Fig. 4.25 Radial stress by the slight cooling effect at 1 hour

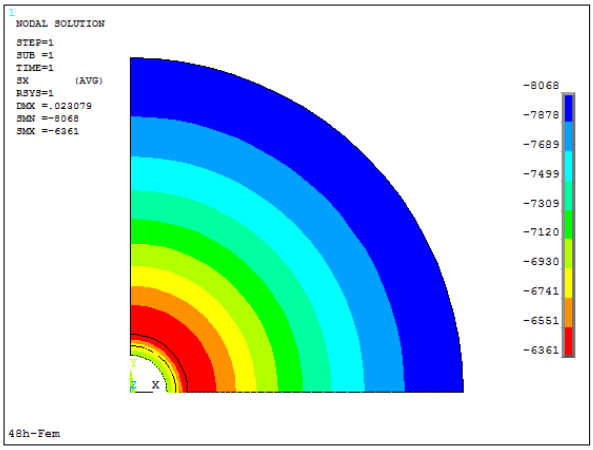

Fig. 4.26 Radial stress by the slight cooling effect at 48 hour

Casing/cement tangential cracking in the cased hole is caused by either tangential tension or tangential compression. Fig. 4.30 plots the tangential stress inside casing/cement caused by the slight cooling effect within 48 hours. Due to the movement of cool wellbore fluid, this process tends to reduce the induced compressive tangential stress in the cased hole. The tangential stress at the inner boundary of casing decreases from 15,057 psi to 6315 psi by the end of first hour. The compressive tangential stress inside the cement is not obviously affected by the slight cooling effect.

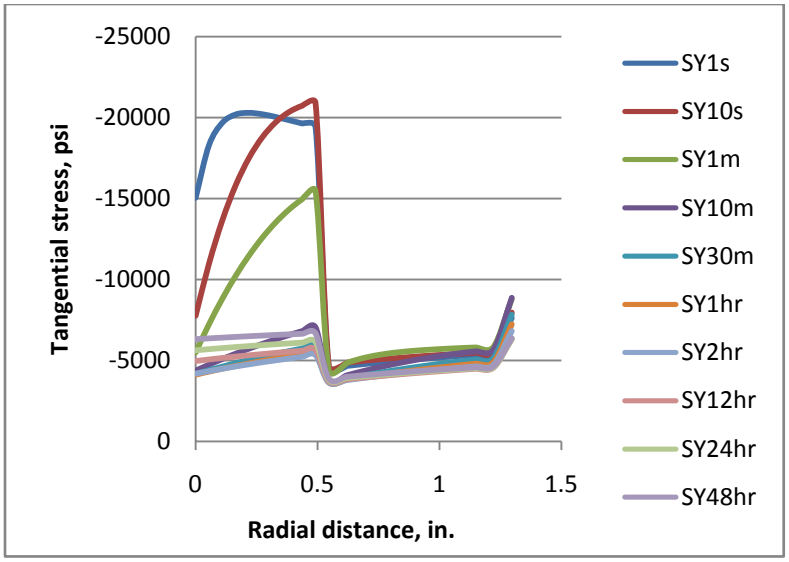

Fig. 4.27 Tangential stress inside casing/cement by the slight cooling effect

Fig. 4.31 has shown the variation of equivalent stress inside casing/cement caused by the slight cooling effect. This model predicted the maximum equivalent stress at the inner wall of the casing. Compared with the equivalent stress profile in the heating effect, it is concluded that both cooling and heating effects result in the increase of equivalent stress.

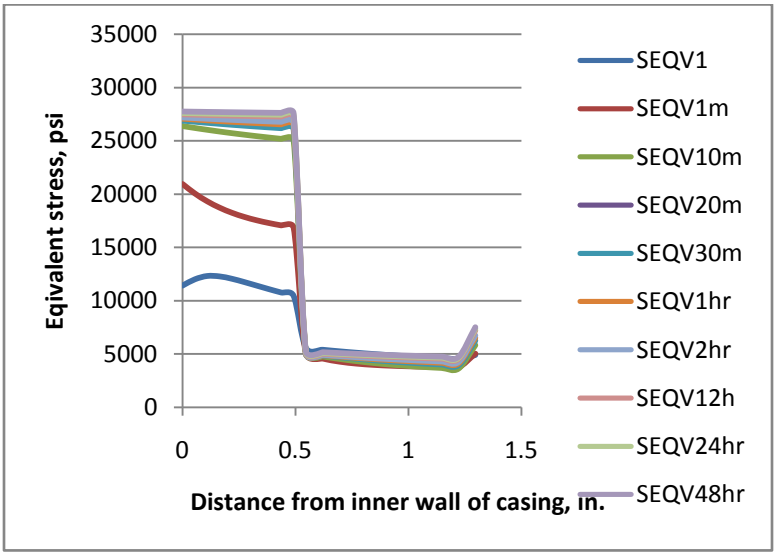

Fig. 4.28 Equivalent stress inside casing/cement by the slight cooling effect

4.4.2 Behavior of Casing/cement by strong cooling effect

In the strong cooling effect, the wellbore fluid is 250 ˚F lower than the formation. The compressive radial stress inside casing/cement still decreased with time in the strong cooling effect. Differently with the heating and slight cooling effects, the casing-cement system will experience a different mechanical behavior caused by the strong cooling effect when the fluid circulation time reaches a critical value.

Figs. 4.29 to 4.31 have shown the contour profile of radial stress in the first 10 minutes. The maximum radial stress doesn't occur at the interface of casing/cement. Instead of the compression in the slight cooling effect, the strong cooling effect due to the movement of wellbore fluid has resulted in the casing-cement tension. The tension stress inside casing/cement was increased by approximately 4111 psi by the end of ten minutes.

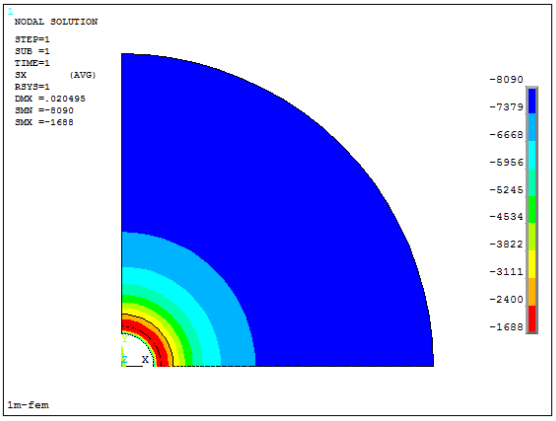

Fig. 4.29 Radial stress by the strong cooling effect at 1 minute

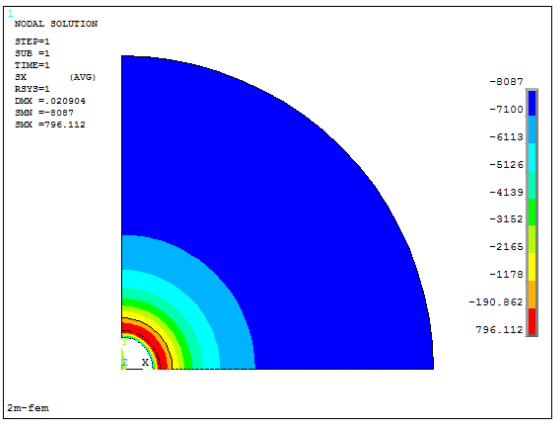

Fig. 4.30 Radial stress by the strong cooling effect at 2 minute

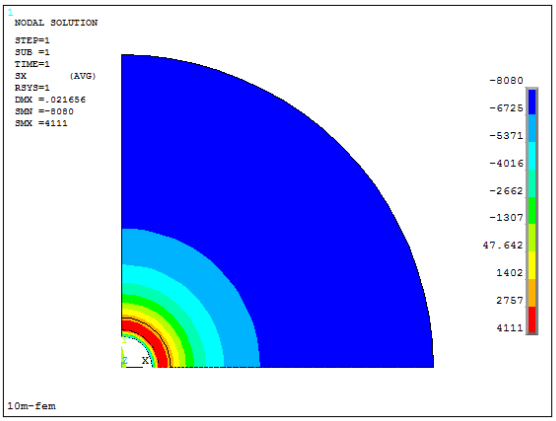

Fig. 4.31 Radial stress by the strong cooling effect at 10 minute

Fig. 4.32 has revealed that, at the beginning, the radial stress generated a maximum compressive value at the interface of casing and cement. In the slight cooling effect, the predicted radial stress inside the casing/cement shows the induced compression. When the wellbore fluid decreases to 100 ˚F, the casing/cement will suffer from the significant radial tension. By the end of 48 hour, the maximum radial tension produced at the interface of casing and cement.

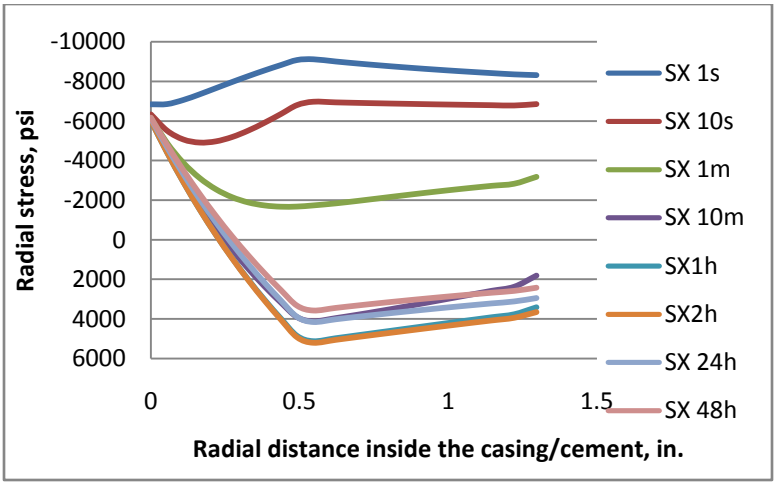

Fig. 4.32 Radial stress inside casing/cement by the strong cooling effect

Fig. 4.33 has revealed the tangential stress inside casing/cement within 48 hours when the wellbore fluid of 100 ˚F is circulated in the cased hole. Compared with the wellbore fluid of 300 ˚F, the larger temperature difference will also cause bigger tensile tangential stress inside the casing. The cement sheath was still under compression. The casing may no longer hold such tension and the tensile failure could happen in the cased hole.

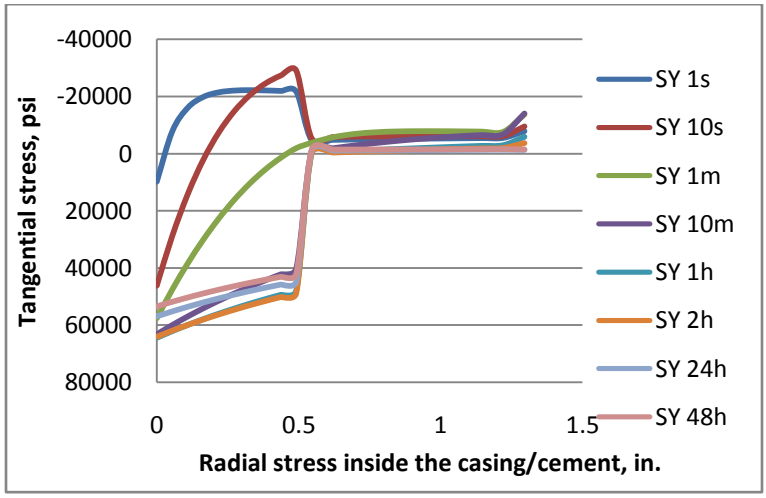

Fig. 4.33 Tangential stress inside casing/cement by the strong cooling effect

Fig. 4.34 has showed the equivalent stress inside casing/cement caused by the strong cooling effect in 48 hours. The larger equivalent stress was predicted at the inner wall of the casing. Compared with the equivalent stress in the slight cooling process, a cooler wellbore fluid can induce much larger equivalent stress in the casing-cement system. Obviously to know from Fig. 4.35, the down-hole thermal and hydraulic loads due to the fluid movement cause little influence in the casing-cement system in terms of the variation of equivalent stress.

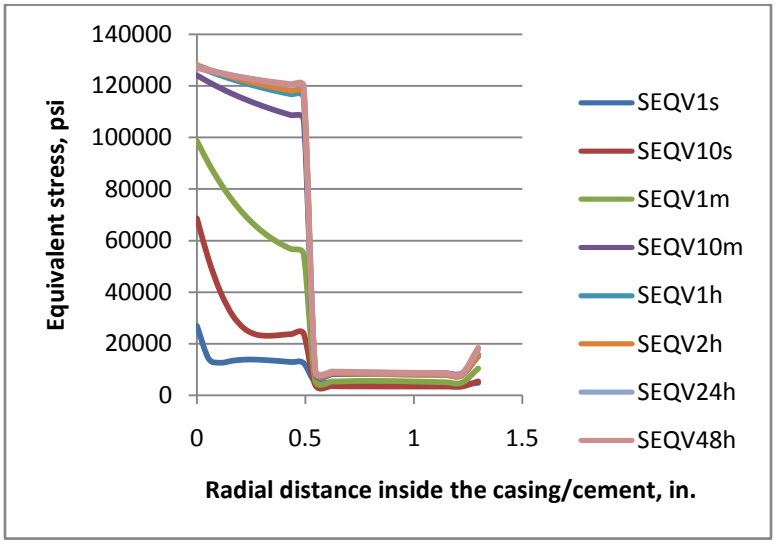

Fig. 4.34 Equivalent stress inside casing/cement by the strong cooling effect

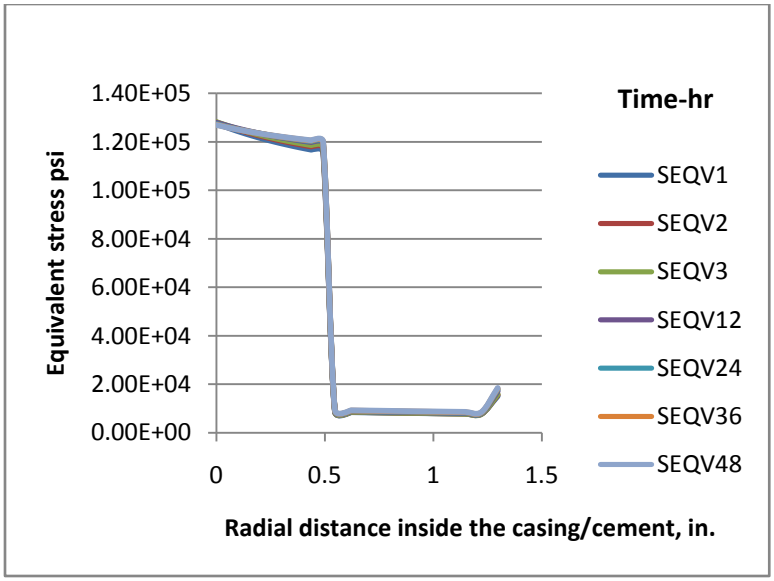

Fig. 4.35 Equivalent stress inside casing/cement by hours

4.4.3 Formation behavior by slight cooling effect

Formation will suffer from shear failure and compressive collapse once tensile or compressive stresses are greater than the formation strength. Temperature gradient between wellbore drilling fluid and formation in the open hole can cause the stress redistribution inside formation, which may result in the wellbore collapse or lost circulation. However, the induced stress inside formation in the cased hole has not yet been well understood. To construct the down-hole stress profile of formation, this section will discuss the mechanical response of formation in the cased hole during the circulation of wellbore fluid.

The predicted results show that the slight cooling effect can result in the reduction of formation compressive radial stress. We assume the fluid temperature of 300 ˚F in the wellbore. The casing inner diameter 0.408 in. and the casing-cement thickness is 1.296 in. The induced radial and tangential stresses inside formation are analyzed at different time steps. Fig. 4.36 has revealed the radial stress of formation in 48 hours. The inner surface of formation experienced the maximum compressive radial

stress, which is approximate 8500 psi. By the end of 48 hours, this compressive radial stress decreased to approximate 6100 psi.

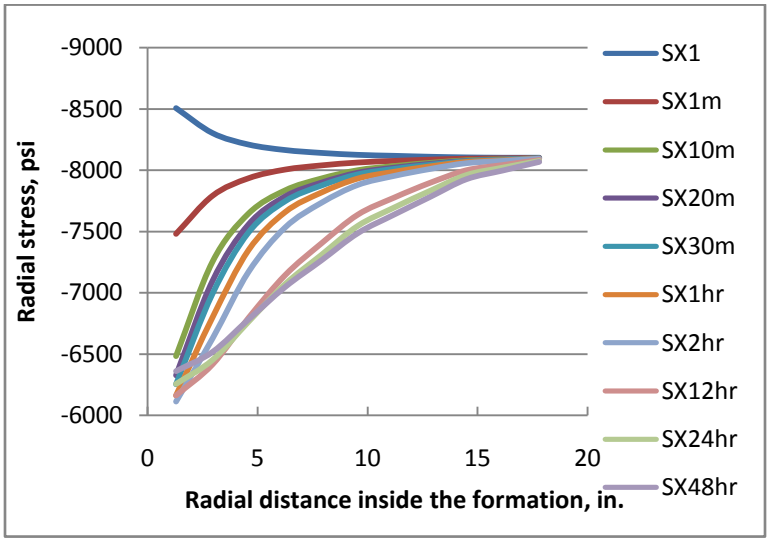

Fig. 4.36 Radial stress inside formation by the slight cooling effect in 48 hours

Fig. 4.37 has revealed that the mechanical behaviors of formation are divided two stages. The compressive tangential stress at the inner surface of formation nonlinearly increased in the first 10 minutes and the far field of formation has been little affected under the effect of wellbore fluid movement. In the second stage, the compressive tangential stress nonlinearly decreased at the inner surface of formation from 1 hour to 48 hours. The compressive tangential stress increased apparently at the far field of formation. Compared with the stress in the heating effect, the slight cooling effect created an opposite influence in terms of the mechanical response of formation.

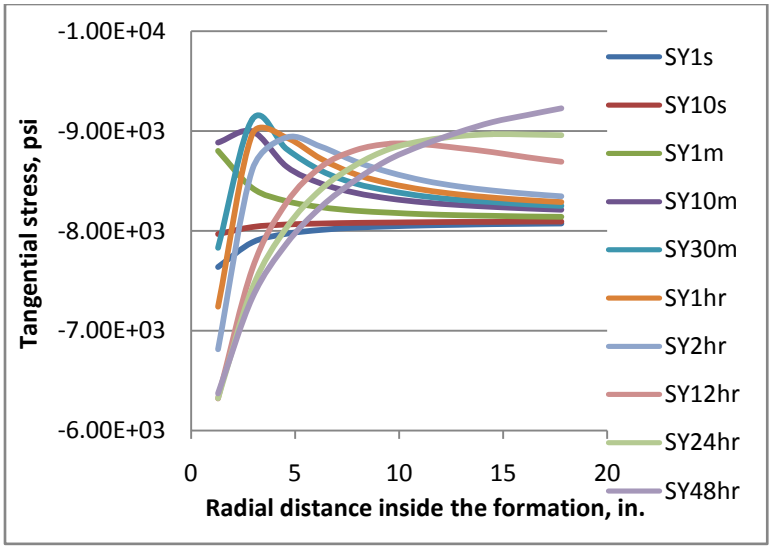

Fig. 4.37 Tangential stress inside formation by the slight cooling effect in 48 hours

Fig. 4.38 has revealed the variation of formation equivalent stress in 48 hours. In 1 minute, the movement of wellbore fluid didn't significantly change the equivalent stress distribution inside the formation. In 10 minutes, the equivalent stress at the cement-formation interface apparently increased and that at the far field of formation has not been largely changed. By the end of 48 hours, the maximum equivalent stress inside formation increased to 7505 psi from 4900 psi at the beginning.

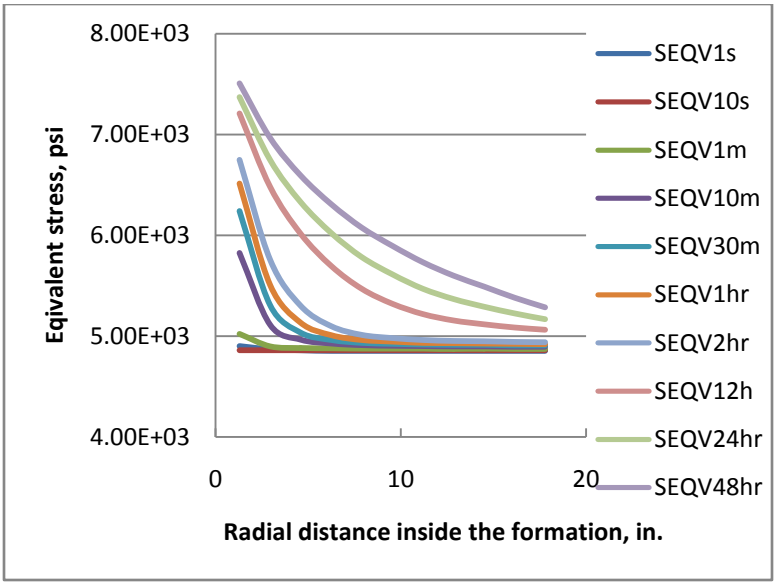

Fig. 4.38 Equivalent stress inside formation by the slight cooling effect in 48 hours

4.4.4 Formation behavior by strong cooling effect

Fig. 4.39 has revealed the radial stress inside formation in 48 hours. Instead of the compression inside the formation caused by the slight cooling effect, the radial stress at the inner surface of formation changed from compression to tension with time in the strong cooling effect.

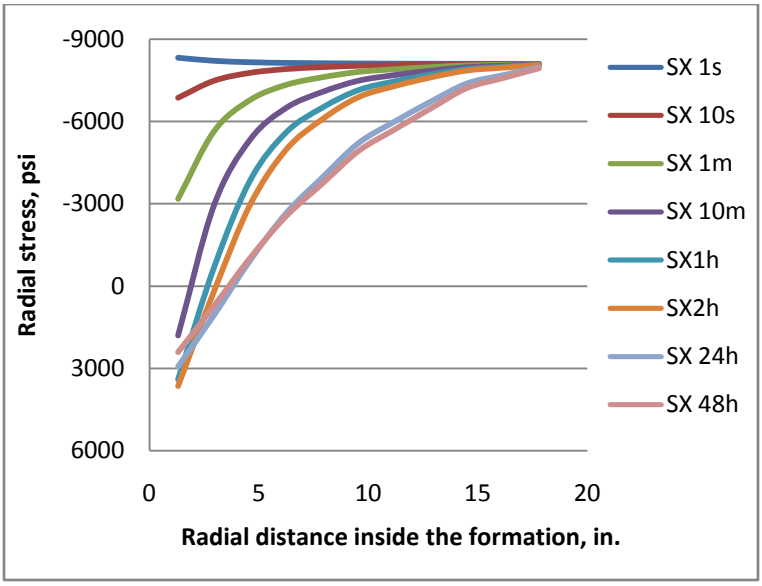

Fig. 4.39 Radial stress inside formation by the strong cooling effect in 48 hours

Fig. 4.40 has revealed that two stages of mechanical behaviors of formation caused by the strong cooling effect. In the first 10 minutes, the compressive tangential stress at the inner surface of formation increased. From 1 hour to 48 hours, the compressive tangential stress at the inner interface of formation slightly decreased.

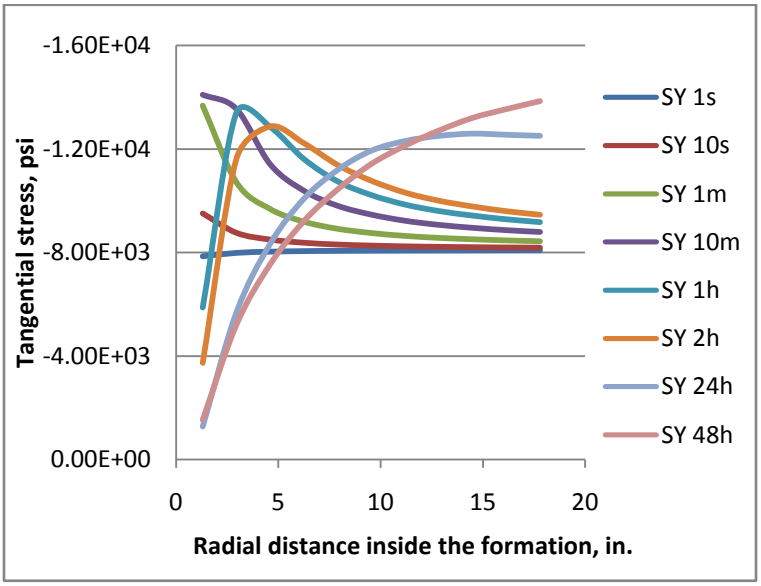

Fig. 4.40 Tangential stress inside formation by the strong cooling effect in 48 hours

Figs. 4.41 have shown that the equivalent stress inside formation uniformly increased in 48 hours in this case. At the interface of cement and formation, the equivalent stress is importantly increased under the strong cooling effect. After 1 hour, the equivalent stress inside the formation has little increased. By the end of 48 hours, it increased to 1, 8000 psi.

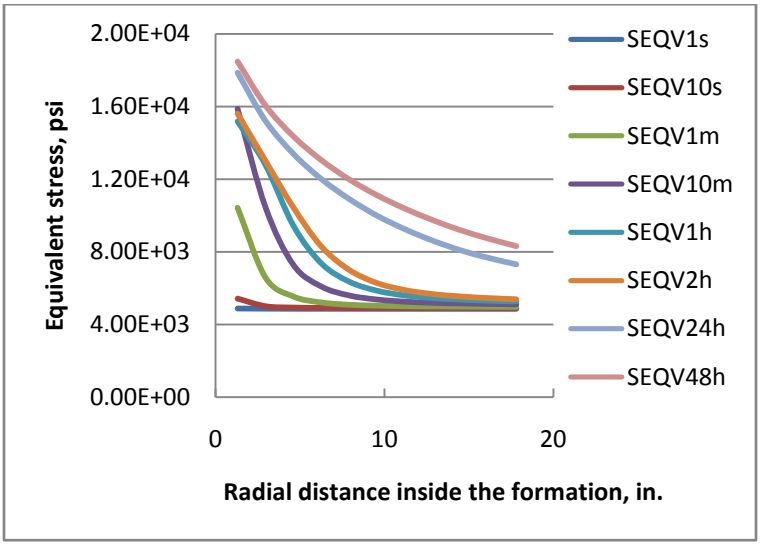

Fig. 4.41 Equivalent stress inside formation by the strong cooling effect in 48 hours

4.5 Discussion

This chapter investigates the induced stress in the casing-cement-formation system under HPHT conditions using finite element methods. The compressive radial stress inside casing/cement is concluded to reach a maximum value at the interface of casing and cement. This maximum stress at the casing-cement interface tends to decrease around 1 hour later. A group of parameters such as the properties of fluid and solid, as well as the wellbore geometry, will determine the critical time and stress.

The effect of formation tectonics has an apparent impact on the stress distribution inside casing/cement. The maximum compressive radial stress is predicted at the interface of casing and cement and it is normal to the formation minimum horizontal stress. The tectonic effect strongly influences equivalent stress inside casing/cement.

With the higher ratio of formation maximum horizontal stress against minimum horizontal stress, the larger equivalent stress is generated inside casing/cement.

The induced stress of casing/cement in the cooling effect behaviors differently with that in the heating effect. In the slight cooling effect, the radial stress inside casing/cement is predicted as compression. The maximum radial stresses will no longer generate at the casing/cement interface. Instead of the radial compression inside casing/cement caused by the slight cooling effect, the casing/cement will suffer from radial tension by the strong cooling effect.

5. NONHOMOGENEOUS EFFECT

5.1 Statement

Along with producing hydrocarbon resources in deep wells, maintaining the wellbore stability becomes a challenge task during drilling and completing through different formation zones. Well instability in shale formations has been recognized as a serious problem in many years. Shale is found in around 90% of drillable formations and over 70% of drilling instabilities are related to shale. Damages in the casing-cement system decreases the collapse and burst strength of casing/cement.

Shales are mainly composed of fine grain sands and clay. Shale presents the low strength resistance and most likely it is water sensitivity. The common problems of drilling in shale include borehole reduction or enlarging and wellbore collapse. Shale is also a naturally impermeable rock that prevents immigration of oil and gas. Generating oil and gas requires the hydrocarbon underneath and the rock cap to hold the resource. In reality, shale not only exclusively exists as a natural rock cap, it is also found inside the sandstone.

In order to understand the combination effect of shale and sandstone in the cased hole, we present a 3D finite element model. This part analyzes the casing-cement instabilities in the cased hole by the presence of nonhomogeneous formation. We investigate the interaction of casing, cement, and nonhomogeneous formation to evaluate the casing-cement instability.

It is found that the nonhomogeneous formation affects the distribution of radial stress in the casing and cement sheath. The risk of radial cracking and shear failure in the casing-cement-sandstone layer is higher than that in the casing-cement-shale layer.

5.2 Methodology

The expense of HPHT wells leads to using numerical modeling as an alternative way to evaluate well integrity in the absence of enough survey information, especially in a 3D

scale model. The 3D model is defined using an eight-node element with four variables at each node. The unknowns are the displacements in three directions and temperature on each corner point. This numerical model represents a quarter portion in a vertical well, as shown in Fig. 5.1. It has an outer diameter (OD) of 40 in., which is approximately 10 times the casing radii. The commonly accepted effective distance is as much as seven times the wellbore radius [3, 14].

A 3D model usually generates significant elements, which results in expensive computation cost. To decrease the element number, a vertical base model with height of 10 in. is adopted because the model with the bigger dimension is tested to demonstrate a similar behavior in heat transfer and mechanical response.

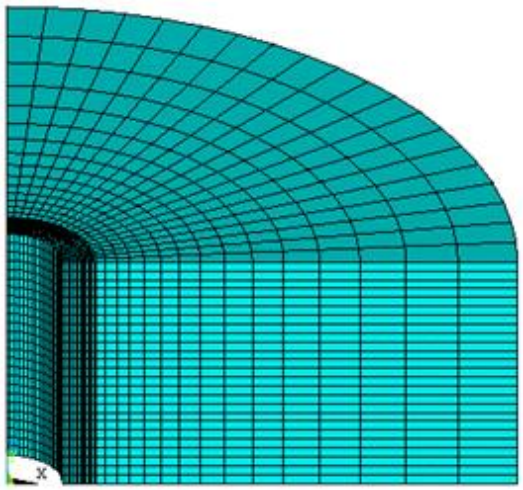

Fig. 5.1 The nonhomogeneous formation finite element model

A dense mesh is used in the vicinity of casing because stress concentration most likely occurs inside casing/cement sheath. To maximize accuracy of temperature and stress fields, a number of incremental elements were applied on the rock formation in the radial direction.

The force balance equation for the 3D model is given by Eq. 5.1 in the form of virtual strain energy. The first term represents virtual strain energy stored in this system,

the second term represents virtual energy induced by body forces, and the third term corresponds to the energy generation by boundary conditions.

$$\int_{\Omega_e} \sigma_{ij} \delta \varepsilon_{ij} d\Omega - \int_{\Omega_e} f_i \delta u_i d\Omega - \int_{\Gamma} t_i \delta u_i ds = 0 \tag{5.1}$$

Because the thermal stress $\sigma_T = \Delta T \alpha E$ is imposed, the stress tensor in Eq. 5.2 can be expressed in the form of Eq 5.1 [47]

$$\sigma_{ij} = 2G\varepsilon_{ij} + \frac{vE}{(1+v)(1-2v)} \varepsilon_{vol} \delta_{ij} + \frac{E}{1-2v} \alpha_T \delta_{ij} T \tag{5.2}$$

5.3 Case study

This model investigates the effects of nonhomogeneous formation, temperature variation, and induced radial stress on casing-cement sheath. Table 5.1 shows the designed properties and geometry of casing/cement/ formation. The other material properties are found in Table 4.1.

Table5. 1 The geometry of nonhomogeneous model

Well depth, ft	18,000
Circulation rate, gpm	250
Fluid weight, ppg	11
Fluid viscosity, cp	2
Fluid specific heat, btu/lb. ˚F	0.45
Fluid thermal conductivity, btu/ft.hr. ˚F	1.0
Horizontal in-situ stress, psi	12,000
Overburden stress, psi	14,000
Casing inside diameter (ID), in.	4.408
Casing OD, in.	5.5
Cement sheath ID, in.	5.5
Cement sheath OD, in.	7
Formation ID, in.	7
Formation OD, in.	40
Model height, in.	10
Fluid circulation time, hour	12
Gravitational factor,m^2/s	9.8

The fluid in the wellbore has an initial temperature of 300 ˚F, the original formation temperature is 350 ˚F. Figs. 5.2 and 5.3 revealed temperature profile with respect to time in 12 hours. In all time steps, temperature decreased from its highest value of 350 ˚F at the outer boundary of formation to its lowest value of 300 ˚F at the wellbore. Applying a cooling effect by lowering circulation fluid leads to temperature decline at any observed location. It is interesting to indicate that the formation temperature could not be impacted heavily by this effect. Besides the fluid temperature

and its thermal properties, a supplemental cause to this behavior is that heat transfer in the formation depends on the combination of wellbore geometry, rock properties, and the fluid circulation rate.

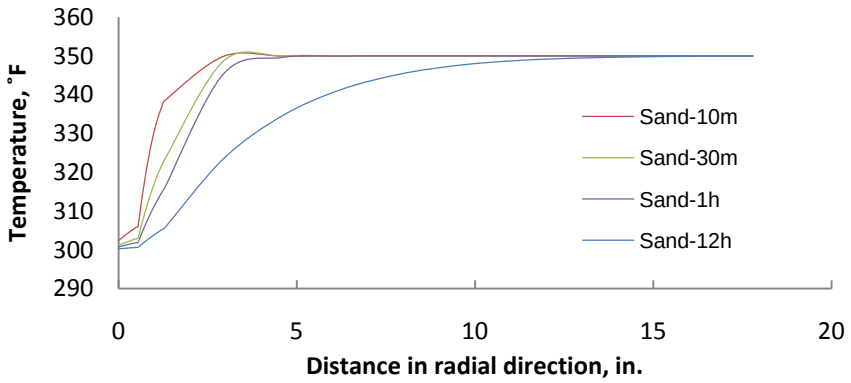

Fig. 5.2 Temperature profile in the casing-cement-sandstone.

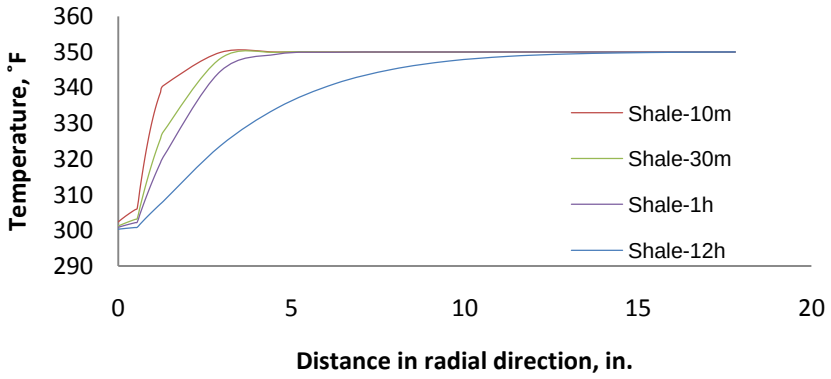

Fig. 5.3 Temperature profile in the casing-cement-shale.

To understand the mechanism of the system's heat transfer and its energy exchange, thermal gradient (TG) is used to characterize the behavior of heat transfer across casing and cement sheath during wellbore fluids circulation. This leads us to an in-depth evaluation of which path and at what rate temperature changes most quickly in the cased hole.

Figs. 5.4 to 5.6 describe thermal gradient under the cooling effect process of the system. The higher thermal gradient (red color) indicates that the temperature changes most rapidly around those areas. This value changes with respect to time, and the heat gradient also shifts in the radial direction of casing and cement sheath. The higher TG occurs around its interface of casing and cement, but its distribution is different at 30 minutes, shown by the presence of two coning shapes.

The profiles in Figs.4c and 4d show the calculated TGs in casing, cement, and formation at 1 hour and 12 hours. A large heat capacity in both shale and sandstone leads to a slow process of cooling the formation. The highest TG in the red areas shifts into the formation, and its value also indicates that, at these time steps, heat transfer in shale layers is relatively quicker than those in sandstone layers. Compared with sandstone, shale with lower thermal conductivity delays the heat energy of the formation across the interface between the cement sheath and the formation.

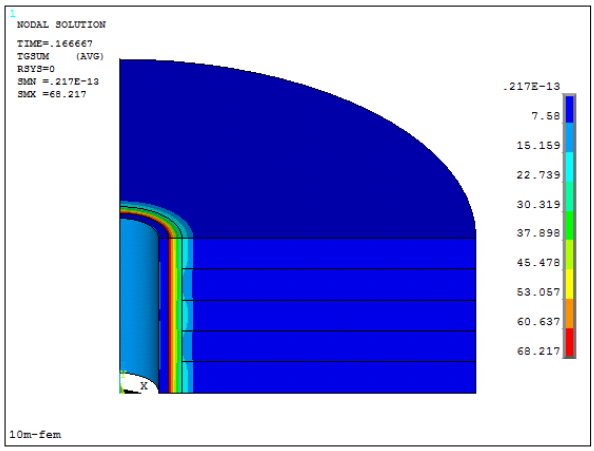

Fig. 5.4 Thermal gradient in the nonhomogeneous formation at 10 minutes

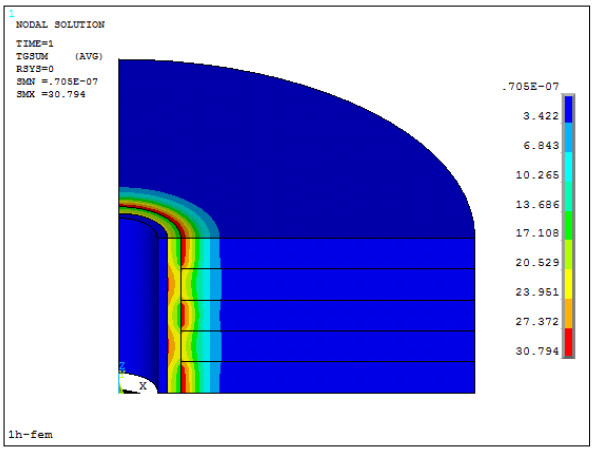

Fig. 5.5 Thermal gradient in the nonhomogeneous formation at 1 hour

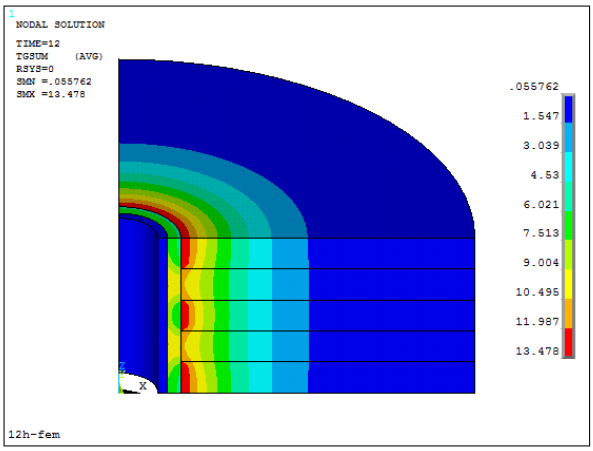

Fig. 5.6 Thermal gradient in the nonhomogeneous formation at 12 hours.

Results shown in Figs.4a to 4d also indicate that rock formation has an impact on the thermal profile of the casing-cement sheath. Cement slurry with the same properties is filled in the entire annulus between casing and formation, and the properties of fluid in the wellbore stays constant. However, the TG distribution inside the cement sheath is not uniform because the rate of heat transfer in shale and sandstone is different.

5.3.1 Induced shear stress and thermal stress in this model

Figs. 5.7 and 5.8 show the behavior of radial stress in the casing and cement sheath as function of time. The results, both at the beginning and at 12 hours, show that higher radial stress occurs in the interface between casing and cement sheath, regardless of its surrounding rock type. This is because wellbore contraction under horizontal in-situ stresses inward tends to reduce its diameter, whereas the hydraulic pressure in the wellbore tends to expand wellbore diameter. A much more important implication of this study shows that the induced shear stress by the unequal radial stress in the vertical direction could contribute to damage on casing and cement.

Furthermore, radial stress predicted around the interface between casing and cement-sandstone has a larger value, whereas the area between casing and cement-shale has a relatively lower radial stress. Shale with a high percent of clay has ductile mobility under high compression pressure, which results in zones of sandstone experiencing higher stress because of less mobility compared with zones of shale. Because cement fully bonds to the casing and rock formation, the synchronized movement inside the casing-cement-rock formation will lead to higher stress and a larger area inside casing-cement.

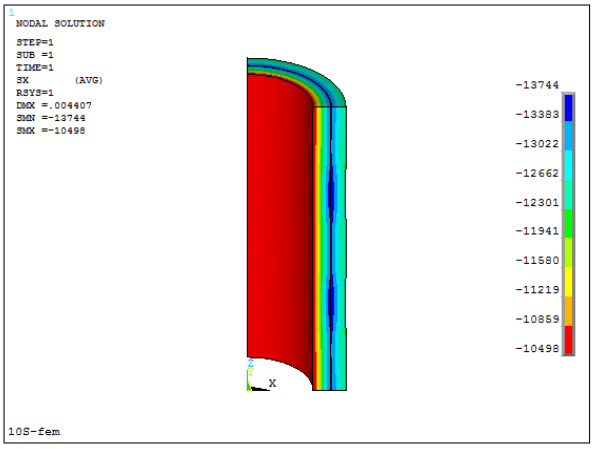

Fig. 5.7 Radial stress of casing/cement in the nonhomogeneous formation at 10 s

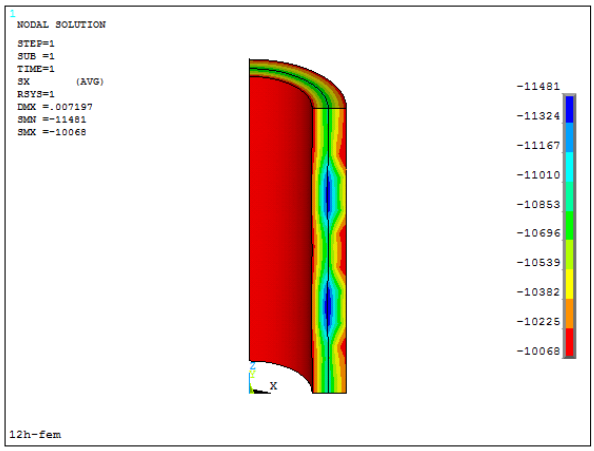

Fig. 5.8 Radial stress of casing/cement in the nonhomogeneous formation at 12 h

As seen in the casing-cement system over 12 hours, the maximum radial stress decreases in the interface of casing-cement as a function of time. The explanation behind this behavior is that thermal stress resulting from the temperature difference between wellbore and formation has an opposite direction compared with the direction of compression radial stress in the interface. It leads to the net radial stress decreasing as thermal stress increases. Thus, the thermal stress should not be overemphasized in the cooling effect. Results indicate that thermal stress in the base study decreases by approximately 2,300 psi.

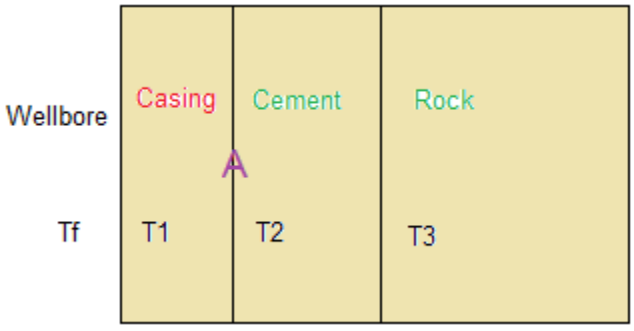

Fig. 5.9 Cross section of this model in the nonhomogeneous formation.

The maximum radial stress is predicted at Interface A, as indicated in Fig 5.9, but it decreases as thermal stress increases. The relation can be found in Eq. 5.3. Thermal stress in the area of A points to the wellbore because T2 is always bigger than T1, whereas the radial stress is in the opposite direction.

$$\sigma_{\text{interface}} = \sigma_A - \sigma_{thermal} \tag{5.3}$$

5.3.2 Gravity effect

Formation in this model not only carries the weight of the formation above, but is also subject to its body force. To this point, the equivalent stress in the top and bottom layers draws us to investigate gravity effect on this model. The predicted results, as shown in Fig. 5.10, indicate that the equivalent stress at the top is hardly different from the bottom. Apparently, the gravity effect on this model is negligible.

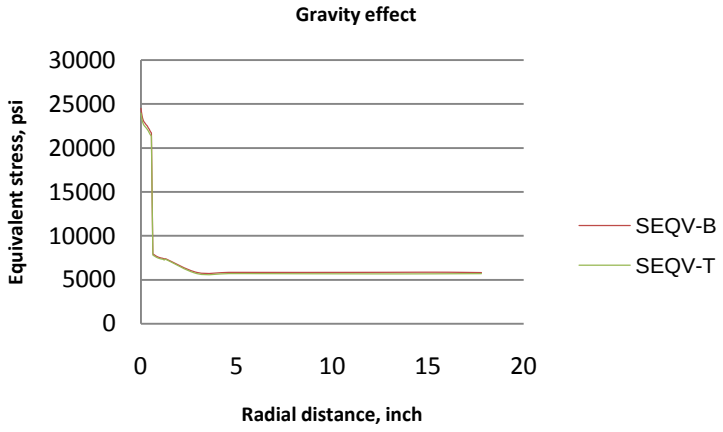

Fig. 5.10 Equivalent stress profile at the top and bottom layers of this model.

5.3.3 Effect of shale ductile behavior

To examine the ductile behavior of shale induced by its lower stiffness, a comparison study of shale stiffness and sandstone stiffness was run. The Young's modulus of

sandstone was fixed, and the Young's modulus of shale was slightly decreased from its original 4 × 106 psi to 3×106 psi and 2×106 psi, separately. This model was still run with a 14,000-psi overburden stress in the wellbore and kept the remaining initial and boundary conditions unchanged. The maximum radial stress calculated by a 4×106-psi Young's modulus of shale is 13,744 psi. Figs. 5.11 and 5.12 indicate that within the shale's Young's modulus of 3×106 psi and 2×106 psi, the maximum radial stress in the interface of casing and cement is predicted at 14,391 psi and 16,354 psi. This leads to the conclusion that softer shale will significantly increase the maximum radial stress in the casing-cement-sandstone layer, subsequently increasing the risk of radial cracking and shear failure around the casing-cement interface.

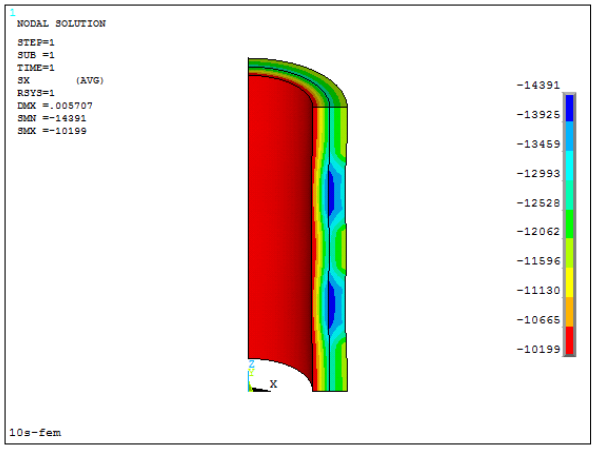

Fig. 5.11 Radial stress inside casing/cement by shale Young's modulus of 3×10^6 psi.

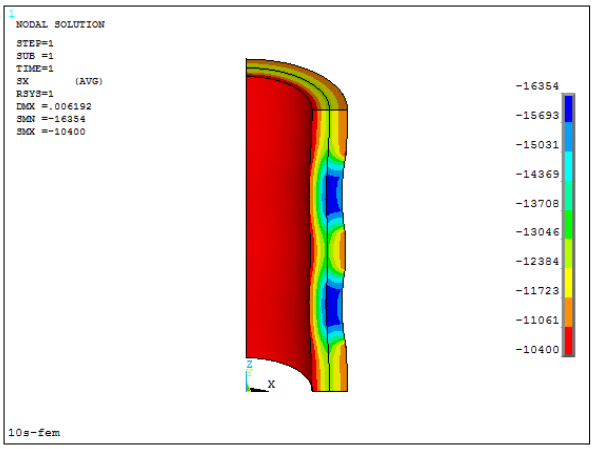

Fig. 5.12 Radial stress inside casing-cement by shale Young's modulus of 2×10^6 psi.

5.4 Discussion

The radial stresses of casing/cement sheath decrease significantly in both sandstone and shale layers as function of circulation time. The nonhomogeneous formation affects the distribution of radial stress in the casing and cement sheath. The risk of radial cracking and shear failure in the interface between casing and cement/sandstone is higher than in the casing-cement-sandstone layer.

Within a lower Young's modulus for shale, the higher radial stress was predicted in the casing-cement-sandstone layer. Body force induced by the gravity in the cased-hole model is concluded to be neglected through comparing the equivalent stress in the top layer and in the bottom layer.

6. CASING WEAR

6.1 Statement

This part aims to establish the proper understanding of the mechanical responses for worn casing in HPHT wells. Casing wear is considered a serious problem in HPHT wells, particularly in directional and extended drilling. Because the rotation of drill pipe causes significant contact forces, casing wear creates the reduction of casing wall. Subsequently, the effect of casing wall reduction will induce stress concentration at the worn area and then result in new burst and collapse resistance of the remaining casing. In the presence of corrosive fluids in the well, the reduction of casing thickness will be accelerated because of the chemical reaction also destroying the surface of casing.

The contact pressure on the inner surface of casing becomes much harder to control during drilling through deep formations. Casing wear is not only a problem related to directional or extended wells; it also occurs in vertical wells.

Casing wear causes significant casing strength reduction, thereby possibly resulting in a tangential collapse and radial crack in the wellbore system. Without considering the effect of down-hole heat transfer, the casing wear model will be insufficient for evaluating the true stress of worn casing in the development of deep wells. In terms of an analytical solution, the typical Lame equation does not consider the temperature effect. First, we propose a casing model without wear by considering the thermal stress. Then, we use the boundary superposition for analyzing the casing wear model.

In this chapter, we describe the stress concentration of casing after wear in a cemented well. Since the traditional Lame equations for cylinder are weakened by the lack of the temperature effect, and our direct solution considers that the effects of temperature variation on the worn casing are solved under the assumption of boundary superposition.

The results have shown that the elevated temperature intended to expand the worn part of casing and significantly resulted in further compression hoop stress. The

casing uncemented with formation will suffer from tension when the burst pressure is applied in the wellbore.

6.2 Analytical model

The force equilibrium of a wellbore consists of normal forces, shear forces, and body forces. In the cylindrical coordinate system, these are expressed as follows (Fjaer et al. 2008).

$$\frac{\partial \sigma_r}{\partial r} + \frac{1}{r}\frac{\partial \tau_{r\theta}}{\partial_\theta} + \frac{\sigma_r - \sigma_\theta}{r} + \sigma f_r = 0 \tag{6.1}$$

After neglecting the effect of shear force and body force, Eq. 6.2 is obtained from Eq. 6.1

$$\frac{\partial \sigma_r}{\partial r} + \frac{\sigma_r - \sigma_\theta}{r} = 0 \tag{6.2}$$

Eqs. 6.3 to 6.5 present the stress-strain relations for homogeneous, isotropic materials.

$$\varepsilon_r - \alpha_T \Delta T = \frac{1}{E}\left[\sigma_r - \nu(\sigma_z + \sigma_\theta)\right] \tag{6.3}$$

$$\varepsilon_\theta - \alpha_T \Delta T = \frac{1}{E}\left[\sigma_\theta - \nu(\sigma_z + \sigma_r)\right] \tag{6.4}$$

$$\varepsilon_z - \alpha_T \Delta T = \frac{1}{E}\left[\sigma_z - \nu(\sigma_\theta + \sigma_r)\right] \tag{6.5}$$

Plain strain is applied in the cased hole because the dimension of the well in the axial direction is very large compared with the dimensions of the well in the other two directions. Therefore, the strain of a normal x-y plain and the shear strains γ_{xz} and γ_{yz} are assumed to be zero. The relations are expressed in Eq. 6.6.

$$\varepsilon_z = \gamma_{xz} = \gamma_{yz} = 0 \tag{6.6}$$

To express the axial stress using radial stress and hoop stress, Eq. 6.7 is obtained after substituting Eq. 6.6 into Eq. 6.5.

$$\sigma_z - \alpha E \Delta T = \nu\left[\sigma_r + \sigma_\theta\right] \tag{6.7}$$

Thus, the relation of strain-stress in Eqs. 6.3 and 6.4 can be rearranged as shown in Eqs. 6.8 and 6.9.

$$\varepsilon_r = \frac{1}{E}\left[\sigma_r\left(1-\nu^2\right) - \nu(1+\nu)\sigma_\theta + (1+\nu)\alpha E \Delta T\right] \tag{6.8}$$

$$\varepsilon_\theta = \frac{1}{E}\left[\sigma_\theta\left(1-\nu^2\right) - \nu(1+\nu)\sigma_r + (1+\nu)\alpha E \Delta T\right] \tag{6.9}$$

Solving Eqs. 6.8 and 6.9 for σ_r, σ_θ yields the following.

$$\sigma_r = \frac{E(1-\nu)\varepsilon_r + E\nu\varepsilon_\theta - (1+\nu)\alpha E \Delta T}{(1+\nu)(1-2\nu)} \tag{6.10}$$

$$\sigma_\theta = \frac{E(1-\nu)\varepsilon_\theta + E\nu\varepsilon_r - (1+\nu)\alpha E \Delta T}{(1+\nu)(1-2\nu)} \tag{6.11}$$

The relations between displacements and strains are expressed in Eqs. 6.12 and 6.13.

$$\varepsilon_r = \frac{\partial u}{\partial r} \tag{6.12}$$

$$\varepsilon_\theta = \frac{u}{r} \tag{6.13}$$

For simplicity, the minimum horizontal stress is equal to maximum stress, and both temperature and pressure are applied in the system. The boundary conditions in the wellbore are presented in Eqs. 6.14 to 6.17.

$$r = r_w, \sigma = p_w \tag{6.14}$$

$$r = r_o, \sigma = p_o \tag{6.15}$$

$$r = r_w, T = T_w \tag{6.16}$$

$$r = r_o, T = T_o \tag{6.17}$$

To solve for the stress in the cylinder system, the relations of stress-strain and strain-displacement, as well as the boundary conditions, are applied into Eq. 6.2. This application results in the general expressions of stresses as presented in Eqs. 6.18 to 6.20.

$$\begin{aligned}\sigma_r = & \frac{2(p_o r_o^{\,2} - p_w r_w^{\,2})(1-\nu) + \alpha E \Delta T (r_o^{\,2} - r_w^{\,2})}{2(r_o^{\,2} - r_w^{\,2})(1-\nu)(1-2\nu)} \\ & - \frac{2(p_o - p_w)(1-\nu) r_o^{\,2} r_w^{\,2} + \alpha E \Delta T r_w^{\,2} (r_o^{\,2} - r_w^{\,2})}{2(1-\nu)(r_o^{\,2} - r_w^{\,2}) r^2} - \frac{\alpha E \Delta T}{2(1-\nu)} \left(1 - \frac{r_w^{\,2}}{r^2}\right)\end{aligned} \tag{6.18}$$

$$\begin{aligned}\sigma_\theta = & \frac{2(p_o r_o^{\,2} - p_w r_w^{\,2})(1-\nu) + \alpha E \Delta T (r_o^{\,2} - r_w^{\,2})}{2(r_o^{\,2} - r_w^{\,2})(1-\nu)(1-2\nu)} \\ & + \frac{2(p_o - p_w)(1-\nu) r_o^{\,2} r_w^{\,2} + \alpha E \Delta T r_w^{\,2} (r_o^{\,2} - r_w^{\,2})}{2(1-\nu)(r_o^{\,2} - r_w^{\,2}) r^2} - \frac{\alpha E \Delta T}{2(1-\nu)} \left(1 + \frac{r_w^{\,2}}{r^2}\right)\end{aligned} \tag{6.19}$$

$$\sigma_z = \frac{4v(p_o r_o^{\,2} - p_w r_w^{\,2})(1-v) + \alpha E \Delta T (r_o^{\,2} - r_w^{\,2})}{2(r_o^{\,2} - r_w^{\,2})(1-v)(1-2v)} - \frac{\alpha E \Delta T (1-2v)}{(1-v)} \tag{6.20}$$

6.3 Casing wear and boundary superposition

Because the concept of stress profile for a crescent-shaped body is limited, it would be difficult to determine the stress profile around the worn portion using a direct principle. The superposition theory is widely acceptable in the analysis of stress concentration resulting from small particles in contact zones. Boundary conditions are discretized into several virtual parts (Mudumba 2005). Instead of solving for this problem directly, the hoop stress at the worn area will be analyzed in two virtual parts.

In these virtual regions, the burst pressure acting in the worn part is considered as the superposition of two parts, as shown in Figs. 6.1 to 6.3. The thickness variation after wear is defined using Eqs. 6.21 and 6.22. The r_{new} is defined as the wellbore radius after casing wear. The r_{new} is bigger than r_w because of the reduction of casing wall.

$$h_1 = r_o - r_w \tag{6.21}$$

$$h_2 = r_o - r_{new} \tag{6.22}$$

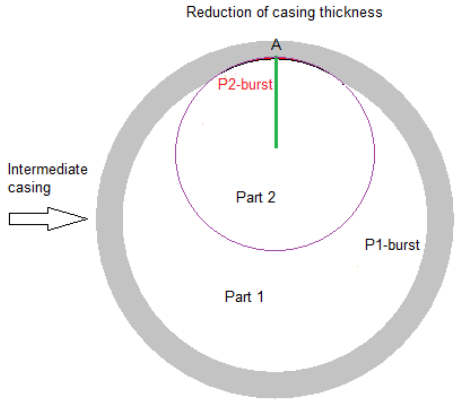

Fig. 6.1 Casing wear scheme by tool joint.

Fig 6.1 presents that the intermediate casing is worn by a tooljoint with a radius of r_2, and the worn area is indicated by a red line around Point A. The hoop stress concentration is induced by the geometry change resulting from casing wall reduction. P1 and P2 represent the burst pressure in the worn surfaces and the integrity surfaces separately. Because the burst pressure is always perpendicular to the tangential line of its arc, they apparently have an identical value within a different radial direction.

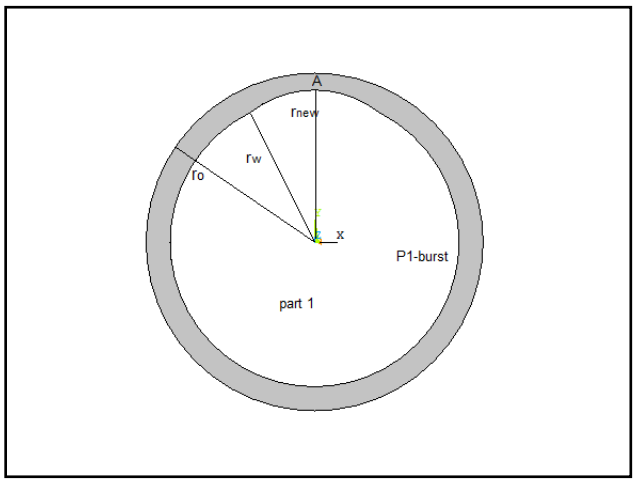

Fig. 6.2 Induced hoop stress in virtual part 1.

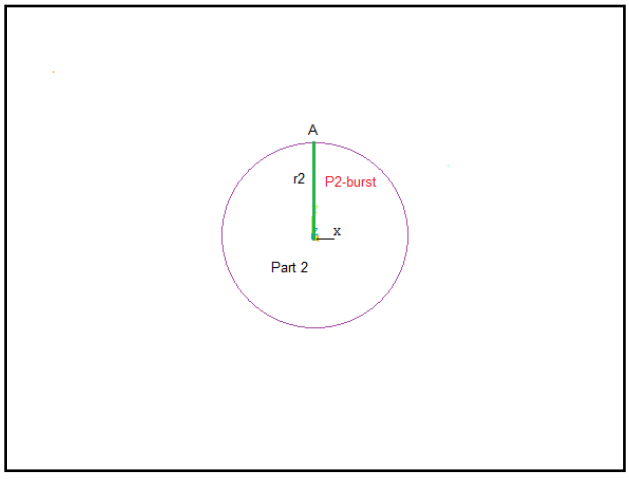

Fig. 6.3 Induced hoop stress in virtual part 2.

Before casing wear: Point A is in the first virtual structure of Part 1,which is located inside the casing wall. Therefore, the hoop stress of $\sigma_{\theta 1}$ at Point A with respect to $r \in (r_w, r_o)$ can be calculated using Eq. 6. 19.

After casing wear: The wall behind Point A, as shown in Fig. 6.2, is the thinnest part in the entire casing. The radius of r_{new} at Point A implies that the thickness of casing decreased from h1 to h2. Point A in the second virtual structure of Part 2 is on the boundary of the new arc. The effect of the crescent-worn shape will generate an additional stress of $\overline{\sigma}_\theta$ using Eq. 6.23.

$$\overline{\sigma}_\theta = \frac{2(p_o(r_2+h_2)^2 - p_w r_2^{\,2})(1-v) + \alpha E \Delta T((r_2+h_2)^2 - r_2^{\,2})}{2((r_2+h_2)^2 - r_2^{\,2})(1-v)(1-2v)} - \frac{\alpha E \Delta T}{2(1-v)}(1+\frac{r_w^{\,2}}{r^2}) + \frac{2(p_o - p_w)(1-v)(r_2+h_2)^2 r_2^{\,2} + \alpha E \Delta T r_2^{\,2}((r_2+h_2)^2 - r_2^{\,2})}{2(1-v)((r_2+h_2)^2 - r_2^{\,2})r^2} \tag{6.23}$$

Thus, the hoop stress in the wear part can be obtained from Eq. 6.24.

$$\sigma_{\theta,wear} = \sigma_{\theta 1} + \overline{\sigma}_\theta \tag{6.24}$$

6.4 Numerical solution

Casing wall reduction decreases the tangential resistance of casing strength. To evaluate the casing stress evolution under its worn shape, the thermal stress of casing is simulated as a time-dependent process. The proposed material properties in the model are designed in Tables 6.1 and 6.2. The dimension of this wellbore includes a casing diameter of 7 in. To be consistent with the reality of oil fields, cohesion force and friction angle of cement and rock are used in the simulations. The cohesion force is the force of attraction between the molecules of the same substance, and the friction angle measures the ability of rock or cement to resist the shear stresses.

Table 6.1 Wellbore geometry and properties for casing wear analysis

	ID, in.	OD, in.	Elastic modulus, psi	Poisson ratio	Cohesion force, psi	Friction angle, °
Casing	6	7	2.80E+07	0.3	Not applicable	Not applicable
Cement sheath	7	9	3.00E+06	0.24	8.00E+03	30
Rock	9	60	6.00E+06	0.2	6.00E+03	30

Table 6.2 Casing-cement-rock thermal properties for casing wear analysis

	Density, kg/m^3	Conductivity, btu/ft-hr-°F	Heat capacity, Btu/lb-°F	Thermal expansion, $°F^{-1}$
Casing	7.0E3	7.2	0.12	1.8E–05
Cement sheath	1.8E3	0.6	0.5	1.2E–05
Rock	2.0E3	0.48	0.4	1.4E–05

The reduction factor of worn casing is calculated using Eq. 6.25. The wear shape is assumed with a crescent shape, and the original casing thickness is 0.5 in. It has a 0.1-in. reduction after casing wear.

$$RF = \frac{h_{initial} - h_{reduction}}{h_{initial}} \tag{6.25}$$

Table 6.3 lists the profile of fluid temperature and pressure under different scenarios. To evaluate the stress concentration in worn casing, five base models are built with either different temperatures or pressures of fluid in the model. For simplicity, the maximum horizontal stress of rock is equivalent to the minimum horizontal stress.

Discussion of the following results will be confined to one well with different temperature and pressure profiles, and the well is circulated with fluids each hour in all cases. A series of simulations are performed to evaluate the stress concentration of the worn casing. The burst pressure and temperature of the fluids are chosen to provide the needed input data for a sensitivity analysis of the model. The plotted results in all cases are only shown in the casing and cement part.

Table 6.3 Profile of fluid temperature and burst pressure for casing wear analysis

	Fluid T, ˚F	Rock T, ˚F	Initial T, ˚F	Burst pressure, psi	Rock in-situ stress, psi
Case 1	350	350	350	12,500	11,000
Case 2	450	350	350	12,500	11,000
Case 3	450	350	350	13,500	11,000
Case 4	450	350	350	14,500	11,000
Case 5	450	350	350	13,500	0

Case 1: The identical temperature profile of fluid and rock implies that no heat transfer occurs in the cased well. The maximum radial stress is obtained around the interface of casing and cement. The predicted radial stresses indicate little difference in the worn part compared with those in the unworn part, as shown in Fig. 6.4.

The burst strength in worn casing has been reported by some researchers. The maximum hoop stress occurs at the inner diameter of the worn section (Wu and Zhang 2005). Without considering the confining effect of cement and rock, the casing burst stress in the worn part will be overestimated. This occurs because the burst pressure in

uncemented hole causes the tension effect when the casing stands along. Fig. 6.5 indicates that higher compression hoop stress occurs around the worn area. It likely causes the yield of worn casing or its compression failure.

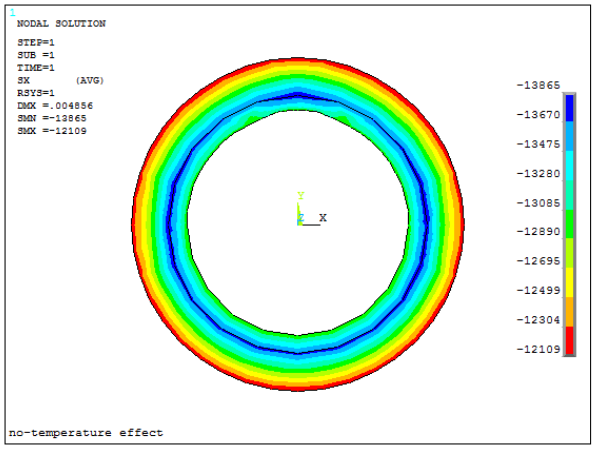

Fig. 6.4 Radial stress inside the worn casing-cement in Case 1.

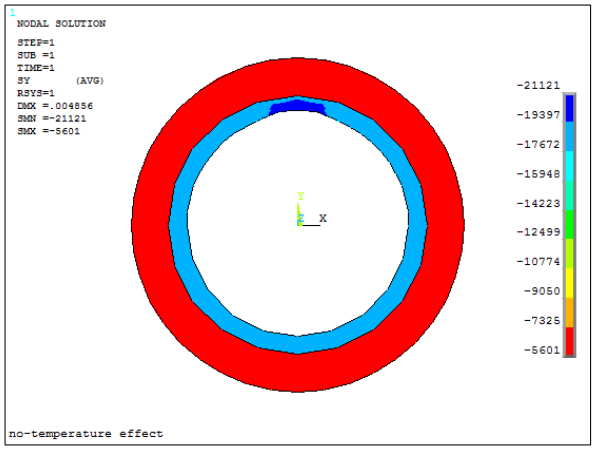

Fig. 6.5 Hoop stress inside the worn casing-cement in Case 1.

Case 2: The fluid temperature is set to 450˚F, which is much higher than the rock temperature of 350˚F. The thermal stress will take place until the heat transfer achieves its balance. The predicted results in this case are also recorded at 1 hour. Fig. 6.6

indicates that maximum compressive radial stress was increased by one-third by the temperature effect from 13866 psi to 19757 psi; although, it is unlikely to cause the yield by this amount.

The elevated casing temperature induced by hotter fluid and high operating pressure acting on the casing wall results in the expansion of the worn casing while constrained by the rock. The predicted results indicate that the constraint expansion causes a further compression effect to casing-cement. The maximum compressive hoop stress of 73791 psi, as shown in Fig. 6.7, is three times larger than it in Case 1; this value is beyond the strength limit of some casing types, such as J55 and K55. It is concluded that the worn casing in HPHT wells suffers from a high risk of compression failure in a tangential direction.

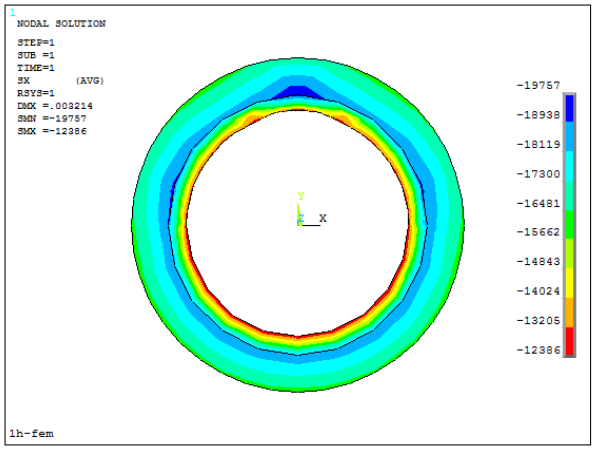

Fig. 6. 6 Radial stress inside the worn casing-cement in Case 2.

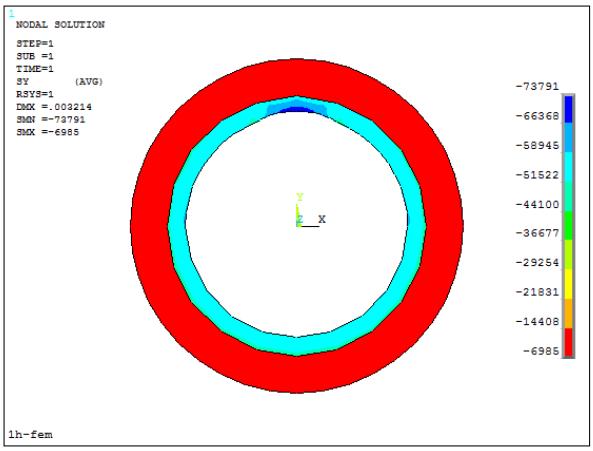

Fig. 6.7 Hoop stress inside the worn casing-cement in Case 2.

Case 3: This case is simulated in a same temperature profile used in Case 2, but it has an inner pipe operating pressure of 13,500 psi. The higher burst pressure, as expected, causes larger compression in the radial direction of casing to rock, as shown in Fig. 6.8.

The result obtained from Fig. 6.9 indicates that the larger burst pressure leads to a reduction of maximum hoop stress. This hoop stress is decreased from 73,791 to 68,671 psi. This is because the combination of the high temperature and constraint expansion effects causes an extremely large compression tangential load on the remaining part of the worn casing, whereas the increased burst pressure intends to expand the worn casing. Although the casing operating with a higher burst pressure can significantly reduce the maximum hoop stress in the worn part, it still risks failure under the large absolute value of the compression hoop stress.

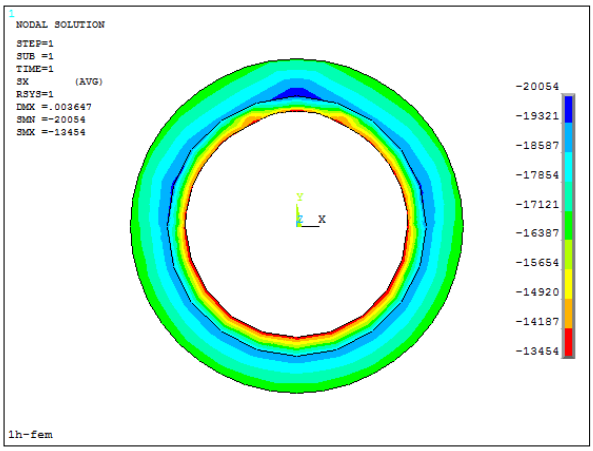

Fig. 6.8 Radial stress inside the worn casing-cement in Case 3

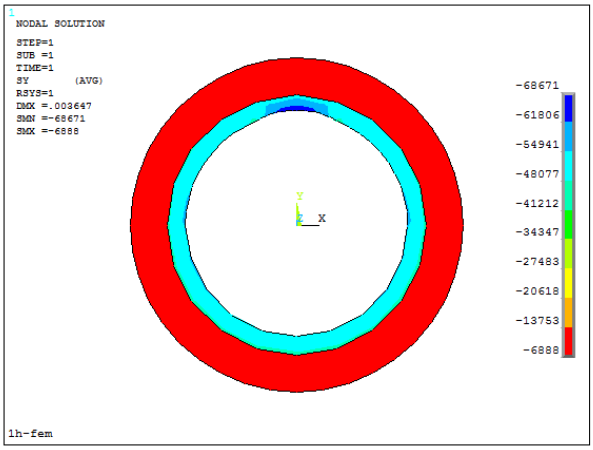

Fig. 6.9 Hoop stress inside the worn casing-cement in Case 3.

Case 4: The temperature profile in this case is identical those in Cases 2 and 3, but the burst pressure increases up to 14,500 psi. The predicted results from Fig. 6.10 clearly show the maximum radial stress slightly increasing along with the rising burst pressure. As expected, the maximum hoop occurs in the remaining portion of the worn part, and it decreases by 5,000 psi, as indicated in Fig. 6.11.

Cases 2 to 4 present stress profiles in the worn casing under different burst pressures. A higher stress concentration is predicted in all cases, but the risk of

compression casing cracking in the worn part declines because of the face of the burst pressure decreasing the compression hoop stress.

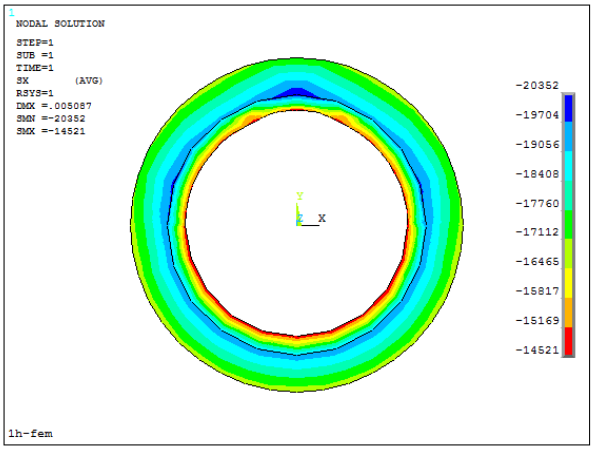

Fig. 6.10 Radial stress inside the worn casing-cement in Case 4.

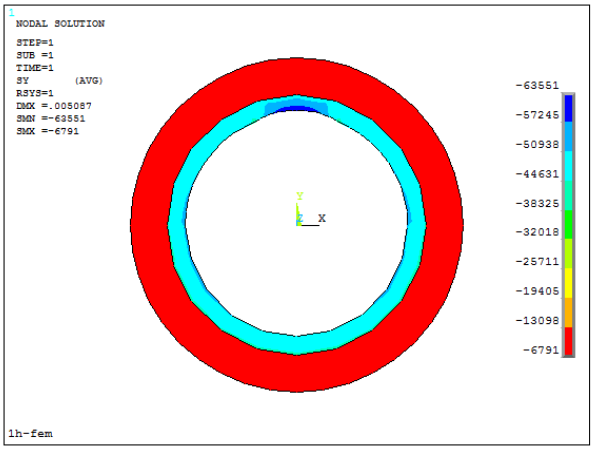

Fig. 6.11 Hoop stress inside the worn casing-cement in Case 4.

Case 5: The casing could suffer from experience large tension when the burst pressure is applied on the inner wall of casing without cementing formation. To evaluate stress behavior in the worn casing-cement by the effect of rock, the in-situ stress at the boundary of rock is assumed to be zero in this run. Fig. 6.12 depicts the radial stress profile of the worn casing, and the maximum value occurs on the inner wall of the casing, which is different from Cases 1 to 4.

Tension failure on the worn casing is observed when the burst pressure is higher than its confined pressure. Although the maximum hoop stress in this case, as shown in Fig. 6.13, is still predicted in the location of the worn area, it reveals that the worn part will suffer from extreme tension.

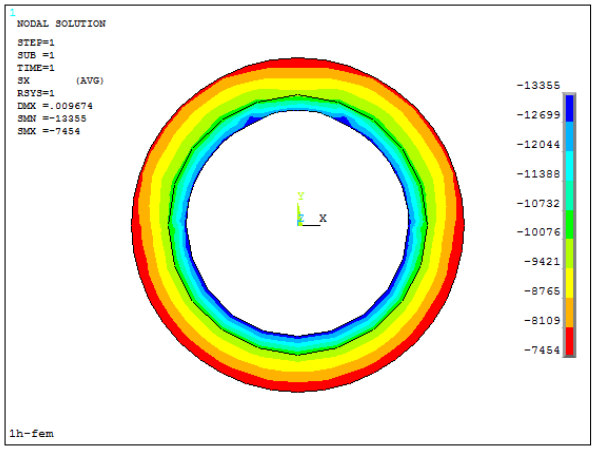

Fig. 6.12 Radial stress inside the worn casing-cement in Case 5

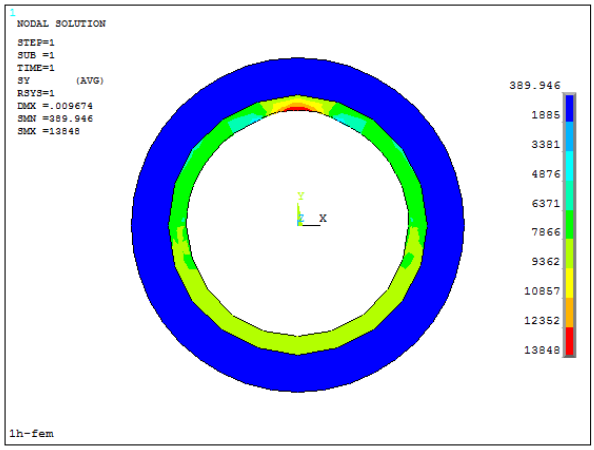

Fig. 6.13 Hoop stress inside the worn casing-cement in Case 5

6.5 Discussion

The induced stress of worn casing without considering the effect of rock is usually evaluated as unconstrained tension. The reality of casing in a well is that it is most likely

surrounded by the adjacent rocks. Not only does the burst pressure act on the casing wall, but the in-situ stress generated by rock also constrains the expansion of casing. Subsequently, hoop stress in the portion of worn casing could be under compression by the effect of the rocks, which is dependent on horizontal in-situ stresses.

An analytical solution evaluates the casing wear model in an HPHT well using boundary superposition. The worn casing suffers from the expected stress concentration around the worn part, and the radial stress shows the compression behavior in all cases. The burst pressure results in tension inside worn casing without considering the effect of formation, whereas the existence of the formation will confine the expansion of worn casing. The hoop stress of the worn areas depends upon the effect of the formation and it will increase sharply with the increase of burst pressure and elevation of temperature.

7. WELLBORE INSTABILITY INDUCED BY GAS MIGRATION DURING CEMENTING

7.1 Statement

Gas migration is a serious problem in the development of deep gas wells. It results in cement bond loss, ultimately damages the formation zonal isolation. In reality, the cased-hole instability caused by gas migration exists in all kinds of wells. The mechanical response in the casing-cement system is subject to change in a gas migration well. Understanding the stress evolution inside casing/cement in the gas migration well is important for identifying the status of well integrity.

As shown in Fig. 7.1, in the transition phase of fluid cement to solid cement, gas bubbles will flow up the annulus when the hydrostatic pressure of cement slurry is not able to balance the formation gas pressure. Permanent gas channels inside the cement sheath will generate after the gas bubbles traveling in the cement slurry. Stress redistribution in the well due to the existence of gas channels causes the instability on the casing-cement system.

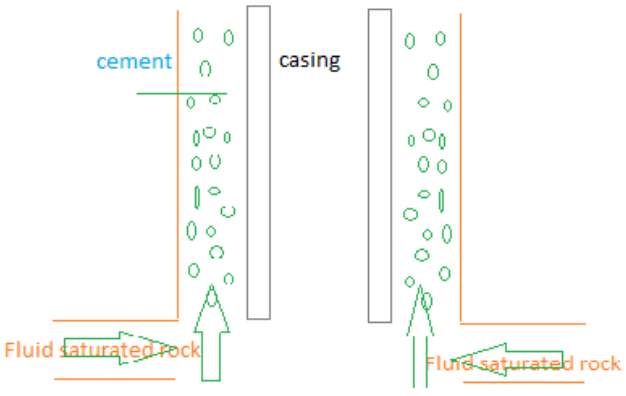

Fig. 7.1 Gas migration when cementing through fluid saturated formation

Some measurements reducing gas migration during the well completion stage have been developed based on the control of cement shrinkage. The researchers agree on that the drilling mud of high density is required to isolate the formation gas in Ghawar field [11]. In order to control gas migration in the cementing phase, other researchers study on dispersing and reducing gas bubbles using different cement slurries, meanwhile optimizing the cementing procedures. Ennings et, al. [11] developes new expanding additive mixed with the cement slurry to prevent the micro-annulus inside cement sheath. Steward (1988) prefers that the good displacement procedure would assist the cementing zonal isolation. A.L Martins et, al. [48] conducts the experimental study to control gas migration during the cementing stages. His report emphasizes that the integration operations including lab test, cement design and practical operation in field should be used to avoid gas migration.

In a well with gas channels caused by gas migration, the strength and mechanical behavior in the casing-cement system have been changed. Without understanding the new mechanical responses of casing/cement, the stability of the gas migration well cannot be properly evaluated. Casing-cement mechanical responses in the gas migration well have not been thoroughly understood.

We investigate stress distribution in and around the cement sheath with gas channels using finite element method. In our analysis, the casing-cement-formation system will not fail even the induced stress exceeds the material strength and the casing, cement and formation are fully bonded. We perform dedicate simulations for studying casing-cement stress evolution in differing gas channels inside the cement sheath. The gas channel model will be simulated in a quarter wellbore system. Gas channel will be assumed the cylindrical shape. The diameters of gas channels are 0.1 in., 0.2 in., 0.4 in. and 0.7 in. respectively. The thermal and hydraulic loads are imposed on the gas channel model. Tables 7.1 and 7.2 state the designed geometry and properties for this analysis.

Table 7.1 Thermal and mechanical properties for gas migration analysis

	Elastic modulus, psi	Poisson's Ratio	Density, g/cm^3	Thermal conductivity, btu/ft.hr. ˚F	Specific heat, Btu/lb. ˚F	Thermal expansion, ˚F ^-1
Casing	2.80E+07	0.3	7	7.2	0.12	1.8
Cement sheath	3.00E+06	0.24	1.8	0.6	0.5	1.2
Sandstone	6.00E+06	0.2	2	0.48	0.4	1.4

Table 7.2 The cased-hole geometry for gas migration analysis

Burst pressure, psi	10000
Formation horizontal stress, psi	12000
Initial wellbore temperature, ˚F	300
Formation T@ upper section, ˚F	350
Casing ID, In.	4.408
Casing OD, In.	5.5
cement sheath ID, In.	5.5
Cement sheath OD, In.	7
Formation ID, In.	7
Formation OD, In.	40
Fluid specific heat, btu/lb. ˚F	0.45
Fluid thermal conductivity, btu/ft.hr. ˚F	1.0
Fluid thermal convective, btu/ft^2.hr. ˚F	288
Mud circulating Time, hour	48

7.2 Cement sheath without gas channel

Under a HPHT well condition, we illustrate the casing-cement mechanical responses in the cased-hole model without gas channels. For the comparison analysis, the constant well geometry and properties are used in the cased-hole model with gas channels. In the first case, 0.1-in. diameter gas channel is located in the middle of cement sheath. The temperature of wellbore fluid acting on the casing inner surface is 300 ˚F, and temperature of 350 ˚F at the outer boundary of formation is used.

Cement sheath without gas channel: Figs. 7.2 to 7.7 have revealed that the radial stress, tangential stress and equivalent stress inside casing/cement without gas channel at 1 minute and 1 hour. The maximum compressive radial stress inside casing/cement was predicted at the interface of casing and cement. It decreased from 12377 psi at 1 minute to 11045 psi at 1 hour due to the cooling effect.

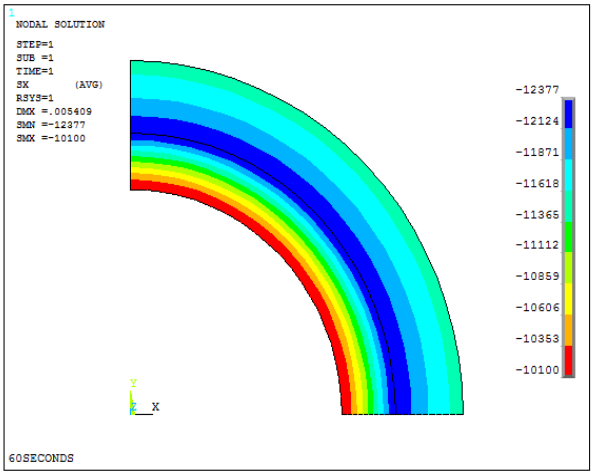

Fig. 7.2 Radial stress inside casing/cement without gas channel at 1 minute

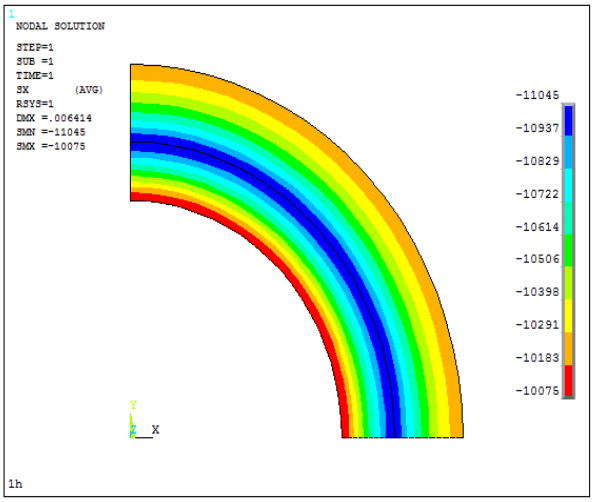

Fig. 7.3 Radial stress inside casing/cement without gas channel at 1 hour

The maximum compressive tangential stress at 1 minute was predicted as 25586 psi around the casing-cement interface, as indicated in Fig. 7.4. The cased-hole wellbore was cooled down along with the fluid movement in the wellbore. Fig. 7.5 has revealed that the thermal effect due to the fluid movement produced the maximum compressive tangential stress at the casing inner surface instead of that at the casing-cement interface.

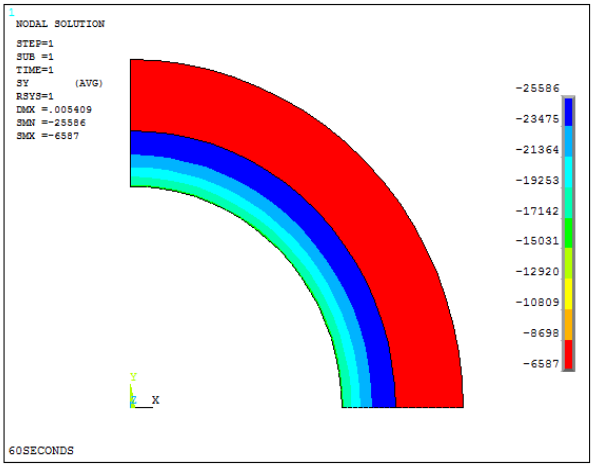

Fig. 7.4 Tangential stress inside casing/cement without gas channel at 1 minute

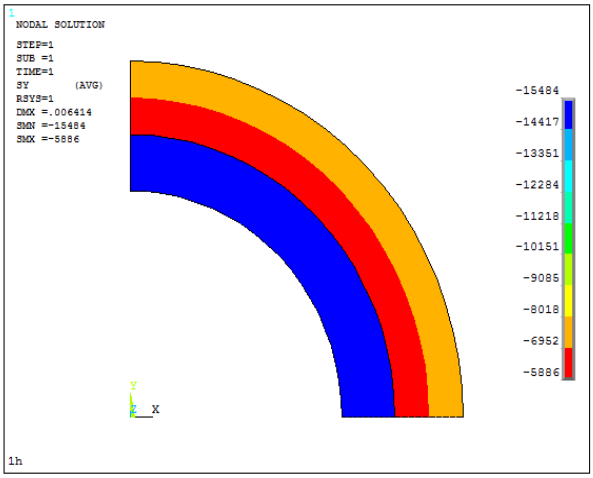

Fig. 7.5 Tangential stress inside casing/cement without gas channel at 1 hour

Figs. 7.6 and 7.7 have shown the equivalent stress inside casing/cement in the cased-hole model. The high stress at the inner wall of the casing is predicted. Compared to the radial and tangential stresses of casing/cement, the equivalent stress in the casing-cement system importantly increased, which rose from 24491 psi to 30209 psi by the end of 1 hour.

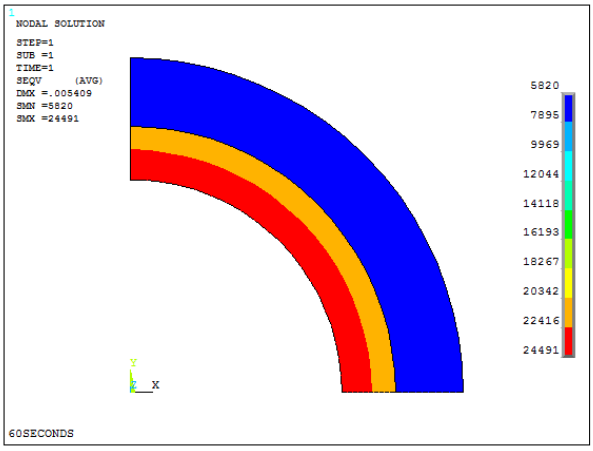

Fig. 7.6 Equivalent stress inside casing/cement without gas channel at 1 minute

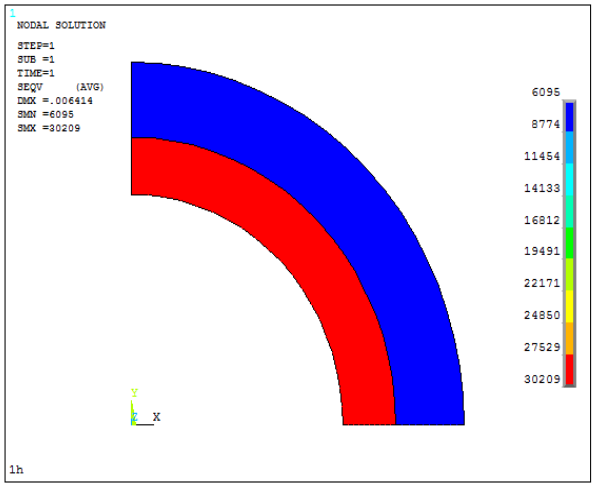

Fig. 7.7 Equivalent stress inside casing/cement without gas channel at 1 hour

7.3 Cement sheath with gas channel

Figs. 7.8 and 7.9 have shown that the maximum compressive radial stress occurred around the gas channel inside the cement sheath in the casing-cement system. The existence of gas channel due to the gas migration in the cased hole can alleviate the risk of radial cracking at the casing-cement interface. This maximum compressive radial stress decreased from 23303 psi at 1 minute to 20706 psi at 1 hour.

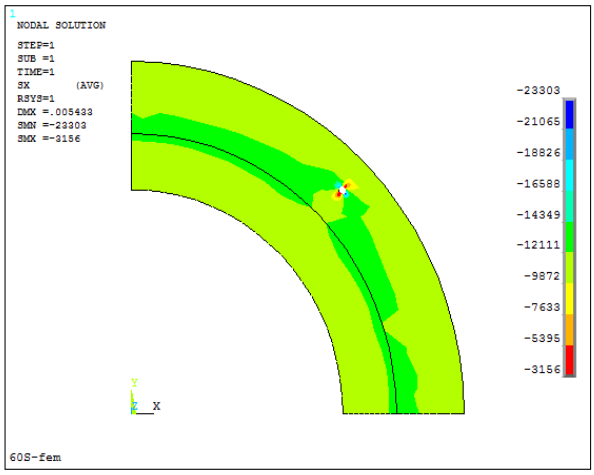

Fig. 7.8 Radial stress inside casing/cement with gas channel at 1 minute

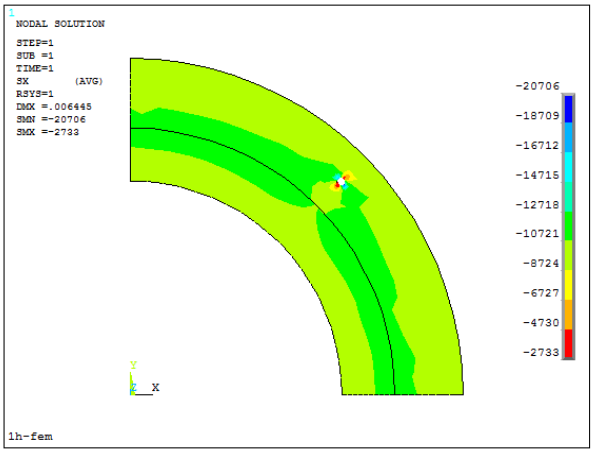

Fig. 7.9 Radial stress inside casing/cement with gas channel at 1 hour

Figs. 7.10 and 7.11 have shown that the maximum compressive tangential stress inside casing/cement occurred at the interface of casing and cement in the first minute. By the end of 1 hour, the maximum compressive tangential stress was predicted at inner surface of casing. Compared with the tangential stress inside the casing/cement without gas channel, the gas channel due to gas migration doesn't have apparent influence on the casing/cement in terms of the variation of tangential stress.

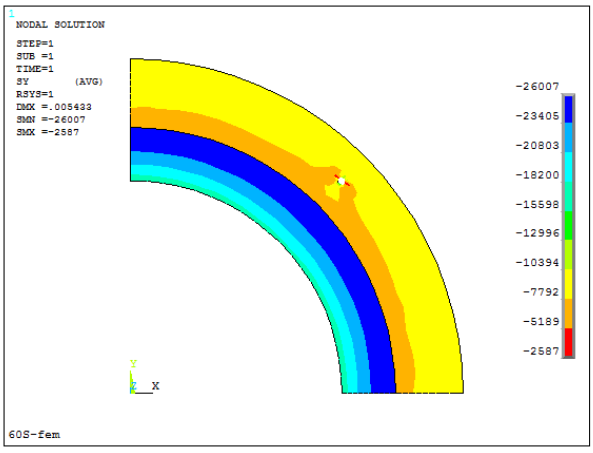

Fig. 7.10 Tangential stress inside casing/cement with gas channel at 1 minute

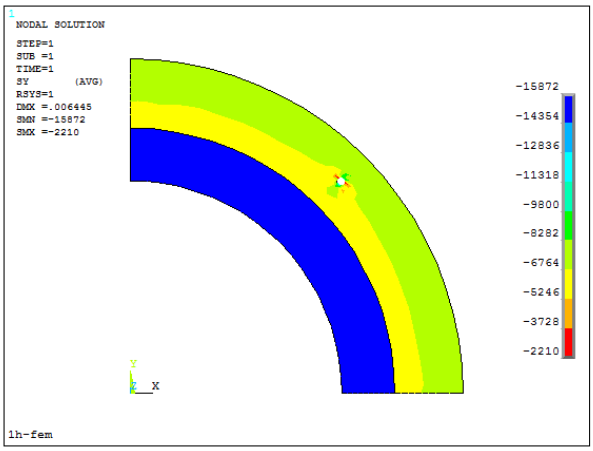

Fig. 7.11 Tangential stress inside casing/cement with gas channel at 1 hour

Figs. 7.12 and 7.13 have shown the equivalent stress of casing/cement at 1 minute and 1 hour. The maximum equivalent stress occurred at the inner surface of casing and increased to 30339 psi by the end of 1 hour. In terms of the variation of equivalent stress inside the casing/cement, gas channel caused by the gas migration had little influence on the casing/cement.

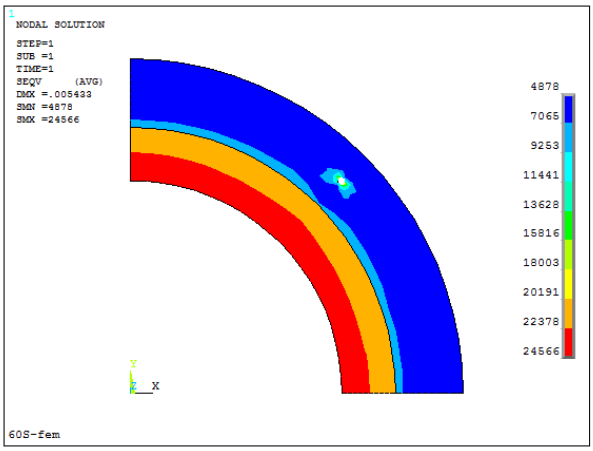

Fig. 7.12 Equivalent stress inside casing/cement with channel at 1 minute

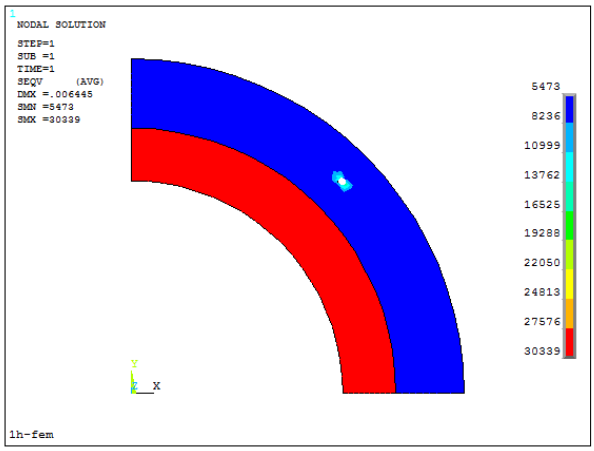

Fig. 7.13 Equivalent stress inside casing/cement with channel at 1 hour

Table 7.3 summarizes the radial stress, tangential stress and equivalent stress inside casing/cement in both gas migration and non gas migration cases. The stress with negative sign indicates a compression. Because of the channel after gas migration, the maximum compressive radial stress inside casing/cement in the gas migration case is as much as two times, compared with that in the non gas migration case.

Table 7.3 Maximum stress in the gas migration and non gas migration cases

	Gas migration			Without gas migration		
	Max Radial stress, psi	Max Tangential stress, psi	Max Equivalent stress, psi	Max Radial stress, psi	Max Tangential stress, psi	Max Equivalent stress, psi
1 minute	-23303	-26007	24566	-12377	-25586	24491
1 hour	-20706	-15872	30339	-11045	-15484	30209

7.4 The number of gas channel effect

In Fig. 7.1, formation gas migrating in the cement column is an uncontrollable process due to the complexity of down-hole conditions. Most likely there exist multiple gas channels inside the cement sheath after gas migration. We investigate the stress evolution inside casing/cement with up to four gas channels in the quarter cross-section model. Gas channel diameter of 0.2 in. is defined in this part. Casing, cement and formation are fully bonded.

On the plot of radial stress in Figs. 7.14 to 7.18, the maximum and minimum compressive radial stresses were predicted around the gas channels inside the cement sheath. The radial debonding inside casing/cement could start in the gas channel area instead of the interface of casing and cement. In fact, the maximum and minimum compressive radial stresses are perpendicular with respect to each other. Fig. 7.15 has revealed that the compressive radial stress in the casing-cement system increased from 11046 psi to 23187 psi by the presence of 0.2-in. diameter gas channel. However, the maximum radial stress inside the casing/cement didn't increase along with the increase of the number of the gas channels.

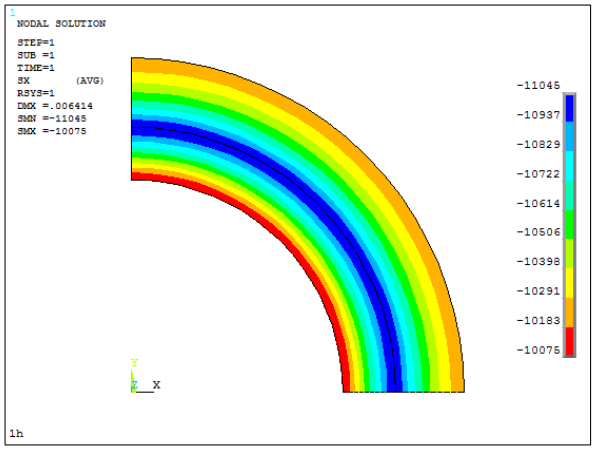

Fig. 7.14 Radial stress inside casing/cement without gas channel

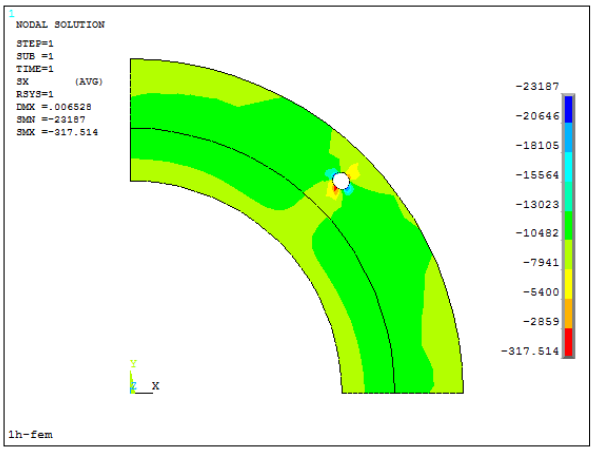

Fig. 7.15 Radial stress inside casing/cement with one 0.2-in gas channel

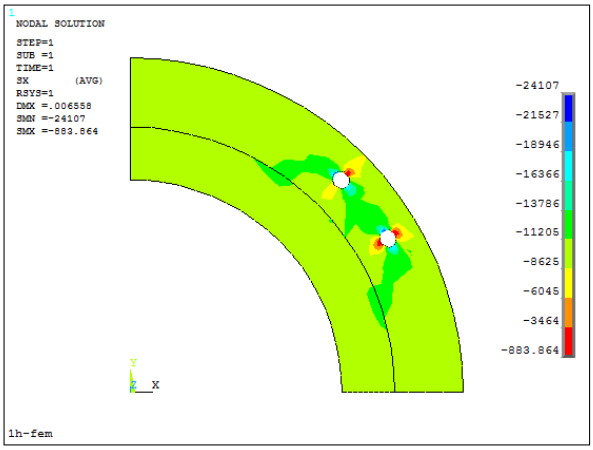

Fig. 7.16 Radial stress inside casing/cement with two 0.2-in gas channels

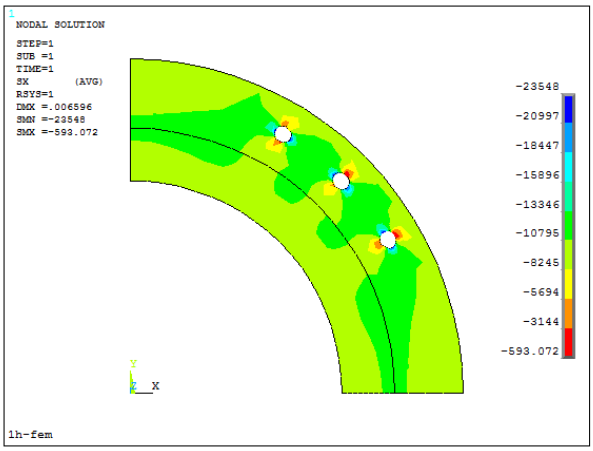

Fig. 7.17 Radial stress inside casing/cement with three 0.2-in gas channels

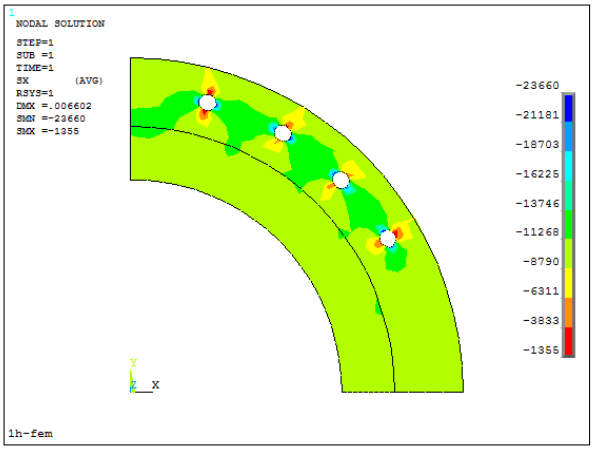

Fig. 7.18 Radial stress inside casing/cement with four 0.2-in gas channels

Figs. 7.19 to 7.23 have shown the compressive tangential stress inside the casing/cement with gas channel at 1 hour. The maximum compressive tangential stress was produced at the inner surface of casing in all cases. In the non gas migration case, the maximum compressive tangential stress of 15484 psi was predicted. The increase of the number of gas channels inside the cement sheath would not significantly increase the tangential stress in the casing-cement system.

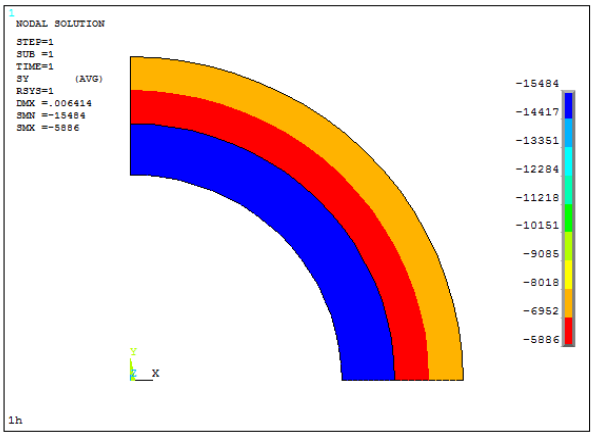

Fig. 7.19 Tangential stress inside casing/cement without gas channel

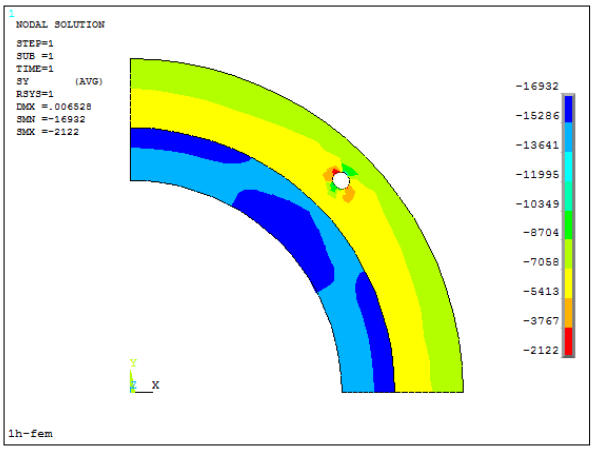

Fig. 7.20 Tangential stress inside casing/cement with one 0.2-in gas channel

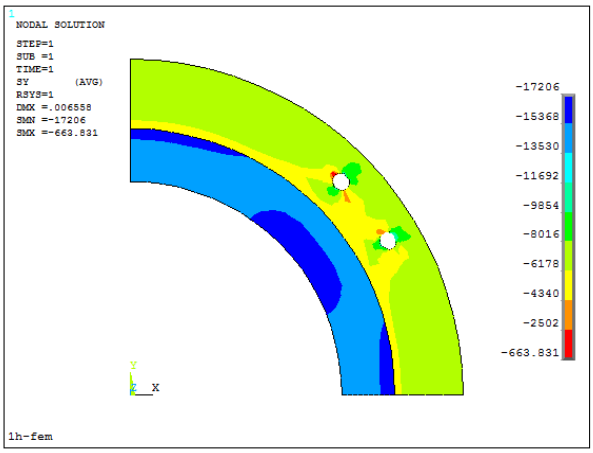

Fig. 7.21 Tangential stress inside casing/cement with two 0.2-in gas channels

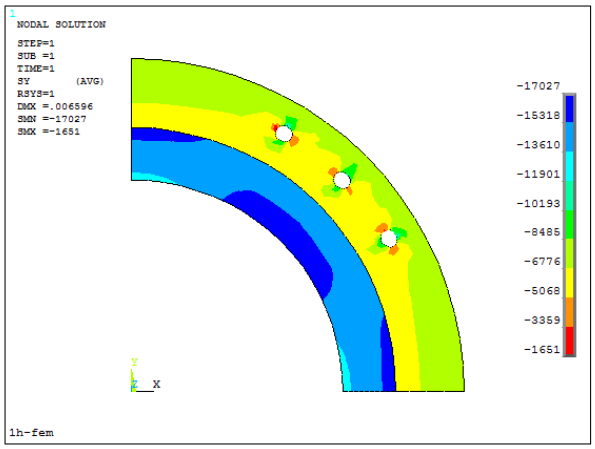

Fig. 7.22 Tangential stress inside casing/cement with three 0.2-in channels

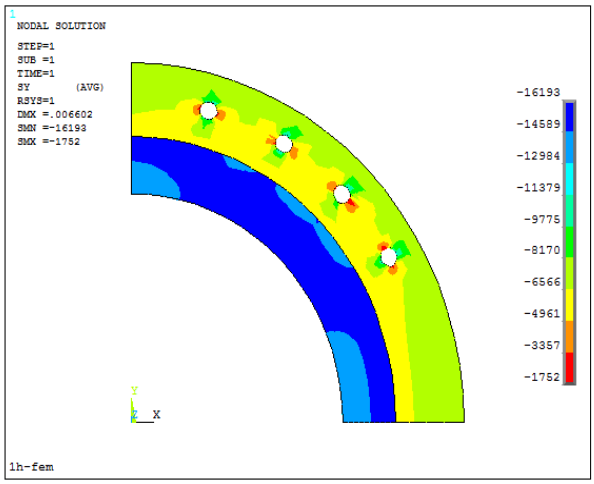

Fig. 7.23 Tangential stress inside casing/cement with four 0.2-in channels

Figs. 7.24 to 7.28 have revealed the equivalent stress inside the casing/cement with gas channel at 1 hour. The maximum equivalent stress was produced inside the casing. Fig. 7.24 has shown that the maximum equivalent stress of 30209 psi was predicted in the non gas migration case. It is noted that the maximum equivalent stress of 30464 psi inside casing/cement was generated by the presence of four gas channels of 0.2-in. diameter. In terms of the variation of equivalent stress, the increase of number of gas channels would not significantly influence the casing-cement instability.

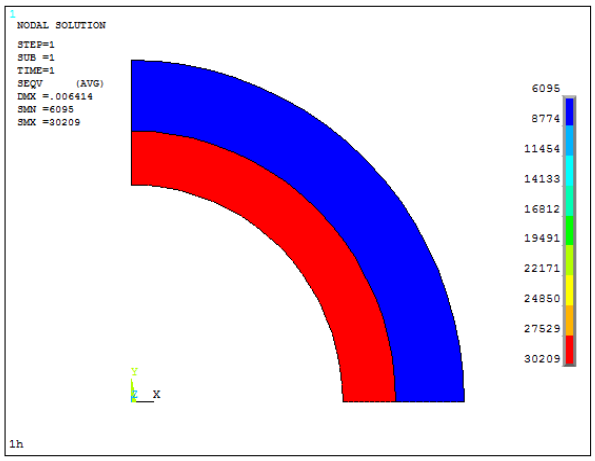

Fig. 7.24 Equivalent stress inside casing/cement without gas channel

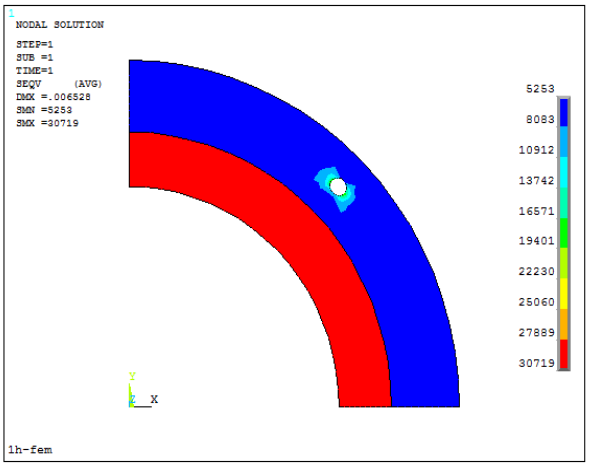

Fig. 7.25 Equivalent stress inside casing/cement with one 0.2-in gas channel

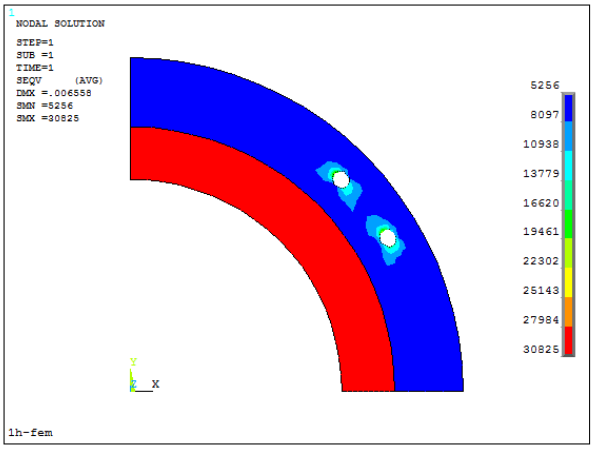

Fig. 7.26 Equivalent stress inside casing/cement with two 0.2-in gas channels

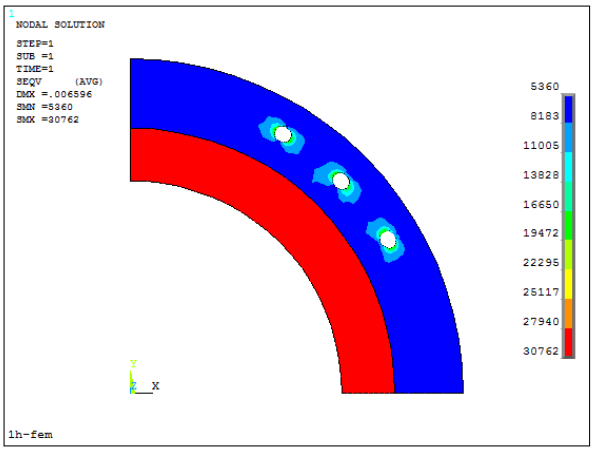

Fig. 7.27 Equivalent stress inside casing/cement with three 0.2-in gas channels

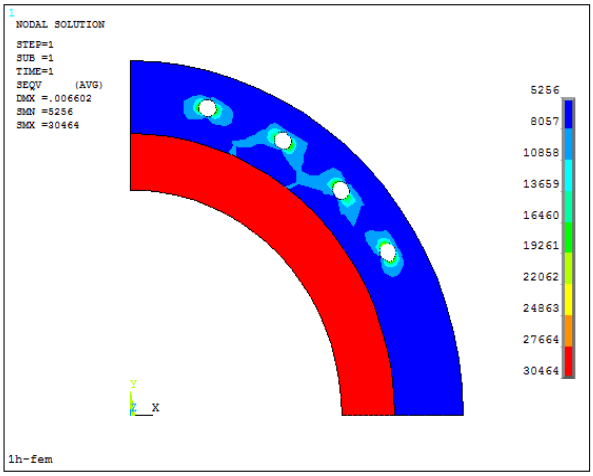

Fig. 7.28 Equivalent stress inside casing/cement with four 0.2-in gas channels

7.5 Gas channel Size effect

The size of gas channel is identified as an important parameter to determine the state of stress inside casing/cement. This part investigates the mechanical response of casing/cement in differing gas channels. 0.1 in. 0.2 in. 0.4 in. and 0.7 in. gas channels inside the cement sheath are assumed in the model.

Figs. 7.29 to 7.30 have revealed that the maximum radial stress of 23187 psi, in the gas channel of 0.2-in case, is slightly higher than the maximum radial stress of 20706

psi, in the gas channel of 0.1-in. case. The instability at the interface of casing and cement is less likely to occur due to the uniform stress distribution in the casing-cement system.

The maximum compressive radial stress of 20706 psi was produced in 0.1 in. gas channel case compared with the 21443 psi in 0.7 in. gas channel case. Figs 7.29 and 7.32 revealed that the positive value of radial stress marked by the red regions indicated the occurrence of tension inside casing/cement. The casing-cement system will be under the risk of tensile cracking due to the limited tensile resistance of cement.

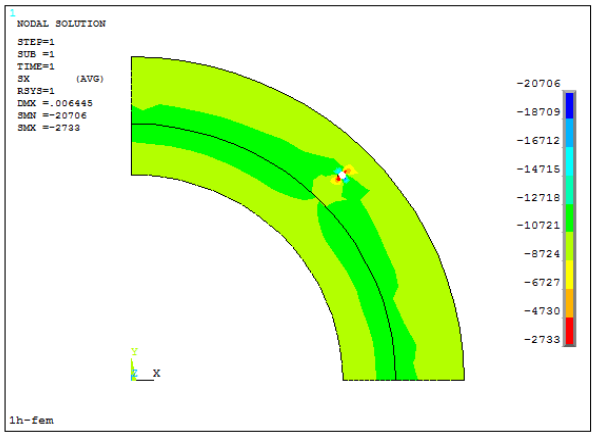

Fig. 7.29 Radial stress inside casing/cement with 0.1- in. gas channel

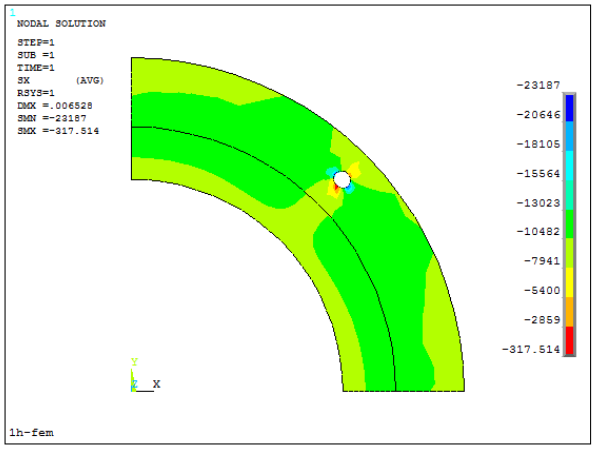

Fig. 7.30 Radial stress inside casing/cement with 0.2-in. gas channel

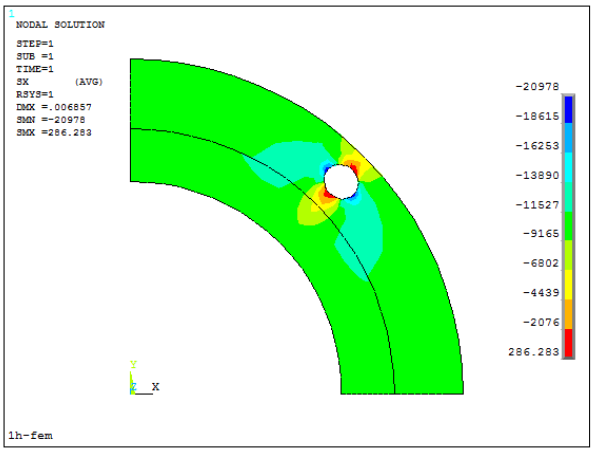

Fig. 7.31 Radial stress inside casing/cement with 0.4-in. gas channel

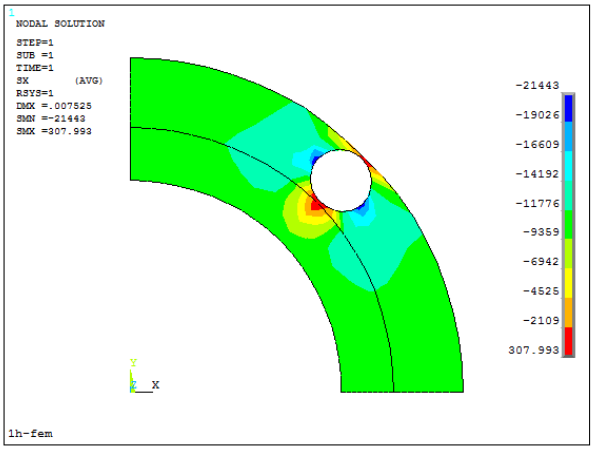

Fig. 7.32 Radial stress inside casing/cement with 0.7-in. gas channel

Figs. 7.33 to 7.36 have revealed the compressive tangential stresses in differing gas channel. The maximal tangential stress of 15872 psi inside the casing/cement was produced in the presence of 0.1 in. gas channel. In 0.7-in gas channel case, the maximum compressive tangential stress was significantly elevated to 29359 psi. Overall, the predicted results have demonstrated that the maximum compressive tangential stress increased along with the increase of gas channel size.

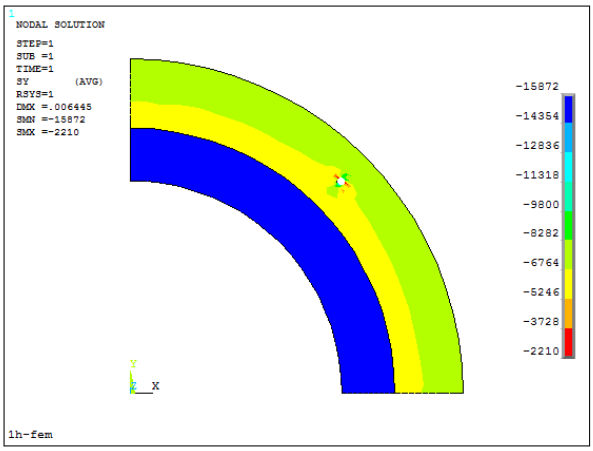

Fig. 7.33 Tangential stress of casing/cement with 0.1-in.gas channel

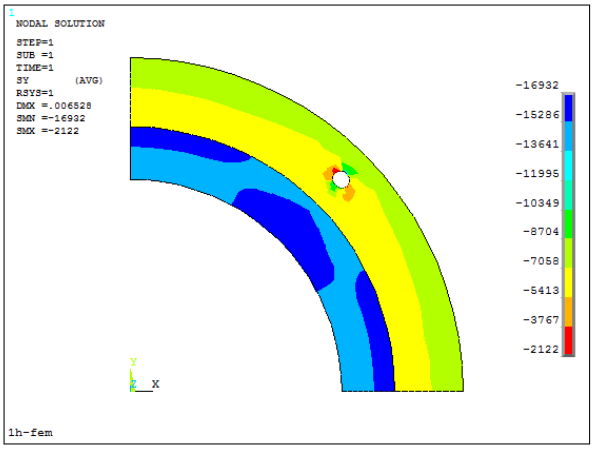

Fig. 7.34 Tangential stress of casing/cement with 0.2-in. gas channel

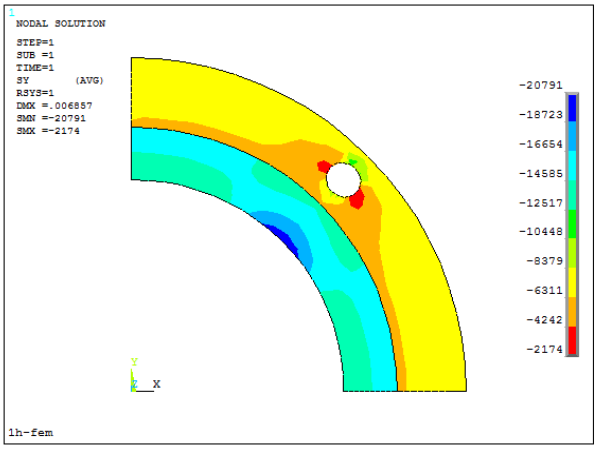

Fig. 7.35 Tangential stress of casing/cement with 0.4-in. gas channel

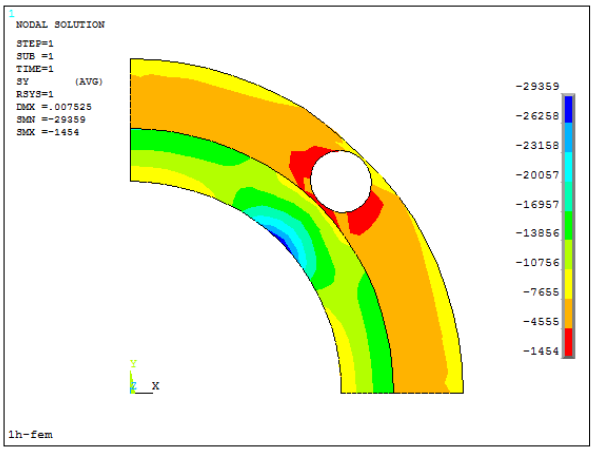

Fig. 7.36 Tangential stress of casing/cement with 0.7-in. gas channel

The increase of gas channel size apparently increase the maximum equivalent stress inside casing/cement. Figs. 7.37 to 7.40 have revealed that the equivalent stress in differing gas channels. Similarly like that in the case without gas channel, casing will suffer from the high induced equivalent stress. However, the equivalent stress inside casing/cement didn't significantly increase, despite the size of gas channel increased up to 0.7 in.

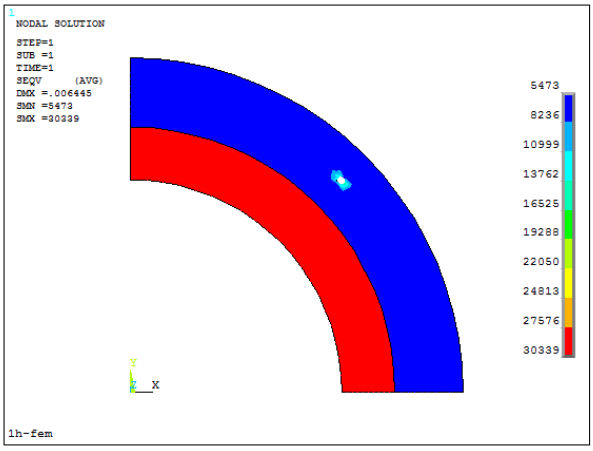

Fig. 7.37 Equivalent stress of casing/cement with 0.1-in. gas channel

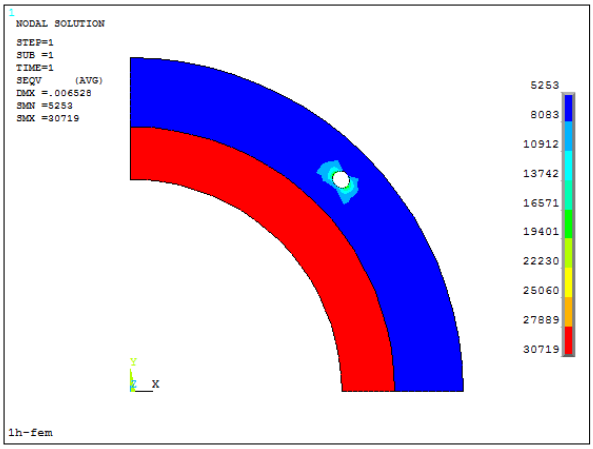

Fig. 7.38 Equivalent stress of casing/cement with 0.2-in. gas channel

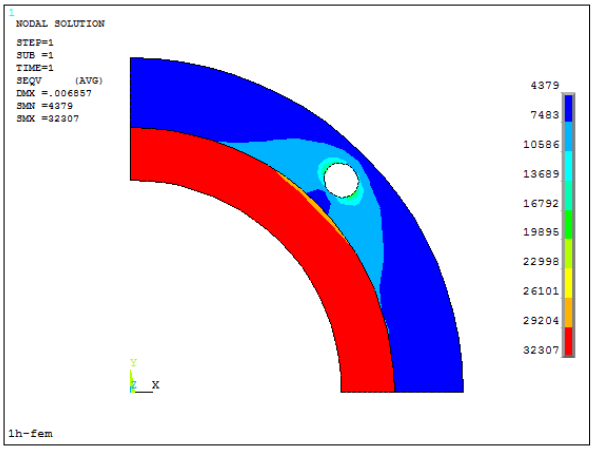

Fig. 7.39 Equivalent stress of casing/cement with 0.4-in. gas channel

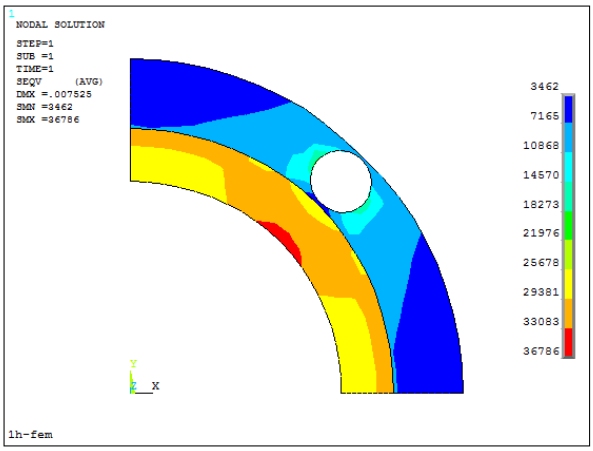

Fig. 7.40 Equivalent stress of casing/cement with 0.7-in. gas channel

Table 7.4 lists the maximum induced stresses inside casing/cement in the cased-hole model. It is concluded that, during the wellbore fluid movement in the wellbore, the tangential stress and equivalent stress inside casing/cement will be significantly increased along with the increase of gas channel size.

Table 7.4 Sensitivity analysis of gas channel size

Channel Diameter, in.	0.1	0.2	0.4	0.7
Max Radial stress, psi	-20706	-23187	-20978	-21443
Max Tangential stress, psi	-15872	-16932	-20791	-29359
Max Equivalent stress, psi	30339	30719	32307	36786

Along with the increase of gas channel size, the tensile radial stress will generate in the casing-cement system. Figs. 7.43 and 7.44 have revealed the maximum and minimum radial stresses as a function of gas channel size. Both maximum radial stress and minimum radial stress occurred around the gas channel, but they are in different directions. This model predicted the maximum compressive radial stress at the tangential direction. The radial stress increased to approximate 26,000 psi in the presence of 0.2-in. gas channel, and then decreased slightly once the gas channel size is greater than the critical size.

Fig 7.43 has revealed that, when the gas channel size was smaller than 0.23 in.; the compressive minimum stress decreased along with the increase of gas channel size. However, the tension inside the casing/cement was produced when the gas channel size was greater than 0.23 in. This tension will be a major factor to cause the cement cracking because of the limited tensile tolerance of cement.

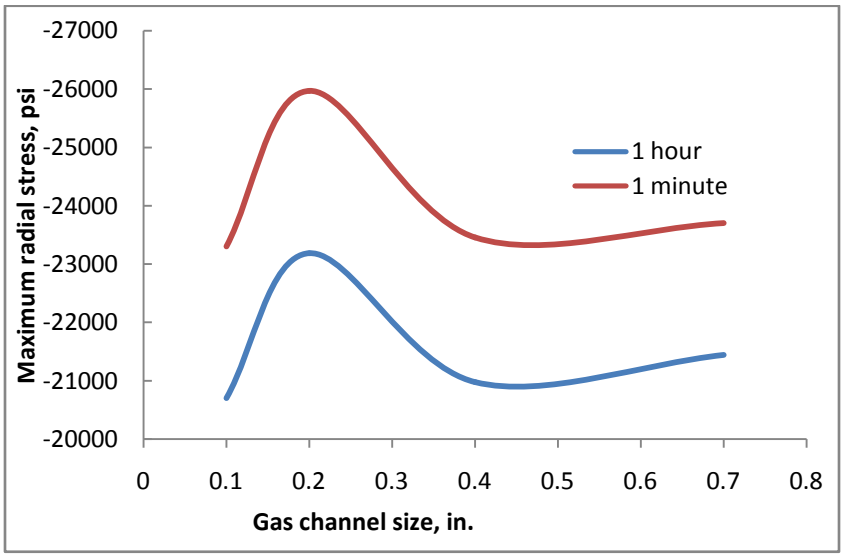

Fig. 7.41 Maximum radial stress in differing size of gas channel

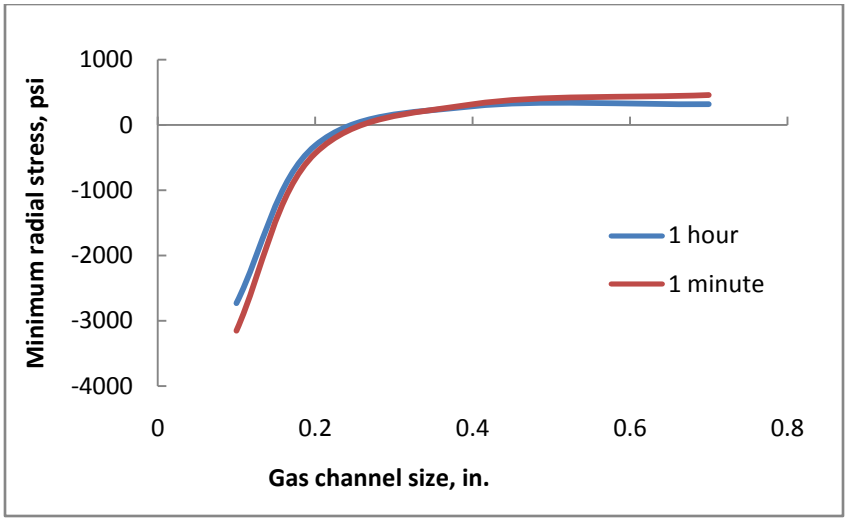

Fig. 7.42 Minimum radial stress in differing size of gas channel

7.6 Discussion

This section discussed mechanical responses of casing/cement with gas channels caused by gas migration. The stress concentration occurs at the areas around the gas channel. Gas migration can induce a higher risk of cracks in the casing-cement system. It is concluded that the gas migration effect can be negligible by the presence of the small gas channel.

In the presence of gas channel inside a cement sheath after gas migration, the compressive maximum stress and minimum stress in the proposed numerical models are found around the gas channel. They are perpendicular to each other. The radial stress is increased inside the cement with the increase of the number of gas channels. However, the increase of gas channels has little influence on casing-cement tangential and equivalent stresses.

It is indicated that the size of a gas channel is an important factor to determine casing-cement instability. There exists a critical gas channel size inside cement. In the above analysis, the maximum compressive radial increased with the increase of gas channel size when the gas channel is less than 0.2 in.

More importantly, the minimum compressive radial stress inside cement sheath decreased with the increase of gas channel size. When the diameter of gas channel is

greater than a certain value, the predicted minimum compressive radial stress will produce tension. Cement sheath is easily subject to cracking because of the little tensile tolerance. The consequence of the cracking may cause important instability in the casing-cement system. The compressive tangential stress of cement apparently increases by the presence of gas channel. The equivalent stress at the inner surface of casing presents a maximum value, but it has been little impacted because of the existence of gas channel.

8. CONCLUSIONS AND RECOMMENDATIONS

8.1 Conclusions

A precise understanding of the induced wellbore stresses plays a crucial role in dealing with the cased-hole instability. This research has investigated the cased-hole instability using numerical analytical techniques. Through analyzing the variation of induced stress in the casing-cement system, the factors such as transient thermal load, casing wear, nonhomogeneous formation resulting in cemented well instabilities in HPHT wells are investigated. Without properly evaluating the above factors, casing and cement instabilities in the cased hole will be predicted unrealistically. Our work provides a basis for the evaluation of cased well instability in the planning stages of drilling and well completion.

The transient thermal and mechanical behaviors in the cased hole have been presented. Heat transfer through formation in the cased hole is much slower than it is inside casing/cement. The interface of casing and cement should not be always considered a higher debonding region. This study showed that, when the wellbore fluid temperature was higher than the formation temperature, the maximum compressive radial stress occurred at the interface of casing and cement sheath. In our specific case, the radial stress at the casing-cement interface will increase under the critical time and decrease thereafter.

Compared with the heating effect, the cooling effect tends to reduce the compressive radial stress in the casing-cement-formation system. Both heating and cooling effects indicated that the higher tangential and equivalent stresses happened at the inner boundary of casing. The equivalent stress inside casing/cement has not yet affected as much as the radial and tangential stress in this model.

Casing-cement mechanical response is obviously affected by the tectonic effect of formation. The maximum radial stress occurs at the upper interface of casing and cement, which is in the direction of formation minimum radial stress. The equivalent

stress inside casing/cement is most sensitive to the tectonic effect. A strong formation tectonic effect will induce the larger equivalent stress.

The nonhomogeneous formation is concluded to have a significant impact on the radial stress redistribution inside casing/cement. The risk of radial cracking and shear failure in the casing-cement-sandstone layer is higher than that in the casing-cement-shale layer. Within a lower Young's modulus for shale, the higher radial stress was predicted in the casing-cement-sandstone layer. The body force of the cased-hole model has not yet apparent effect on the stress distribution inside casing/cement.

Worn casing suffers from the expected stress concentration around the worn part, and the compressive radial stress occurred in our cases. Tangential stress in the portion of worn casing could also produce compression by the effect of the rock. This is dependent on horizontal in-situ stresses. The tangential stress will increase significantly with the increase of burst pressure and temperature elevation. Tension failure in the worn-casing system could occur when the burst pressure is much higher than the formation pressure.

The gas channel size and the number of gas channel inside cement sheath are identified as two important factors to influence the casing-cement stability. By the presence of gas channel caused by gas migration, stress concentration occurs around the gas channel. The more gas channels there are, the higher radial stress is induced inside the cement sheath. The compressive maximum radial stress and minimum radial stress in the proposed numerical model were found to be perpendicular to each other. More importantly, the minimum compressive radial stress will decrease with the increase of gas channel size. When the diameter of gas channel is greater than a certain value, the minimum compressive radial stress in the cased-hole system will produce tension inside the cement sheath.

8.2 Future work

This report concentrated on the analysis of casing-cement instability in cased hole through building the down-hole stress profile. For the next stage of this research, our

methods presented in this work can be extended to apply to directional wells or multilateral wells stability analysis. In addition, the pre-induced torque and drag of casing strings during drilling phase, especially located in well conjunctions as well as kick off and drop off sections, should be addressed in the analysis of well integrity.

This work mainly focuses on the radial cross-section of cased wellbore. The small size of this model with dedicated meshes did guarantee the results accuracy. Future research may increase the dimension of the 3D model in order to simulate a longer cased-hole section. The mechanical response of casing/cement/formation in an arbitrary direction should be emphasized. Casing/cement could survive after the elastic failure. The future work may include the plastic failure study in casing-cement system. In addition, the future model is suggested to be capable of dealing with the fully nonlinear material properties of cased hole.

This research assumed that there was no fracture inside the formation. The future model also needs to account into the influence of natural fractures and stimulated fractures in casing-cement-formation system under non-isothermal down-hole conditions.

REFERENCES

1. Heathman, J.F. and Beck, F.E., *Finite Element Analysis Couples Casing and Cement Designs for HTHP Wells in East Texas*, in *IADC/SPE Drilling Conference*. 2006, Society of Petroleum Engineers: Miami, Florida, USA.

2. Zhang, J., *The impact of shale properties on wellbore stability*. 2005, PhD dissertation, The University of Texas at Austin. p. 260 .

3. Manriquez, A.L., *Finite element modeling of the stability of single wellbores and multilateral junctions*. 2003, PhD dissertation, The University of Texas at Austin. p. 239.

4. Wu, J. and Zhang, M., *Casing Burst Strength After Casing Wear*, in *SPE Production Operations Symposium*. 2005: Oklahoma City, Oklahoma.

5. Yadav, A., *Casing Impairment/Damage in Stress- Sensitive Reservoir-A Case Study*, in *Canadian International Petroleum Conference*. 2003, Petroleum Society of Canada: Calgary, Alberta.

6. Heathman, J., Tare, U. and Ravi, K., *Understanding Formation (In)Stability During Cementing*, in *SPE/IADC Drilling Conference*. 2003: Amsterdam, Netherlands.

7. Ravi, K., Vargo, R.F., and Cox, B., *Successful Cementing Case Study in Tuscaloosa HPHT Well*, in *SPE Russian Oil and Gas Technical Conference and Exhibition*. 2008: Moscow, Russia.

8. Vargo, R.F. , *Improved Deepwater Cementing Practices Help Reduce Nonproductive Time*, in *IADC/SPE Drilling Conference*. 2006: Miami, Florida, USA.

9. Bour, D.L. and Wilkinson, J.G. , *Combating Gas Migration in the Michigan Basin.* SPE Drilling Engineering, 1992. **7**(1).

10. Coker, O.D., Harris, K.L. and Williams, T.A., *Preventing Shallow Gas Migration in Offshore Wells: The Performance of Lead Cements*, in *European Petroleum Conference*. 1992: Cannes, France.

11. Jennings, S.S., Al-Ansari, A.A. and Al-Yami, A.S., *Gas Migration After Cementing Greatly Reduced*, in *Middle East Oil Show*. 2003: Bahrain.

12. Fleckenstein, W.W., Eustes, A.W. and Miller, M.G., *Burst-Induced Stresses in Cemented Wellbores.* SPE Drilling & Completion, 2001. **16**(2): p. 74-82.

13. Gray, K.E., Podnos, E. and Becker, E., *Finite Element Studies of Near-Wellbore Region During Cementing Operations: Part I*, in *Production and Operations Symposium*. 2007, SPE: Oklahoma City, Oklahoma, U.S.A.

14. Nabipour, A., Joodi, B. and Sarmadivaleh, M., *Finite Element Simulation of Downhole Stresses in Deep Gas Wells Cements*, in *SPE Deep Gas Conference and Exhibition*. 2010, SPE: Manama, Bahrain.

15. Rodriguez, W.J., Fleckenstein, W.W. and Eustes, A.W., *Simulation of Collapse Loads on Cemented Casing Using Finite Element Analysis*, in *SPE Annual Technical Conference and Exhibition*. 2003, SPE: Denver, Colorado.

16. Shahri, M., Schubert, J.J. and Amani, M., *Detecting and Modeling Cement Failure in High-Pressure/High-Temperature (HP/HT) Wells, Using Finite Element Method (FEM)*, in *International Petroleum Technology Conference*. 2005, IPTC: Doha, Qatar.

17. Thiercelin, M.J., *Cement Design Based on Cement Mechanical Response.* SPE Drilling & Completion, 1998. **13**(4): p. 266-273.

18. Wu, J. and Knauss, M.E., *Casing Temperature and Stress Analysis in Steam-Injection Wells*, in *International Oil & Gas Conference and Exhibition in China*. 2006, SPE: Beijing, China.

19. Sunal, O., *A Look Into Casing Deformation Due to Plastic Behavior of Formations*, in *SPE Eastern Regional/AAPG Eastern Section Joint Meeting*. 2008, SPE: Pittsburgh, Pennsylvania, USA.

20. Bradley, W.B. and Fontenot, J.E., *The Prediction and Control of Casing Wear (includes associated papers 6398 and 6399).* SPE Journal of Petroleum Technology, 1975(02).

21. Gao D.L., Sun, L. Z., Lian J.H., *Prediction of casing wear in extended-reach drilling.* Journal of Petroleum science 2010. **7**: p. 494-501.

22. Hall, R.W. and Malloy, K.P., *Contact Pressure Threshold: An Important New Aspect of Casing Wear*, in *SPE Production Operations Symposium*. 2005, Society of Petroleum Engineers: Oklahoma City, Oklahoma.

23. Calhoun, W.M., *Casing Wear Prediction and Management in Deepwater Wells*, in *SPE Deepwater Drilling and Completions Conference*. 2010, Society of Petroleum Engineers: Galveston, Texas, USA.

24. Song, J.S., Bowen, J. and Klementich, F. , *The Internal Pressure Capacity of Crescent-Shaped Wear Casing*, in *SPE/IADC Drilling Conference*. 1992, 1992 Copyright 1992, IADC/SPE Drilling Conference.: New Orleans, Louisiana.

25. Rainforth, W.M., *Microstructural evolution at the worn surface: a comparison of metals and ceramics.* Journal of Wear, 2000. **245**(1–2): p. 162-177.

26. Thiercelin, M.J., *Cement Design Based on Cement Mechanical Response*, in *SPE Annual Technical Conference and Exhibition*. 1997, 1997: San Antonio, Texas.

27. Fakhreldin, Y.E., *Novel Technique to Determine Cement Contamination*, in *SPE/IADC Middle East Drilling Technology Conference and Exhibition*. 2011: Muscat, Oman.

28. Crrok, R. and James, H., *Predicting potential gas-flow rates to help determine the best cementing practices*, in *IADC*. 1998.

29. Hibbeler, J.C., DiLullo, G. and Thay, M., *Cost-Effective Gas Control: A Case Study of Surfactant Cement*, in *SPE Asia Pacific Oil and Gas Conference*. 1993: Singapore.

30. Li, X., Cui, L. and Roegiers ,J.C., *Thermoporoelastic Analyses of Inclined Boreholes*, in *SPE/ISRM Rock Mechanics in Petroleum Engineering*. 1998, Society of Petroleum Engineers: Trondheim, Norway.

31. Santoyo, E., *Convective heat-transfer coefficients of non-Newtonian geothermaldrilling fluids.* Journal of Geochemical Exploration, 2003. **78-79**(0): p. 249-255.

32. Kurashige, M., *A thermoelastic theory of fluid-filled porous materials.*. Journal of Solids Structures, 1988. **25**: p. 14.

33. Ferronato, M., Castelletto, N. and Gambolati, G. , *A fully coupled 3-D mixed finite element model of Biot consolidation.* Journal of Computational Physics, 2010. **229**(12): p. 4813-4830.

34. McTigue, D.F., *Thermoelastic response of fluid-saturated porous rock.* Journal of Geophysical Research, 1986. **91**: p. 9533-9542.

35. Marshall, D.W. and Bentsen, R.G. , *A Computer Model to Determine the Temperature Distributions In a Wellbore.* Journal of Canadian Petroleum Technology, 1982. **21**(1).

36. Corre, B., Eymard, R. and Guenot, A., *Numerical Computation of Temperature Distribution in a Wellbore While Drilling*, in *SPE Annual Technical Conference and Exhibition*. 1984: Houston, Texas.

37. Oudeman, P. and Kerem, M., *Transient Behavior of Annular Pressure Build-up in HP/HT Wells*, in *Abu Dhabi International Conference and Exhibition*. 2004, Society of Petroleum Engineers: Abu Dhabi, United Arab Emirates.

38. Timosenko, S.P. and Goodier,J.N., *Theory of Elasticity*. 1970, New York: McGraw Hill Press.

39. Reddy, J.N., *An introduciton to Nonlinear finite element analysis*. 2004, New York: Oxford University Press.

40. Farahani, H.S., *Modeling Transient Thermo-Poroelastic Effects on 3D Wellbore Stability*, in *SPE Annual Technical Conference and Exhibition*. 2006: San Antonio, Texas, USA.

41. Fleckenstein, W.W., Eustes, A.W. and Miller, M.G. , *Burst Induced Stresses in Cemented Wellbores*, in *SPE/AAPG Western Regional Meeting*. 2000, Copyright 2000, Society of Petroleum Engineers Inc.: Long Beach, California.

42. Clifton, R.J., Brown, U. and Wang, J.J., *Modeling of In-Situ Stress Change Due to Cold Fluid Injection*, in *International Arctic Technology Conference*. 1991, 1991: Anchorage, Alaska.

43. Nguyen, V.X. and Abousleiman, Y.N., *The Porochemothermoelastic Coupled Solutions of Stress and Pressure With Applications to Wellbore Stability in Chemically Active Shale*, in *SPE Annual Technical Conference and Exhibition*. 2009, Society of Petroleum Engineers: New Orleans, Louisiana.

44. Nair, R. and Abousleiman, Y. , *A Porothermoelastic Wellbore Model in Oil and Gas Saturated Naturally Fractured Porous Media*, in *SPE Saudi Arabia Section Technical Symposium*. 2009, Society of Petroleum Engineers: AlKhobar, Saudi Arabia.

45. Tran, T. D., Roegiers, J.C. and Thiercelin, M. , *Thermally-Induced Tensile Fractures In the Barnett Shale And Their Implications to Gas Shale Fracability*, in *44th U.S. Rock Mechanics Symposium and 5th U.S.-Canada Rock Mechanics Symposium*. 2010, American Rock Mechanics Association: Salt Lake City, Utah.

46. Tao, Q. and Ghassemi, A., *Poro-thermoelastic borehole stress analysis for determination of the in situ stress and rock strength.* Geothermics, 2010. **39**(3): p. 250-259.

47. Fjaer, E. and Holt, R.M., *petroleum related rock mechanics*. 2004, Oxford,UK: Elsevier. 483.

48. Martins, A.L., *Tools for Predicting and Avoiding Gas Migration After Casing Cementing in Brazilian Fields*, in *Latin American and Caribbean Petroleum Engineering Conference*. 1997: Rio de Janeiro, Brazil.

APPENDIX A

Coordinate transformation

Stresses in Cartesian and Cylindrical coordinates can be transformed each other Fajaer et al (1992). The temperature and stress profiles in previous models are solved in Cartesian coordinate. The transformation between the cylindrical coordinate and Cartesian coordinate can be made, as shown in the following equations. The radial stress is along a radial direction. Since the direction perpendicular to radial stress is on the tangent line of wellbore. Hoop stress in this report is same with tangential stress.

$$\sigma_r = \sigma_x \cos^2\theta + \sigma_y \sin^2\theta + 2\sigma_{xy}\sin\theta\cos\theta \tag{A-1}$$

$$\sigma_\theta = \sigma_x \sin^2\theta + \sigma_y \cos^2\theta - 2\sigma_{xy}\sin\theta\cos\theta \tag{A-2}$$

$$\sigma_z = \sigma_z \tag{A-3}$$

$$\sigma_{r\theta} = (\sigma_y - \sigma_x)\sin\theta\cos\theta + \sigma_{xy}(\cos^2\theta\sin^2\theta) \tag{A-4}$$

$$\sigma_{rz} = \sigma_{xz}\cos\theta + \sigma_{yz}\sin\theta \tag{A-5}$$

$$\sigma_{\theta z} = \sigma_{yz}\cos\theta - \sigma_{xz}\sin\theta \tag{A-6}$$

Similarly, strains in Cartesian coordinate are expressed in terms of Cylindrical coordinate, as shown in the following equation.

$$\varepsilon_r = \frac{1}{2}(\varepsilon_x + \varepsilon_y) + \frac{1}{2}(\varepsilon_x - \varepsilon_y)\cos 2\theta + \gamma_{xy}\sin 2\theta \tag{A-7}$$

$$\sigma_\theta = \sigma_x \sin^2\theta + \sigma_y \cos^2\theta - 2\sigma_{xy}\sin\theta\cos\theta \tag{A-8}$$

$$\sigma_z = \sigma_z \tag{A-9}$$

$$\gamma_{r\theta} = \frac{1}{2}(\varepsilon_y - \varepsilon_x)\sin 2\theta + \gamma_{xy}\cos 2\theta \tag{A-10}$$

$$\gamma_{rz} = \gamma_{xz}\cos\theta + \gamma_{zy}\sin\theta \tag{A-11}$$

$$\gamma_{\theta z} = \gamma_{yz}\cos\theta - \gamma_{xz}\sin\theta \tag{A-12}$$

APPENDIX B

The important part of finite element modeling is to apply appropriate weight function to evaluate each element. As stated in B1 to B15, the matrix coefficients over a master element in Chapter 2 are described by the following integral forms.

$$K_{ij}^{11} = \int_{\Omega e} (\lambda + 2G) \frac{\partial \phi_i}{\partial x} \frac{\partial \phi_j}{\partial x} d\Omega \tag{B-1}$$

$$K_{ij}^{12} = \int_{\Omega e} (\lambda + G) \frac{\partial \phi_i}{\partial x} \frac{\partial \phi_j}{\partial y} d\Omega \tag{B-2}$$

$$K_{ij}^{13} = \int_{\Omega e} (\lambda + G) \frac{\partial \phi_i}{\partial x} \frac{\partial \phi_j}{\partial z} d\Omega \tag{B-3}$$

$$K_{ij}^{21} = \int_{\Omega e} (\lambda + G) \frac{\partial \phi_i}{\partial y} \frac{\partial \phi_j}{\partial x} d\Omega \tag{B-4}$$

$$K_{ij}^{22} = \int_{\Omega e} (\lambda + 2G) \frac{\partial \phi_i}{\partial y} \frac{\partial \phi_j}{\partial y} d\Omega \tag{B-5}$$

$$K_{ij}^{23} = \int_{\Omega e} (\lambda + G) \frac{\partial \phi_i}{\partial y} \frac{\partial \phi_j}{\partial z} d\Omega \tag{B-6}$$

$$K_{ij}^{31} = \int_{\Omega e} (\lambda + G) \frac{\partial \phi_i}{\partial z} \frac{\partial \phi_j}{\partial x} d\Omega \tag{B-7}$$

$$K_{ij}^{32} = \int_{\Omega e} (\lambda + G) \frac{\partial \phi_i}{\partial z} \frac{\partial \phi_j}{\partial y} d\Omega \tag{B-8}$$

$$K_{ij}^{33} = \int_{\Omega e} (\lambda + 2G) \frac{\partial \phi_i}{\partial z} \frac{\partial \phi_j}{\partial z} d\Omega \tag{B-9}$$

$$K^{T1} = \int_{\Omega e} \frac{\alpha E}{1 - 2\nu} T \frac{\partial \phi_i}{\partial x} d\Omega \tag{B-10}$$

$$K^{T2} = \int_{\Omega e} \frac{\alpha E}{1-2\nu} T \frac{\partial \phi_i}{\partial y} d\Omega \tag{B-11}$$

$$K^{T3} = \int_{\Omega e} \frac{\alpha E}{1-2\nu} T \frac{\partial \phi_i}{\partial z} d\Omega \tag{B-12}$$

$$F^1 = \int_{\Omega e} \phi_i f_x d\Omega - \oint_{\Gamma} \frac{\alpha E}{1-2\nu} T \phi_i ds \tag{B-13}$$

$$F^2 = \int_{\Omega e} \phi_i f_y d\Omega - \oint_{\Gamma} \frac{\alpha E}{1-2\nu} T \phi_i ds \tag{B-14}$$

$$F^3 = \int_{\Omega e} \phi_i f_z d\Omega - \oint_{\Gamma} \frac{\alpha E}{1-2\nu} T \phi_i ds \tag{B-15}$$